博士論文

論文題目　Study of Plasma Current Start-Up by the Lower Hybrid Wave Using X-ray Measurements on the TST-2 Spherical Tokamak

（TST-2球状トカマクにおけるX線計測を用いた低域混成波による
プラズマ電流立ち上げの研究）

氏　名　山﨑　響

Doctoral Thesis

Study of Plasma Current Start-Up by the Lower Hybrid Wave Using X-ray Measurements on the TST-2 Spherical Tokamak

（TST-2 球状トカマクにおける X 線計測を用いた低域混成波によるプラズマ電流立ち上げの研究）

A thesis submitted for the degree of Doctor of Philosophy
by

Hibiki Yamazaki

Department of Complexity Science and Engineering
Graduate School of Frontier Sciences
The University of Tokyo

December 11, 2019

Abstract

Spherical tokamak (ST) can be a compact and economical reactor, but plasma current start-up method without the central solenoid needs to be established. The final target of this study is to understand the plasma current start-up and current drive process in ST configurations, and experiments and measurements have been carried out for this target.

In the TST-2 spherical tokamak device, current drive experiments using the lower hybrid wave (LHW) are carried out. Although the LHW shows very high current drive efficiency in conventional tokamaks, it is believed to be difficult to use it in spherical tokamaks, because it cannot propagate at low magnetic field. Therefore, it is important to understand the current drive physics, such as wave propagation, absorption by electrons, and fast electron transport in ST configurations. In addition, optimization and control of wave launching scenario is essential. Since the LHW accelerates electrons directly through Landau damping, and the generated fast electrons carry the plasma current, it is necessary to get information on the fast electrons produced by the LHW. Measurements of x-rays (XRs) emitted through bremsstrahlung process is a standard method to study the behavior of the fast electrons and the physics of lower hybrid current drive (LHCD).

In this study, we developed several wide energy range (a few keV to several hundreds keV) x-ray measurement systems, and investigated the spectrum under various conditions. As a result of soft x-ray measurement using two filters, Fe: 10 μm and Al: 200 μm, the signal ratio during LHW injection showed $\sim$ 20 %, suggesting the presence of the characteristic line radiation from stainless steel components. In the modulation experiment, a fluctuation synchronized with the power modulation of LHW was measured, and in the phase where LHW is off, it was found that the signal ratio was 60 % or more and it indicates the measured spectrum is considered to be a continuous spectrum.

As a result of HXR measurements, a spectrum of the photon energies below 100 keV was measured by vertical sightlines using thin PEEK flange, and the dependence on the plasma current was observed. Using a newly developed LYSO scintillation detector, a good sensitivity for high energy x-rays and an excellent time resolution have been demonstrated. A strong dependence of the radiated HXR energy on the plasma position was found and described by model considering RF induced radial transport. Thick target spectra by fast electrons colliding with the antenna limiter was modeled, and experimental HXR spectra were quantitatively explained by the model. Consequently, the loss mechanism of fast electrons was explained for the first time.

For a more sophisticated x-ray measurements, a state of the art detector "CMOS based 2-dimensional pixel array sensor with electrical discriminators and counters" is an attractive detector. Since there is few implemented cases in plasma experiments, we have developed a computational tool for designing multi-energy soft x-ray (ME-SXR) measurement system using the detector, and applied this tool to estimate SXR emission for the MST device at the University of Wisconsin-Madison and the DIII-D device at General Atomics as well as the JT-60SA device at QST and the NSTX-U device at PPPL. This computational tool can calculate the spectral, spatial and temporal responses of the ME-SXR pinhole cameras for arbitrary plasma densities ($n_{\mathrm{e,D}}$), temperature (T_{e}) and impurity densities (n_{Z}). For the purpose of simulating the detector response, a large database has been created for calculating the SXR emission from several ions (e.g. D, C, O, Al, Si, Ar, Ca, Fe, Ni, Mo and W) generally encountered in tokamaks.

The ME-SXR pinhole camera system for MST has been designed using this tool and calculated results

were compared with experimental data at MST and it was found that the measured signals are comparable to the calculation results within a factor of two. This is the first verification of the tool by an actual plasma. Using this tool, ME-SXR system designs have been developed for several devices including TST-2 and QUEST at Kyushu University and the installations are planned. This tool can be used not only for the design of a system suitable for each target plasma, but also for the analysis of experimental data.

Contents

List of Figures

List of Tables

List of abbreviations

CCC	Capacitively-coupled comb-line
CS	Central solenoid
DCO	Deuterium, Carbon, and Oxygen
ECH	Electron cyclotron heating
ECW	Electron cyclotron wave
EEDF	Electron energy distribution function
HFS	High field side
HXR	Hard x-ray
JC	Judgment coefficient
LCFS	Last closed flux surface
LFS	Low field side
LG	Light guide
LHCD	Lower hybrid current drive
LHW	Lower hybrid wave
ME-SXR	Multi-energy soft x-ray
OH	Ohmic heating
PEEK	Polyether ether ketone
PF	Poloidal field
PHA	Pulse height analysis
PMT	Photo multiplier tube
PPCD	Pulsed poloidal current drive
QSH	Quasi-single helicity
RF	Radio frequency
SBD	Surface barrier diode
SNR	Signal to noise ratio
ST	Spherical tokamak
SXR	Soft x-ray
TF	Toroidal field
XCS	X-ray crystal spectroscopy
XIS	X-ray imaging systems

Chapter 1

Introduction

1.1 Nuclear fusion and plasmas

Nuclear fusion is one of the nuclear reactions where two or more nuclei or subatomic particles collide to produce a heavier nucleus. When the mass of the produced nucleus becomes closer to that of iron, the reaction tends to generate an energy because iron is the most stable nucleus. Nuclear fission is another type of reaction where a heavy nuclei, such as uranium splits into small lighter nuclei, and the reaction tends to release an energy. The released energy is equal to the defect of mass, and it is written as $E = \Delta mc^2$, where E is the released energy, c is the speed of light and Δm is the difference in the total masses before and after the reaction.

A deuterium (D)–tritium (T) reaction, written as

$$\mathrm{D} + \mathrm{T} \longrightarrow {}^4\mathrm{He}\,(3.52\ \mathrm{MeV}) + {}^1\mathrm{n}\,(14.06\ \mathrm{MeV}), \tag{1.1}$$

is one of the easiest fusion reactions to cause, and the world's fusion research is focused on this reaction because of the following several advantages : virtually inexhaustible fuel which we can get from seawater, capability of producing large amount of energy, and large reaction cross section at a lower temperature compared with those for other reactions. Fusion reactions which are considered for a fusion power source including the D–T reaction is listed in Table. 1.1. Reaction No. 1 is the D–T reaction, and No. 2, No. 3 and No. 6 are the reactions known as proton–proton chain reactions which generate the energy of the sun.

The cross section of the D–T reaction is the largest and the reaction can occur at a lower energy compared with other reactions.

In order to cause a fusion reaction, sufficient energy is needed to overcome the mutual Coulomb repulsion force between ions, and make the particles closer to the range of strong force. This energy can be achieved

Table 1.1: Favorable fusion reactions [1, 2].

1.	${}^2\mathrm{D} + {}^3\mathrm{T}$	$\rightarrow$	${}^4\mathrm{He}\,(3.52\ \mathrm{MeV}) + {}^1\mathrm{n}\,(14.06\ \mathrm{MeV})$
2.	${}^1\mathrm{p} + {}^1\mathrm{p}$	$\rightarrow$	${}^2\mathrm{D} + \mathrm{e}^- + 0.42\ \mathrm{MeV}$
3.	${}^2\mathrm{D} + {}^1\mathrm{p}$	$\rightarrow$	${}^3\mathrm{He} + 5.49\ \mathrm{MeV}$
4.	${}^2\mathrm{D} + {}^2\mathrm{D}$	$\rightarrow$	${}^3\mathrm{T}\,(1.01\ \mathrm{MeV}) + {}^1\mathrm{p}\,(3.02\ \mathrm{MeV})$ (50 %)
		$\rightarrow$	${}^3\mathrm{He}\,(0.82\ \mathrm{MeV}) + {}^1\mathrm{n}\,(2.45\ \mathrm{MeV})$ (50 %)
5.	${}^2\mathrm{D} + {}^3\mathrm{He}$	$\rightarrow$	${}^4\mathrm{He}\,(3.67\ \mathrm{MeV}) + {}^1\mathrm{p}\,(14.68\ \mathrm{MeV})$
6.	${}^3\mathrm{He} + {}^3\mathrm{He}$	$\rightarrow$	${}^1\mathrm{p} + {}^1\mathrm{p} + {}^4\mathrm{He} + (12.86\ \mathrm{MeV})$
7.	${}^1\mathrm{p} + {}^{11}\mathrm{B}$	$\rightarrow$	$3\ {}^4\mathrm{He} + 8.7\ \mathrm{MeV}$

by heating the ions to very high temperatures, which normally lead to a plasma state. In addition, in order to obtain a net energy, it is necessary to sustain the particles with sufficient density during a sufficiently long time. That is why the temperature (T), density (n) and energy confinement time ($\tau_{\rm E}$) are the most important parameters for nuclear fusion power plants.

The condition of these parameters T, n and $\tau_{\rm E}$ necessary to maintain the fusion reaction was evaluated by John.D.Lawson in 1957 [3]. Here, the number of reaction per unit volume and unit time is expressed as $n_{\rm d} n_{\rm t} \langle v\sigma \rangle$, and the output power of D–T reaction is $P_{\rm th} = (n^2/4) \langle v\sigma \rangle E$, where $\langle v\sigma \rangle$ is a reaction cross section, and $n_{\rm d} = n_{\rm t}$ is assumed. An energy confinement time $\tau_{\rm E}$ is defined by the ratio of the stored energy of plasma $(3/2)n(T_{\rm e} + T_{\rm i}) = 3nT$ and the energy loss per unit time $P_{\rm L}$, that is $\tau_{\rm E} = 3nT/P_{\rm L}$.

Assuming that the energy loss of the fusion reactor is expressed as the sum of $P_{\rm L}$ and bremsstrahlung $P_{\rm B} = \alpha n^2$, then the condition that the fusion output energy becomes the same as the input energy is expressed as

$$\begin{aligned} P_{\rm L} + P_{\rm B} = \eta(P_{th} + P_{\rm L} + P_{\rm B}) \Leftrightarrow \eta \left(\frac{n^2}{4} < v\sigma > E + \frac{3nT}{\tau_{\rm E}} + \alpha n^2 \right) > \frac{3nT}{\tau_{\rm E}} + \alpha n^2 \\ \Leftrightarrow n\tau_{\rm E} > \frac{3T}{\dfrac{\eta}{4(1-\eta)} \langle v\sigma \rangle E + \alpha}. \end{aligned} \tag{1.2}$$

Assuming that η is $1/3$ as a general power generation efficiency, or $1/5$ as a case where the fusion reaction is sustained by the energy of ^{4}He particle, the $n\tau_{\rm E}$–T diagram obtained from Eq. (1.1) is called a Lawson criterion [3]. The case of $\eta = 1/3$ is called a "break–even condition" which the fusion output energy becomes the same as the input energy, and the case of $\eta = 1/5$ is called an "ignition condition" which the fusion reaction can be sustained without external heating. The minimum of the product for ignition condition is $n\tau_{\rm E} \geq 1.5 \times 10^{20}$ s/m^3 occurs at $T \sim 26$ keV. Note that the triple product of n, $\tau_{\rm E}$ and T has also been used as a more convenient indicator of the parameters needed for sustaining a fusion reaction. The minimum triple product of the break-even condition for D–T reaction is $nT\tau_{\rm E} \geq 1.0 \times 10^{21}$ keV $\cdot$ s/m^3.

As shown by these conditions, we have to confine a high density plasma for a long time to obtain sufficient energy from the fusion reaction. Several effective schemes of plasma confinement have been investigated, and tokamak, which confines a plasma with strong magnetic fields, is considered to be the most practical scheme for a fusion reactor.

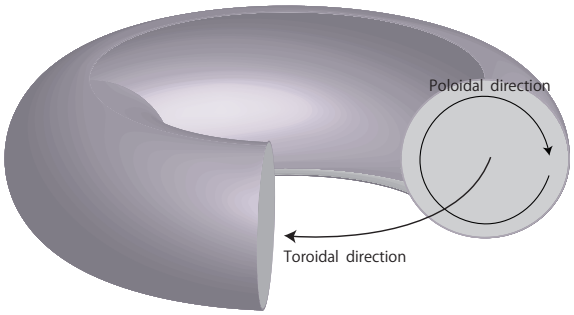

Figure 1.1: Definition of toroidal and poloidal directions.

1.2 Tokamak

The word tokamak is a Russian acronym for "ТОроидальная КАмера с МАгнитными Катушками" meaning TOroidal CHAmber with MAgnetic Coils [4]. Tokamak uses magnetic fields to trap charged particles, and keep them away from the vacuum vessel wall. It has two magnetic field components shown in Fig. 1.1, toroidal and poloidal components, to avoid particle loss caused by drift motions. The toroidal component ($B_{\rm t}$) is produced by the toroidal field (TF) coils, and the poloidal component ($B_{\rm pol}$) is produced mainly by the plasma current ($I_{\rm p}$) in the toroidal direction.

Tokamak is currently the most successful confinement scheme, and the break–even condition was achieved by the JT–60U tokamak in 1998 [5,6]. For the development of tokamak reactors, ITER project is in progress, and the device is now under construction in France. The objective of ITER project is the research and development under a situation close to that in fusion power plants, and to achieve $Q = 10$, where Q is the ratio of the fusion power to the input power.

In tokamaks, the beta value is defined as the ratio of the plasma pressure to the magnetic pressure as,

$$\beta = \frac{P}{B^2/2\mu_0}, \tag{1.3}$$

and is an indicator of the efficiency of magnetic confinement method. A high beta value indicates an economical confinement that the plasma thermal pressure can be confined with a smaller magnetic pressure. Here, the fusion power density $P_{\rm F}$ is approximately proportional to $\beta_{\rm t}^2 B_{\rm t}^4 V_{\rm p}$, where $\beta_{\rm t}$ is the toroidal beta value, $B_{\rm t}$ is the toroidal magnetic field, and $V_{\rm p}$ is the plasma volume.

Since the magnetic field $B_{\rm t}$ has an engineering limitation (< 20 T) and the plasma volume $V_{\rm p}$ should be kept small for an economical reactor, the improvement of the beta value is an important issue and the spherical tokamaks are one of the candidates for a high beta and economical reactor [8].

1.2.1 Spherical tokamak

A spherical tokamak (ST) is a kind of tokamak device, and its aspect ratio ($A = R/a$) is less than about 2, where R and a are the plasma major and the minor radii, respectively. A schematic comparison between the spherical tokamak and the conventional tokamak is shown in Fig. 1.2. The concept of the ST was proposed by M. Peng and D.J. Strickler in 1984 [9]. They theoretically showed that the advantages of an ST: natural elongation, high $I_{\rm p}$ and good stability.

The first spherical tokamak experiments with hot plasmas was performed in START [10] at Culham, and a high $\beta_{\rm t}$ was demonstrated.

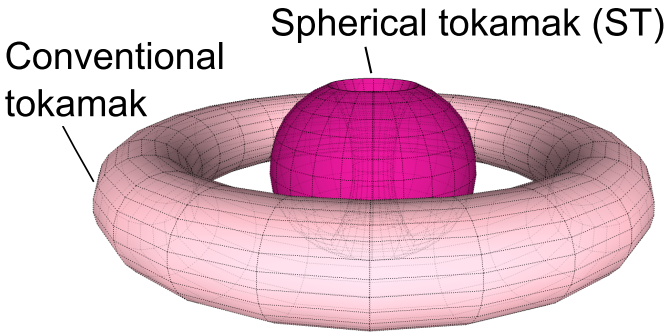

Figure 1.2: The shape of a spherical tokamak (inner torus) and a conventional tokamak (outer torus).

1.3 Non-inductive plasma current drive methods

The magnetic configuration for a tokamak needs plasma current to make poloidal magnetic fields. In most tokamaks, plasma current is driven by the (uni-directional) toroidal electric field induced by a central solenoid (CS). Since the maximum flux swing (i.e., the product of the loop voltage and the duration) is finite, the CS can produce loop voltage only for a finite duration. For long pulse operation, plasma current must be driven non-inductively, and (i) neutral beam injection (NBI), (ii) helicity injection and (iii) radio frequency (RF) waves are used for that purpose [11].

NBI is one of the heating and current drive methods, which is widely used in fusion devices. In NBI high energy neutral particles are injected into the plasma, then the neutral particles experience charge exchange reactions with ions in the plasma, and the energy of the plasma is increased as a result. The efficiency and the location of energy deposition depends on the density (and temperature) of the target plasma. If the plasma is too rarefied the particles penetrate through the plasma without depositing energy, and if the plasma is too dense the energy is deposited at the edge region, where the confinement of high energy ions is poor. Thus, the target plasma must have an appropriate density, which also depends on the beam energy.

Electron cyclotron wave (ECW) and lower hybrid wave (LHW) are major methods for non-inductive plasma current start-up and ramp-up using RF waves [12]. The first RF start-up experiments were performed in the WT-2 tokamak at Kyoto university [13,14]. Electron Bernstein wave (EBW), which is converted from the ECW is used also for ionization and heating of initial plasma because of the characteristic that the ECW can propagate in vacuum and in low density plasmas. In JT-60U, plasma current ramp-up using a combination of ECW and LHW with a small contribution of inboard coils was demonstrated in 2002 [15,16] and fully CS-less start-up was successfully achieved in 2004 [17].

The first non-inductive plasma current start-up and sustainment of an ST configuration was demonstrated on the CDX-U ST [18,19]. Similar non-inductive current start-up experiments have been performed on several STs, such as TST-2 (The University of Tokyo) [20], LATE (Kyoto university) [21, 22], QUEST (Kyushu university) [23,24], NSTX [25], MAST [26,27], and etc. These experiments were performed using ECW. Non ECW plasma current were performed on TST-2; high harmonic fast wave (HHFW) [28] and LHW [29] were used and successful plasma current start-up and sustainment of ST configurations were shown.

1.3.1 Review of lower hybrid current drive experiments in tokamaks

As described in Sec. 1.3, lower hybrid current drive (LHCD) is one of the most effective RF current drive method in conventional high aspect ratio tokamaks, and thus, the LHCD has been studied on several ST devices including TST-2 at the University of Tokyo.

The LHW is an electrostatic wave, and it can accelerate electrons directly through a process of a Landau damping.

The first LHCD experiments were performed on several tokamaks around 1980 and non-inductive current drive was experimentally verified by injecting LHW to OH plasmas (i.e., inductively current driven plasmas) [30–33]. In 1983, a plasma current over 100 kA was generated and sustained by LHW alone on the conventional tokamak PLT with the power of 200 kW at the frequency of 800 MHz [34]. The PLT experiments exhibited good agreement between theory and experiment but their plasma density was relatively low ($n_\mathrm{e} < 10^{19}$ m^3).

An LHCD experiment at the high density, more relevant to the reactor regime, was performed on the Alcator-C tokamak at MIT and the theoretical scaling law of the current drive efficiency was confirmed [35, 36]. These experiments suggest that there is no absolute density limit as long as the density is not reached to the mode conversion density, above which the LHW cannot propagate into the plasma core, but the efficient current drive is obtained only when $\omega > 2\omega_\mathrm{LH}$. Here, ω is the launched wave frequency, ω_LH is the lower hybrid resonance frequency defined as

$$\frac{1}{\omega_\mathrm{LH}^2} = \frac{1}{\Omega_\mathrm{i}^2 + \omega_\mathrm{pi}^2} + \frac{1}{|\Omega_\mathrm{i}^2 \Omega_\mathrm{e}^2|},$$

$\omega_\mathrm{pi} = (n_\mathrm{i} e^2 Z_\mathrm{i}^2 / \varepsilon_0 m_\mathrm{i})^{1/2}$ is the ion plasma frequency, $\Omega_\mathrm{i} = q_\mathrm{i} B / m_\mathrm{i}$ is the ion gyro-frequency, and $\Omega_\mathrm{e} = eB/m_\mathrm{e}$ is the electron gyro-frequency [37].

Because of the high LHW frequency (4.6 GHz) and the high magnetic field (11 T), the inequality $\omega > 2\omega_\mathrm{LH}$ yields $n < 3{\times}10^{20}$ m^{-3} so that the efficient current drive regime is satisfied [38,39]. Although the propagation of LHW is theoretically clarified, understanding of its behavior in high density plasmas is still inadequate. In the experiments conducted on Alcator C-Mod device, the current drive efficiency at the high density was much smaller than what would have been predicted based on the empirical rule from prior experiments and also by a numerical simulation [40, 41].

The density limit for efficient current drive is a function of magnetic field strength, and is low at a low magnetic field strength. For this reason, it was thought to be difficult to use the LHW in STs, which are characterized by high density plasmas confined by low magnetic field strengths. However, it can be used in STs as long as we can keep the density at a low level. Thus, it is important to clarify the effect of density and to clarify the usefulness of LHW current drive in STs.

LHW current drive experiments on the STs have been performed on TST-2 [29] and Globus-M [43, 44].

1.4 The TST-2 spherical tokamak

The Tokyo Spherical Tokamak-2 (TST-2) device (Fig. 1.3) was built at the University of Tokyo [45], after TST-M (Tokyo Spherical Tokamak Modified) [46]. It is a small spherical tokamak with plasma major radius $R_0 = 0.36$ m, minor radius $a = 0.23$ m, and aspect ratio $A = R_0/a \sim 1.6$. Its main parameters are listed in Table 1.2. In TST-2, a fully non-inductive start-up by LHW (200 MHz) has been investigated, and plasma currents up to $I_\mathrm{p} \sim 28$ kA have been achieved. The LHW is excited by capacitively-coupled combline (CCC) antennas (Fig. 1.4) located on the outboard- and the top-side of the plasma, and the antennas are fed by four power amplifier units with 100 kW output each (Fig. 1.5).

The outboard–launch CCC antenna (Fig. 1.4 (a)) was installed on TST-2 in 2013. The radial coordinate of the front surface of the antenna is $R = 621$ mm, and the vertical coordinate of the antenna center is $Z = 0$ mm (mid-plane). Antenna limiters with molybdenum (Mo) tiles are attached on both input and output sides of the antenna to protect the antenna from plasma, and its radial coordinate is $R = 585$ mm.

The top–launch CCC antenna (Fig. 1.4 (b)) was installed in 2016 [47]. The radial extent of the antenna is from $R = 139$ to 378 mm, and the vertical coordinate of the antenna surface is $Z = 435$ mm (originally installed at $Z = 335$ mm, and later updated to 385 mm and 435 mm [48, 49]).

Table 1.2: Main parameters of the TST-2 spherical tokamak.

Parameter	OH discharge	LHCD exp.
Major radius R_0	0.36 m	
Minor radius a_0	0.23 m	
Toroidal field B_t	0.3 T (@ $R_0 = 0.36$ m)	
Plasma current I_p	< 120 kA	< 28 kA
Electron density n_e	$< 2 \times 10^{19} \mathrm{m}^{-3}$	$< 10^{18} \mathrm{m}^{-3}$
Electron temperature T_e	< 400 eV (@ core)	< 40 eV (@ core)
Pulse duration	~ 50 ms	~ 120 ms

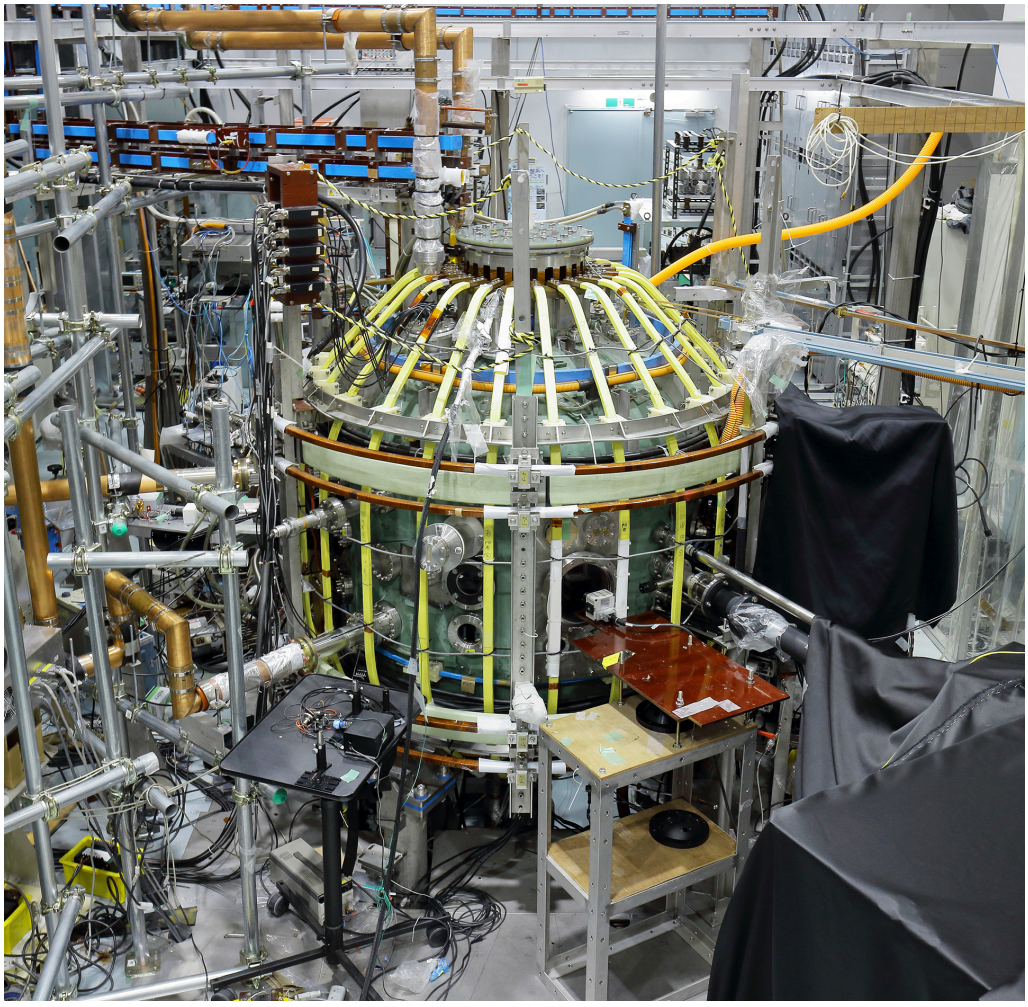

Figure 1.3: Photograph of TST-2.

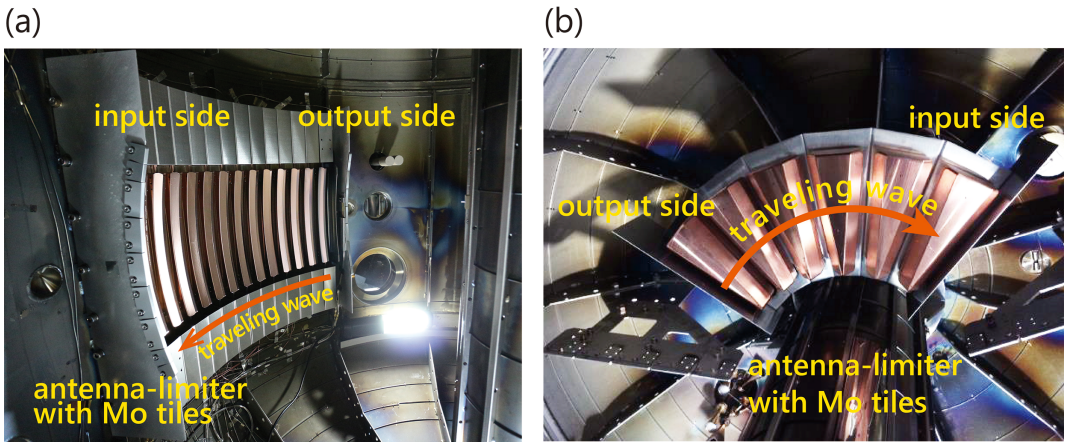

Figure 1.4: Photographs of the outboard–launch CCC antenna installed on the low field side (a), and the top–launch CCC antenna installed on the top of the plasma (b).

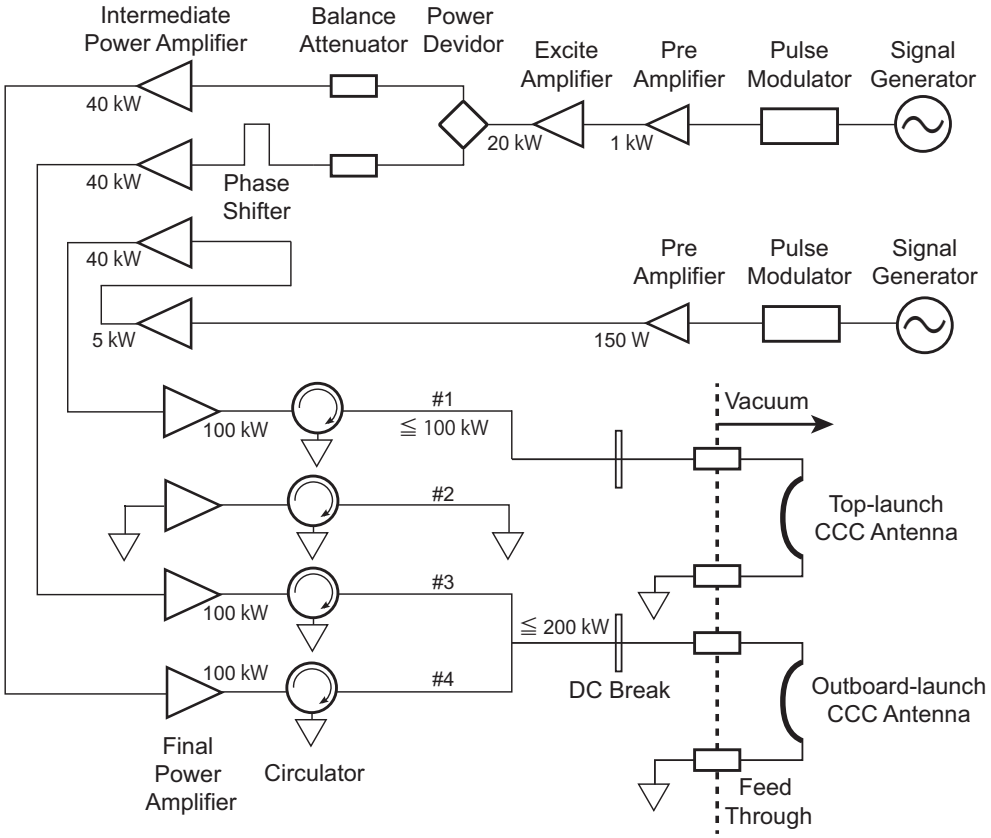

Figure 1.5: Block diagram of the 200 MHz RF power amplifier system.

1.5 Diagnostics and simulations

1.5.1 Diagnostics using x-rays

X-ray emissions contain a wealth of information about a magnetically-confined plasma and thus, lot of diagnostics have been developed. The non-thermal electron generated by RF current driven was confirmed by x-ray measurement [50]. Measurements can be classified into three types: (1) Pulse height analysis (PHA) for the photon energies from 1 to several hundreds of keVs, (2) X-ray imaging systems (XIS), and (3) X-ray crystal spectroscopy (XCS).

PHA method enables to obtain a histogram showing the number of x-ray pulses versus its photon energy. High energy x-ray emission from a fast electron during LHCD on the Alcator C tokamak was measured by PHA method for the first time in 1986 [36]. Although a time response is slow and a profile definition is poor, it is still widely used because of its good energy resolution for estimating electron temperature and impurity concentrations [51, 52]. In this work, HXR detectors using the PHA method is developed and used to measure the x-ray radiation from the fast electron generated by LHW on TST-2.

Soft x-ray tomography is one of the essential techniques of XIS, and can provide 2-D images of x-ray emissivity from the plasma [53]. A conventional SXR tomography consists of an array of diodes and metal filters, and each diodes (detectors) measure the line integrated brightness along several different sightlines, and a large number of algorithms have been proposed to reconstruct the plasma emissivity profile from the line integrated brightness. An analytical solution is known as the inverse Radon transform, and the x-ray tomography was demonstrated on JET tokamak in 1988 [54]. SXR tomography with different algorithms, such as the maximum entropy methods [55] and the Tikhonov regularization related pixel methods [56], are still being used for MHD instability and impurity transport studies on many devices [57–59].

XCS can measure the ion temperature and flow velocity profiles via Doppler broadening and line shifts with He-like ions of medium-Z impurities. Measurements of these parameters are important for optimizing plasma confinement thus, XCS have been installed in many large devices [60–67].

1.5.2 Plasma diagnostics on TST-2

Many instruments for plasma diagnostic are installed on TST-2. The plasma current and coil currents are measured by Rogowski coils surrounding the vacuum vessel and cables for each coil. Spatial profile measurements for electron temperature and density are provided by the Thomson scattering measurement [68]. A microwave interferometer is also used to measure the line-integrated electron density.

1.5.3 Simulation codes

PHITS

PHITS is a Monte Carlo code mainly developed by JAEA, KEK, and NIST, by which one can calculate particle transport in materials [69, 70]. PHITS is used for many purposes such as simulation of high energy physics, design of shielding structure of nuclear facilities, and calculation of neutron and x-ray emission from fusion plasmas.

EFIT, GENRAY and CQL3D

In TST-2, three computational codes are used for analysis of the plasmas. EFIT is an equilibrium reconstruction code [71] and provides information of the magnetic flux surfaces using the results of magnetic measurements. GENRAY is a ray-tracing code which calculates propagation and absorption of waves under the given plasma parameters, and CQL3D is a conservative finite-difference bounce-averaged Fokker-Plank equation solver [72].

1.6 Thesis objectives and outlines

The final target of this study is to clarify the heating process in spherical tokamak configuration and to explore a more efficient start-up method.

In the TST-2 spherical tokamak device, current drive experiment using LHW is carried out. As described in Sec. 1.3.1, LHW shows high current drive efficiency in conventional tokamak, but it is believed to be difficult to use in spherical tokamak. Since ST devices have various good characteristics, it is very important to investigate the behaviors of LHW in high density plasmas, and clarify the performance of LHW current drive in ST plasmas.

Information of x-ray radiation is important because it reflects electron population accelerated by LHW. Hard x-rays which has photon energies between a few tens of keV to several hundreds of keV are useful to get information of the effective temperature of fast electrons, and soft x-rays with energies up to approximately 20 keV are helpful to know about the impurity contamination.

Recently, in fusion research fields, pixelated x-ray detectors using CMOS sensor have been applied to x-ray spectroscopy and imaging measurements. PILATUS3 is one of the successor and it has an adjustable energy threshold for photon detection which can be decided individually on each pixel. This adjustable response on each pixel enables us to operate it with various arrangements and to select an energy range with or without line emissions. This system has a capability for measurements with a good spatial and temporal resolutions compared with conventional methods, but these resolutions strongly depend on their design and configurations such as pinhole camera geometry, energy threshold settings, exposure time, and etc.

The main objectives in this study are listed below:

1. To develop a several wide energy range (a few keV to several hundreds of keV) x-ray measurement systems and to investigate the spectrum under various conditions in order to investigate the fast electron transport and the energy loss mechanism in ST configurations.

2. To detect and identify soft x-rays from thick target emission which contaminates the x-ray radiation from the core plasma.

3. To simulate soft x-ray emission profile from fusion plasmas and to design the ME-SXR pinhole camera for several devices including TST-2.

This thesis is composed of six main chapters:

Chapter 2:
This chapter describes a theory about x-ray measurements and details of the developments of the x-ray measurements on TST-2. Results of calibration and test are also described.

Chapter 3:
Chapter 3 describes a multi energy soft x-ray measurements using the Pilatus detector. Methodology for calculating x-ray emission from a plasma, results of the calculation, and designs for several conditions are presented in detail. Experimental results are also discussed.

Chapter 4:
Results of LHCD experiments on TST-2 are presented in this chapter. SXR measurements for identifying the thick target radiation from vacuum vessel and HXR measurements for studying the fast electron transport are introduced.

Chapter 5:
This chapter discusses the results of x-ray measurements.

Chapter 6:
Summary and conclusions.

Chapter 2

Development of x-ray diagnostics on TST-2

2.1 Principle of x-ray spectroscopy

Plasmas emit electromagnetic radiation in a wide energy range, and its characteristic energy depends on the temperature, density and other parameters. X-rays are dominant emission from hot plasmas and thus, x-ray measurements have been used as one of the most important diagnostic tools for fusion plasmas. X-rays can be divided into the low energy soft x-rays (SXRs) and the high energy hard x-rays (HXRs), and the following sections describe their features and measurement methods.

2.1.1 Soft x-ray measurements

X-rays with the photon energy from several hundreds eV to 10 keV are called soft x-ray (SXR). However, in magnetic confinement fusion field, the energies up to approximately 50 keV are often considered as being part of the SXRs. SXRs are emitted via charged particle interactions, which can be divided into three types; bound-bound, free-bound, and free-free interactions. Bound-bound interaction causes line emission, and both free-bound and free-free interactions produce the continuum component of SXR spectra (Fig. 2.1).

In hot plasmas, a soft x-ray spectrum consists of continuum parts and line emissions. For the former Bremsstrahlung (free-free) and radiative recombination (free-bound) are the dominant emission processes, while for the latter, the bound-bound radiation is the mechanism. These emissivities, which are the energy emitted from a unit volume per unit time and unit energy, are expressed as

$$\frac{dP_{\mathrm{FF}}^{i,j}}{dE} = 3\times10^{-15} n_{\mathrm{e}} n_i \left(\frac{n_{ij}}{n_i}\right) Z_{\mathrm{eff},i}^2 T_{\mathrm{e}}^{-1/2} \times g_{\mathrm{FF}}(T_{\mathrm{e}},E)\exp\left(-E/T_{\mathrm{e}}\right)\left[\mathrm{keV/keV/cm^3/s}\right] \tag{2.1}$$

$$\frac{dP_{\mathrm{FB}}^{i,j}}{dE} = 3\times10^{-15} n_{\mathrm{e}} n_i \left[\frac{n_{ij}}{n_i} Z_{ij}^2 T_{\mathrm{e}}^{-1/2} \beta_{i,j}(T_{\mathrm{e}},E)\exp\left(-E/T_{\mathrm{e}}\right)\right]\left[\mathrm{keV/keV/cm^3/s}\right] \tag{2.2}$$

$$\frac{dP_{\mathrm{L}}^{i,j}}{E_{\mathrm{L}}} \propto n_{\mathrm{e}}^2 \frac{n_i}{n_{\mathrm{e}}}\frac{n_{ij}}{n_i}\left\langle \sigma\nu\left(T_{\mathrm{e}},E\right)_{i,j}\right\rangle \tag{2.3}$$

where, subscription i and j represent an impurity ion i and a charge state j, respectively, n_{e} is the electron density, n_i is the total density of the i th ion, density ratio n_{ij}/n_i is the relative abundance of the j th charge state of the impurity i, $Z_{\mathrm{eff},i}$ is the effective charge of ion i, Z_{ij} is the charge of the ion i j before recombination, g_{FF} is the Gaunt-factor, the function $\beta_{i,j}(T_{\mathrm{e}},E)$ represents recombination from all quantum states, and $\left\langle \sigma\nu\left(T_{\mathrm{e}},E\right)_{i,j}\right\rangle$ is the total cross section averaged over a velocity distribution [73–75].

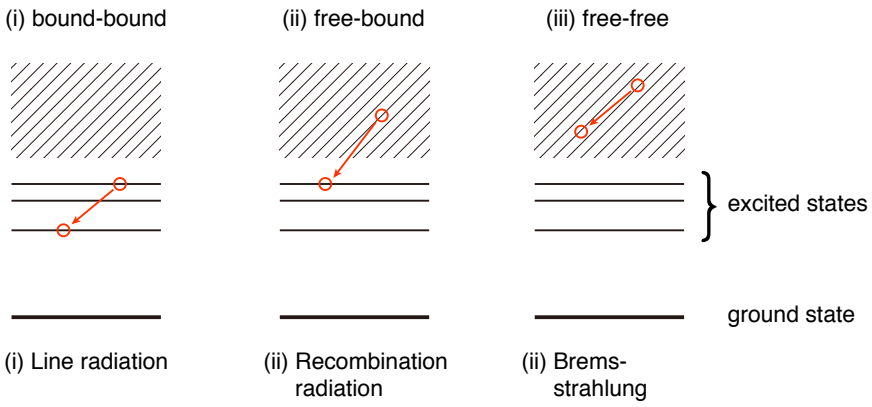

Figure 2.1: Three types of x-ray radiation process in plasma.

2.1.2 Hard x-ray measurements

High energy x-rays with the photon energies above 10 keV are called hard x-rays (HXRs), and are emitted by the electromagnetic radiation process known as Bremsstrahlung which is produced by a high energy electron decelerated in the electric field of an ion. In some configurations such as lower hybrid current drive (LHCD) or electron cyclotron current drive (ECCD) plasmas, a fraction of the electron population is accelerated to high energy range, and its distribution function is not the thermal Maxwellian distribution. HXR measurements are useful to obtain the information on the distribution function of such fast electrons.

Let us consider the fast electrons having a Maxwellian distribution function with an effective temperature of $T_{\rm eff}$, the spectrum of Bremsstrahlung energy $P_{\rm FF}$ (Eq. (2.1)) can be simplified as [75]

$$\frac{dP_{\rm FF}}{dE} \propto \exp\left(-\frac{E}{T_{\rm eff}}\right) [\text{count/keV/keV/s}],$$

where E is the energy [keV] of hard x-rays. Neglecting the weak E dependence of $g_{\rm FF}$ in Eq. (2.1), the slope of the spectrum in a semi-logarithmic plot becomes $1/T_{\rm eff}$. Therefore, the effective temperature $T_{\rm eff}$ can be estimated by from the HXR spectrum.

2.1.3 Scintillation detector

A scintillation detector is a standard device to measure the energy of each HXR. It consists of a scintillator crystal and a photomultiplier tube (PMT). A scintillator crystal emits visible scintillation light by absorbing an x-ray, and a photomultiplier tube attached on the scintillator detects the scintillation light and yields an amplified current pulse.

Scintillator

There are many types of scintillators: sodium iodide crystal doped by thallium (NaI(Tl)), cerium doped lutetium based crystal (LYSO, $Lu_{1.8}Y_2SiO_5 : Ce$), cerium activated lanthanum bromide ($LaBr_3$), etc.

An NaI(Tl) scintillator, first developed in 1948 by Hofstadter [76], is commonly used because of its several good features such as high scintillation intensity, ease of the fabrication of a large crystal, and low prices compared with other scintillators. The next generation scintillator such as LYSO and $LaBr_3$ are discovered in early 2000s. An LYSO:Ce was made from 90 % of $Lu_{1.8}SiO_5$ and 10 % of Y_2SiO_5 by Czochralski growth process in 2000 [77]. It is demonstrated that an LYSO:Ce has a few times faster scintillation light decay time and $\approx$ 75 % of the intensity compared to that of NaI crystal [77–79]. However, ^{176}Lu, an intrinsic

Table 2.1: Performance of typical scintillators [81].

Scintillator	Relative efficiency	Decay time [ns]	Wave length of a scintillation [nm]	Density [g/cm^3]
NaI(Tl)	100	≈ 250	415	3.67
LYSO	75	≈ 40	420	7.20
$LaBr_3$(Ce)	165	≈ 16	380	5.29

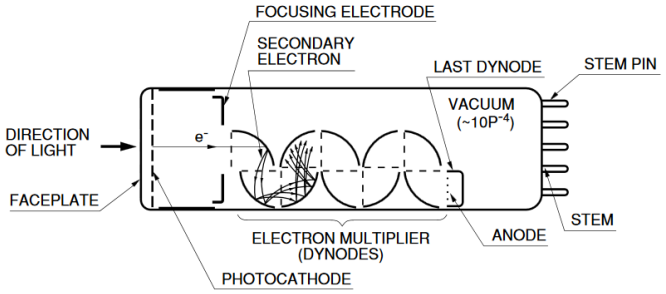

Figure 2.2: Schematic construction of a PMT [83].

radioactive isotope with an abundance of 2.6 % in the natural lutetium, decays β^- followed by the three γ-ray emissions with the energies at 88, 202 and 307 keV. As a result, a spectrum obtained by LYSO is "self contaminated" and thus LYSO is not widely used for x-ray measurements. In 2002, $LaBr_3$ was developed and it has been used for x-ray spectroscopy due to its good characteristics, much more shorter decay time and higher intensity, despite the small fraction of radio active isotopes, 0.09 % ^{138}La and ^{227}Ac, emitting γ-rays with the energies at 31–38, 789, 1436 and 1850-3000 keV [80]. The disadvantages of $LaBr_3$(Ce) are the shorter scintillation wavelength and the lower density. The former leads to lower signal and the latter leads to lower efficiency at high energies. Table 2.1 shows the performance of typical scintillators [81].

Photo multiplier tube

A PMT consists of an input window, a photocathode, dynodes which multiply electrons, and an anode, and it is sealed into a vacuum tube [82]. As shown in Fig. 2.2, the light emitted from scintillator induces photo-electrons at the photocathode, and then the electrons are accelerated and focused by dynodes. These electrons are finally collected by the anode, and provides a current signal to an external circuit. In principle, the number of scintillation light is proportional to the energy of the incident HXR, and the PMT yields current signal proportional to the scintillation light. Thus, the energy of the HXR is proportional to the output signal.

2.1.4 Semiconductor detector

For the energies less than about 100 keV, semiconductor detectors are commonly used. When an x-ray enters a detector, electron-hole pairs are generated and they can be extracted as a current signal. In many semiconductor detectors, the mean energy required for an electron-hole pair creation is around $3 - 4$ eV. In contrast, scintillators require an energy more than ten times larger than it to generate one photon. Due to the higher efficiency of a semiconductor detector, the number of the electron–hole pairs is much larger than the number of photons from a scintillator. As a result, the statistical error in the signal is small and the energy resolution is very high. Typical detectors are Ge, Si, CdTe, etc, and these detectors have very high energy resolution as described above. Most of these are cooled with liquid nitrogen to reduce thermal noise,

Table 2.2: Signal intensities and ratios for different filters.

Stainless steel			Molybdenum		
Filter	Intensity I [a.u.]	Ratio [%]	Filter	Intensity I [a.u.]	Ratio [%]
Cu:20 μm	8.12	$I_{\mathrm{Al}}/I_{\mathrm{Cu}} = 20.1\%$	Cu:20 μm	6.69	$I_{\mathrm{Al}}/I_{\mathrm{Cu}} = 79.7\%$
Al:600 μm	1.63		Al:600 μm	5.33	
Fe:10 μm	22.1	$I_{\mathrm{Al}}/I_{\mathrm{Fe}} = 17.6\%$	Fe:10 μm	12.4	$I_{\mathrm{Al}}/I_{\mathrm{Fe}} = 85.8\%$
Al:200 μm	3.88		Al:200 μm	10.7	

but a CdTe detector can be used at room temperature. The drawback of semiconductor detectors is that it is difficult to make a large detector, so that high energy HXR tends to penetrate through the detector without making electron-hole pairs. As a result the maximum sensitive energy is limited to $10 - 100$ keV.

2.2 Development of soft x-ray measurements

2.2.1 Thick target emission and filter selection

A main purpose of this measurements is the detection of the line emission from solid stainless steel which is irradiated by high energy electrons. All the x-ray measurement systems have its own line of sight and the detected signal reflects the emission not only from the electrons in the (rarefied) plasma, but also from the facing wall which is much more dense than the plasma. When high energy electrons hit the wall, it emits x-rays through Bremmsstrahlung in the wall material. The latter x-rays are referred to as thick target emission, and it can dominate the signal. In the case of TST-2 LHW sustained plasmas, high energy electrons can be generated at the edge plasma, and they produces thick target emission when they hit the wall. Therefore, it is quite important to estimate or measure the effect. Since the TST-2 vacuum vessel wall material is mainly stainless steel, and we can expect that the thick target emission contains spectral lines of iron and nickel. In order to see the contribution of such lines, we adopt an absorption method, in which thin foils with different materials are placed in front of an x-ray detector, and signals with different foils are compared.

Figure 2.3 shows thick target spectrum from both stainless steel and molybdenum calculated by the Monte Carlo transport code PHITS [69,70] as well as transmission curves of Cu (illustrated by green dashed curve) and Al (illustrated by red dashed curve) filters. According to the calculation results, the SXR detector with Al filter shows finite sensitivity at the energies above $\sim$ 8 keV, while the detector with Cu filter shows sensitivity at the energies of the characteristic line emission from the stainless steel in addition to the sensitivity for the detector with the Al filter. Energy flux can be estimated by

$$I = \int_{E_0=1\mathrm{keV}}^{E_1=50\mathrm{keV}} F(E) T_{\mathrm{filter}}(E) \mathrm{dE},$$

where, $F(E)$ is a spectrum calculated by PHITS as a function of photon energy E, T_{filter} is a transmission of the filter, Cu or Al, and the integration interval is from 1 keV to 50 keV. Thus, comparing the ratio between signal intensities of the two detectors with difference filters, we can quantitatively estimate the contribution of the thick target emission.

Since the signal intensity was expected to be small, another filter combination, 10 microns Fe and 600 microns Al, which have a transmission window in the same energy range as copper and higher transmittance were also selected. According to simulation results by PHITS, three times larger signal is expected by changing the filter combination.

The signal ratio between two filters are simulated by PHITS, and summarized in Table 2.2.

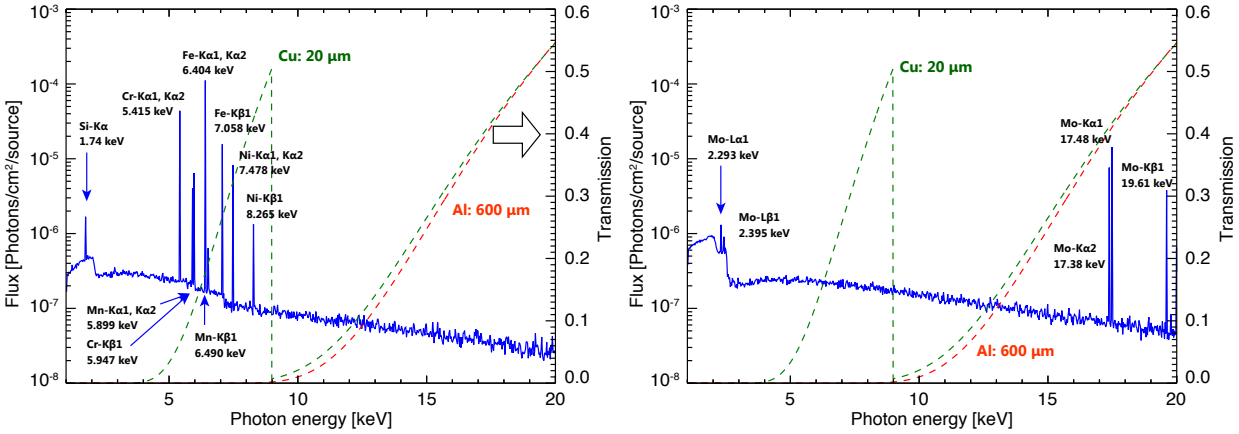

Figure 2.3: Thick target emission from stainless steel (illustrated by blue solid curve in the left figure) and molybdenum (illustrated by blue solid curve in the left figure) calculated by PHITS. Lines are identified in [84]. Transmission of Cu:20 μm and Al:600 μm filters are also depicted by green and red curves, respectively.

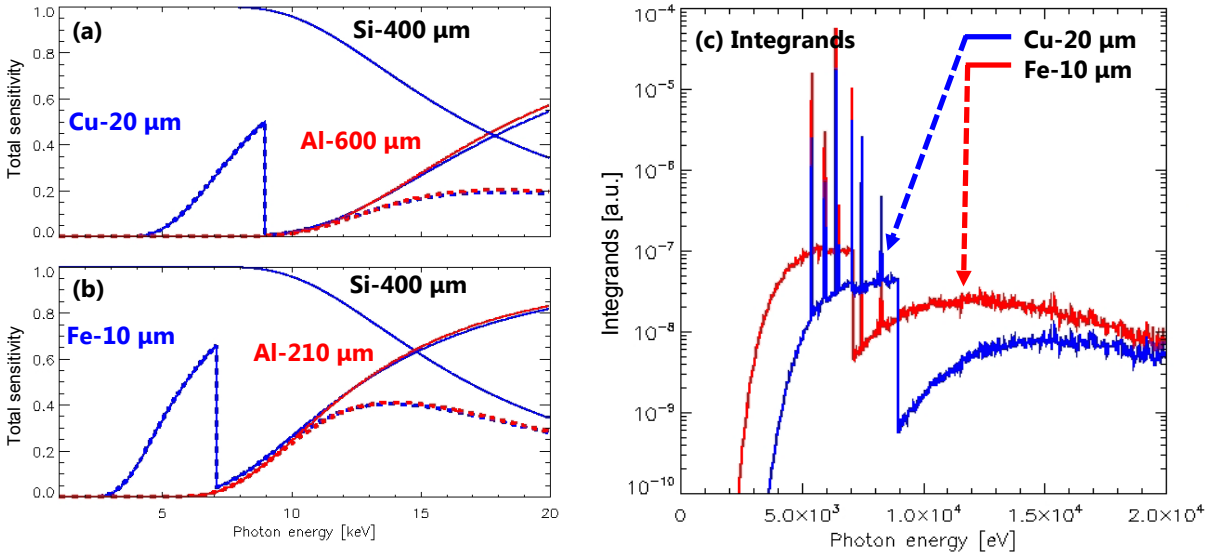

Figure 2.4: Comparison of transmission between Cu (a) and Fe (b). Integrands $F(E)T_{\mathrm{filter}}(E)$ are illustrated in Fig. (c).

2.2.2 Radial measurements using different filter

Two silicon surface barrier detectors (SBDs) are installed to a port on the mid-plane on TST-2. In this study, ORTEC R-015-050-10 (Fig. 2.5 (a)) connected on ICF114 flange was employed and filters described in previous section are attached on the detector (Fig. 2.5 (b)). Gate valve and Turbo molecular pump (TMP) are connected between flange and the TST-2 vacuum vessel so that the replacement of the filter is available without the vacuum break of the TST-2 vacuum vessel.

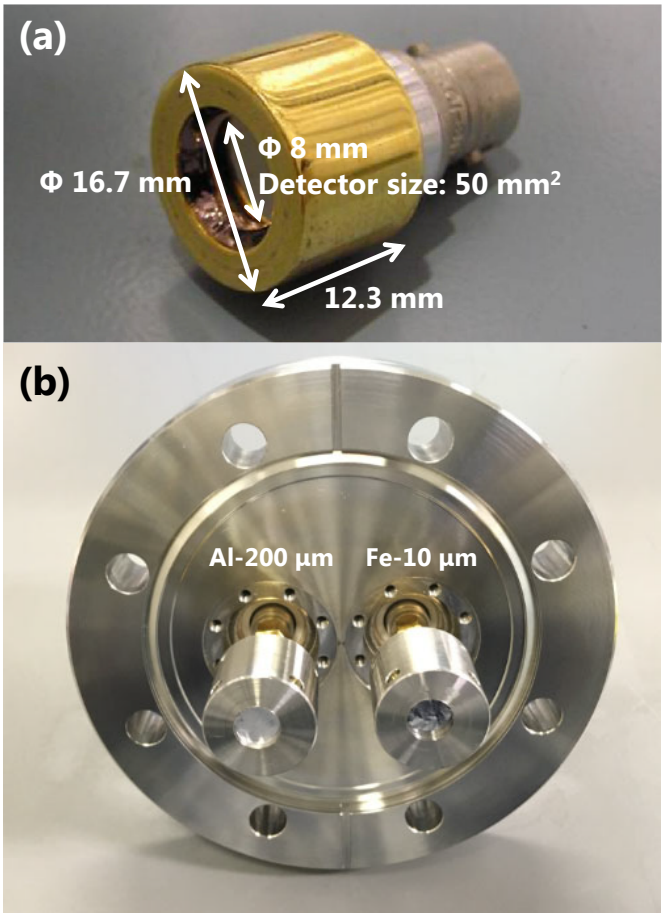

Figure 2.5: (a) Photograph of SBD and its dimensions and (b) two SBDs with different filters, Al and Fe attached on the vacuum flange.

2.3 Design and development of hard x-ray measurement systems

2.3.1 Components of HXR diagnostics

Most of the HXR diagnostic systems used for this work consist of a scintillator crystal and a PMT. The PMT cannot be used in a magnetic field due to the degradation of sensitivity (see Sec. 2.1.3), and therefore needs to be installed away from the coils of the TST-2 device that produces a strong magnetic field. In previous studies, scintillation light was transmitted to a distant PMT using an optical fiber or liquid light guide (LG), or whole system including scintillator crystal was located far from the machine [85]. However, the transmission efficiency is low because the smaller diameter compared to the scintillator crystal's diameter, therefore, in this study, an acrylic LG with the same diameter as the scintillator crystal was used [86, 87].

The scintillation light transmitted to the PMT, and its output current signal is converted into a voltage signal by a trans impedance amplifier circuit. This signal is sampled by 20 MS/s digitizer and its pulse heights are analyzed to obtain the HXR spectrum.

Figure 2.6 shows typical components of HXR diagnostics on TST-2. In this section, details of these components are described.

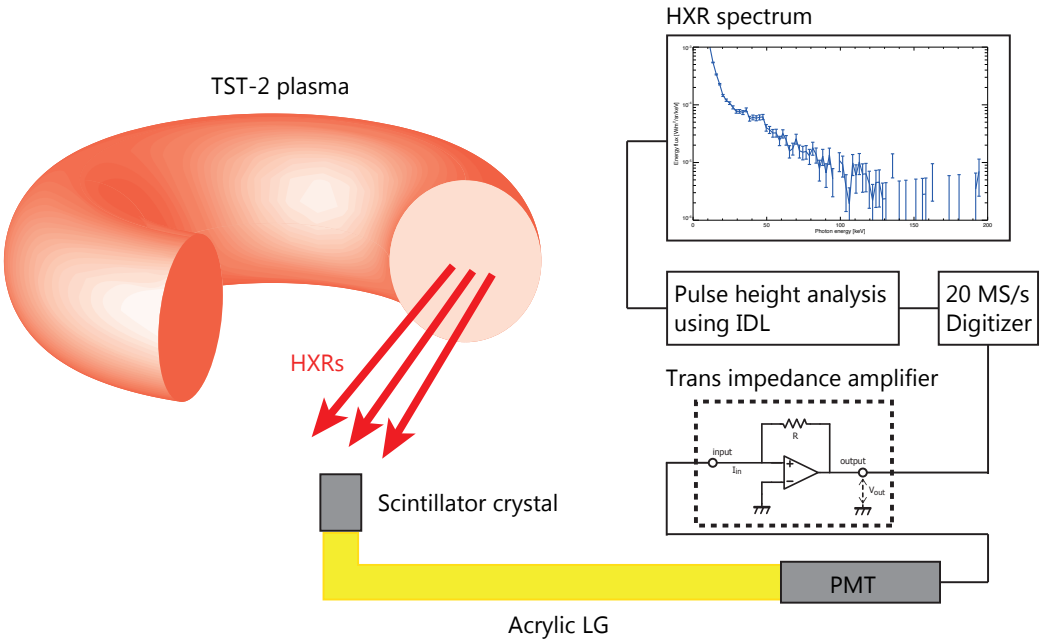

Figure 2.6: A schematic drawing of the HXR diagnostics on TST-2. HXRs emitted from TST-2 plasmas are measured by scintillator crystal and converted to the visible lights. The acrylic LG transmits the light to the PMT, which converts scintillation light into a current signal. The current signal is converted into a voltage signal by the trans impedance amplifier circuit, and amplified, and digitized. Pulse height analysis (PHA) is performed on a computer to obtain spectrum.

2.3.2 Electric circuit

Output current of a PMT needs to be converted to a voltage signal for digitizing. In order to measure the energy of the detected x-rays accurately with a good time resolution, we developed a fast response low noise two stage amplifier. The amplifier consists of a trans-impedance amplifier circuit for converting current to voltage and a non-inverting amplifier. Figure 2.7 shows a block diagram of a typical and ideal trans-impedance circuit and an actual circuit diagram of a trans-impedance amplifier in the first stage and a non-inverting amplifier in the second stage. Assuming the virtual ground in the ideal trans-impedance circuit (Fig. 2.7 (a)), the output voltage is expressed as $V_{\mathrm{out}} = -(I_{\mathrm{in}}R)$. However, in the actual configuration, input capacitance C_{in} which is composed of the cable capacitance (typically 50 pF/m), the floating capacitance and the input capacitance of the op-amp, deteriorates the performances of the circuit. In addition, the amplifier circuit becomes unstable and starts oscillation because of the phase delay arising from this C_{in}. A compensation capacitor C_{f} is connected to suppress the oscillation by phase advance [88,89]. The appropriate capacitance for C_{f} can be calculated as $2\sqrt{C_{\mathrm{in}}/(\pi R_{\mathrm{f}} G_{\mathrm{BP}})}$, where G_{BP} is a gain bandwidth product. Since the appropriate capacitor C_{f} is proportional to input capacitance C_{in}, C_{in} must be kept small for making a fast response circuit because the RC time constant τ of the circuit response is written as $\tau = R_{\mathrm{f}}C_{\mathrm{f}}$.

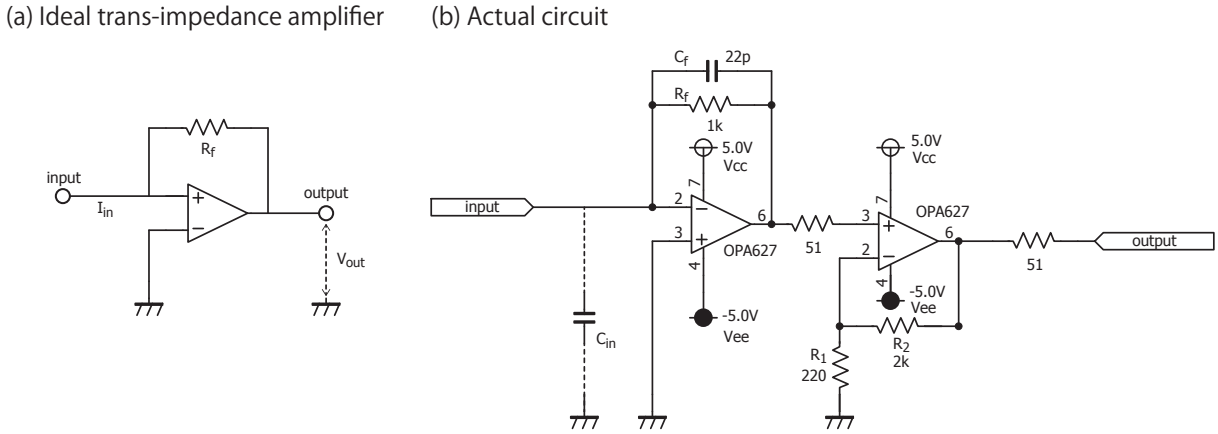

Figure 2.7: (a) Block diagram of trans-impedance amplifier circuit. (b) An actual circuit diagram of trans-impedance amplifier (first stage) and non-inverting amplifier.

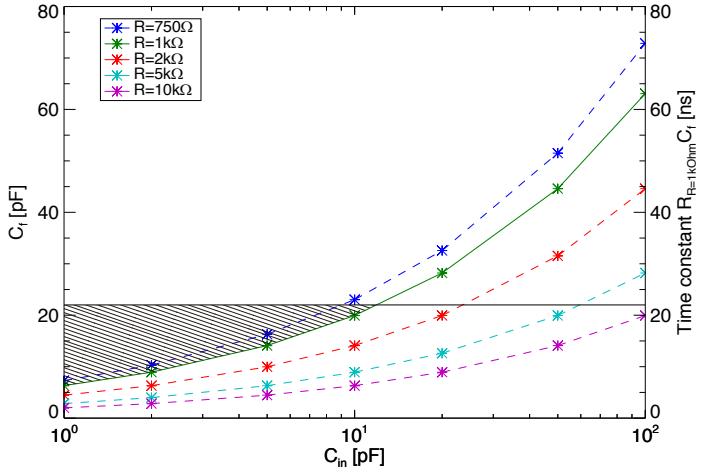

Figure 2.8: Appropriate values of C_f as functions of input capacitance C_in and resistance R_f scanned from 750 Ω to 10 kΩ.

In the circuit used for this work, two operational amplifiers OPA627 (Texas Instruments) are used, and C_in is estimated to be the order of 10 pF. Here, an appropriate C_f is calculated for five cases of feedback resistor R_f with the gain band width $G_\mathrm{BP} = 16$ MHz [90] in the range of C_in from 1 pF to 100 pF. Figure 2.8 depicts a stable C_f as a function of C_in and it shows that the stable C_f is located above each line indicating different R_f. In our circuit, 22 pF and 1 kΩ are selected for C_f and R_f, respectively, and thus, C_in must be smaller than 12 pF (illustrated by hatched region in Fig. 2.8) for stable operation. The band width f of trans-impedance amplifier is expressed as $f = 1/(2\pi R_\mathrm{f} C_\mathrm{f}) \approx 7.2$ MHz

The second stage of Fig. 2.7 (b) is non-inverting amplifier with the gain of $A = 1 + R_2/R_1 \approx 10.1$. Resistors are connected to the output of the two operational amplifiers in order to avoid oscillation due to the floating capacitance. Characteristics of entire circuit obtained from specification of each components are listed in Table 2.3.

Table 2.3: Characteristics of the trans-impedance amplifier for HXR measurements.

Op-amp	OPA627
Band width	≈ 7 MHz
Current gain	≈ 10 mV/μA
Noise	≈ 100 $\mu V_{\rm rms}$
Input impedance	1 kΩ
Output impedance	51 Ω

Table 2.4: List of parameters of $f_{\rm fit}$.

parameter	value	parameter	value
A	1.003	θ	3.0188×10^5
B	0.599	λ_1	3.8537×10^5
C	5.017×10^2	λ_2	6.9387×10^4

2.3.3 Pulse height analysis

The pulse heights of the output signal are proportional to the energy of each HXR detected by scintillator crystals. In order to identify the peak timing and to obtain the pulse height of each x-ray signal, we adopted the analysis algorithm in which a template pulse shape fitting is performed for each pulse.

Fitting method using parametrized function

A pulse shape of an output signal is shaped by RC circuit, thus it can be expressed using exponential terms. The process is as follows: first, a time window of the analysis is determined when the signal crosses the pre-determined threshold voltage. Second, we calculate amplitude $A_{\rm amp}$ from the peak value, and timing τ from the peak timing through fitting. The fitting function $f_{\rm fit}$ is written as

$$f_{\rm fit} = A_{\rm amp}\{Ae^{-\theta(t-\tau)} - Be^{-\lambda_1(t-\tau)} - Ce^{\lambda_2(t-\tau)}\}.$$

Here $A_{\rm amp}$ and τ are the fitting parameters for each HXR, and $A_{\rm amp}$ is proportional to the energy of the HXR. The fixed parameters $A, B, C, \theta, \lambda_1, \lambda_2$ depend on the PMT's gain and the preamplifier circuit. Example of these parameters are listed in Table 2.4.

Finally, the fitting function $f_{\rm fit}$ is subtracted from the original signal, so that the analysis for the following pulses are not affected by preceding pulses (Fig. 2.9).

This method is used in the pulse height analysis (PHA) of the measurements by a module type scintillation detector (OKEN, SP-10), and the fitting for an overshoot of a pulse (a voltage having a reverse polarity after the pulse) works well. However, when the fitting function is compared with the actual pulse, the reproduction of the rising part is not perfect (depicted by red circle in Fig. 2.9), and therefore, when determining the variable $A_{\rm amp}$, the fitting process was performed using the shape of an entire pulse. Therefore, in the case where the second half part of the pulse (i.e. between the time of the maximum and the time of the end of the pulse) is masked by the pulse pileup, the fitting accuracy is deteriorated. In addition, waveform of the fitting function is quite sensitive to fixed parameters $A, B, C, \theta, \lambda_1, \lambda_2$ and when we change the circuit (i.e., time constant or gain of the amplification), these parameters and the function $f_{\rm fit}$ should be recalculated.

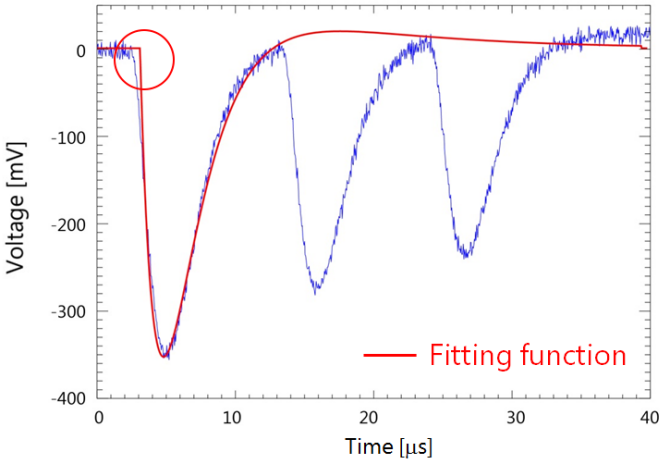

Figure 2.9: An example of the fitting process using a fitting function $f_{\rm fit}$. Since the reproduction of the function $f_{\rm fit}$ is not perfect, an error is included in the rising portion of the pulse indicated by red circle.

Fitting method using template waveform

Since the free parameters for each pulse are the amplitude ($A_{\rm amp}$) and the timing, a stored template waveform can be used for fitting $A_{\rm amp}$. The procedure is almost the same as that described in the previous section but a template waveform is used instead of a parametrized function.

1. A time window is determined when the signal exceeds the pre-determined threshold voltage.
2. A peak position and a pulse height are searched and the template waveform is fitted by adjusting amplitude $A_{\rm amp}$.
3. The fitted function is subtracted from whole signal in the time window then repeat the same procedure for following signals.

Figure 2.10 shows fitting processes for a pileup signal. The original signal is illustrated by blue curve in Fig. 2.10 (a), which is fitted by the template waveform (cyan solid curve). This fitted template waveform (cyan solid curve) is subtracted from the original signal (blue solid curve), and the same steps are repeated for the remaining signal (red dashed curve in Fig. 2.10 (a) and blue solid curve in Fig. 2.10 (b)). Since this method uses only the the first part (i.e. from the time that the signal exceeds the threshold and the time of the maximum) of a signal for the fitting, it is possible to separate multiple pulses even for a pile-up signal. However, as shown in Fig. 2.11, in the case where two pulses are measured with very short intervals and the maximum value of the first pulse cannot be detected, the pulse heights are not correct and cause distortion of the spectrum (in Fig. 2.11, the pulse height of the first pulse should be ∼0.04 V but ∼0.065 V was stored instead, and the pulse height of the second pulse is also incorrect). In order to eliminate the incorrect pulse heights, a coefficient for judging the fitting result was used. This judgment coefficient (JC) is defined as the standard deviation of the residual $\rho_{\rm r}$ in the range between start of the time window and the peak position. In this work, the decision limit is set to be 10 % and thus, pulse heights with JC less than 10 % are used for making a spectrum. Figure 2.12 shows the comparison between fitting results with different JCs.

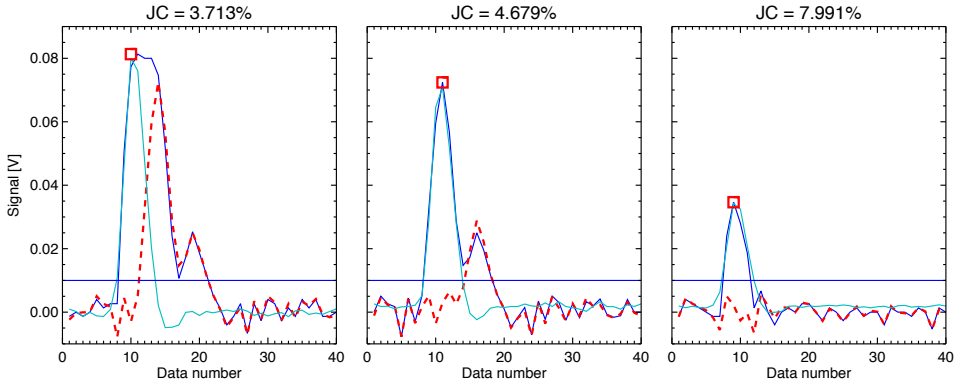

Figure 2.10: Results of pulse height analysis for pulse pile-up signal. A base signal (blue solid curves) is fitted by template waveform (cyan solid curves) and the pulse height A_{amp} is stored. The fitted template waveform is subtracted and signal is used for "next" base signal (red dashed curves).

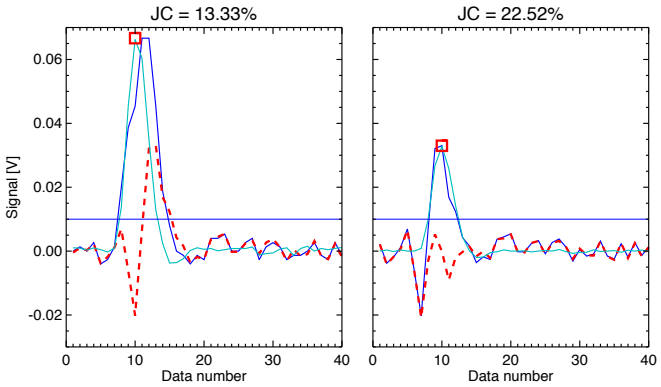

Figure 2.11: Results of pulse height analysis for a case where the two or more pulses are not separated. A fitting process for first pulse was failure and the pulse heights (indicated by red square) of first and second pulses are not stored because values of JC exceed upper limit (10 %).

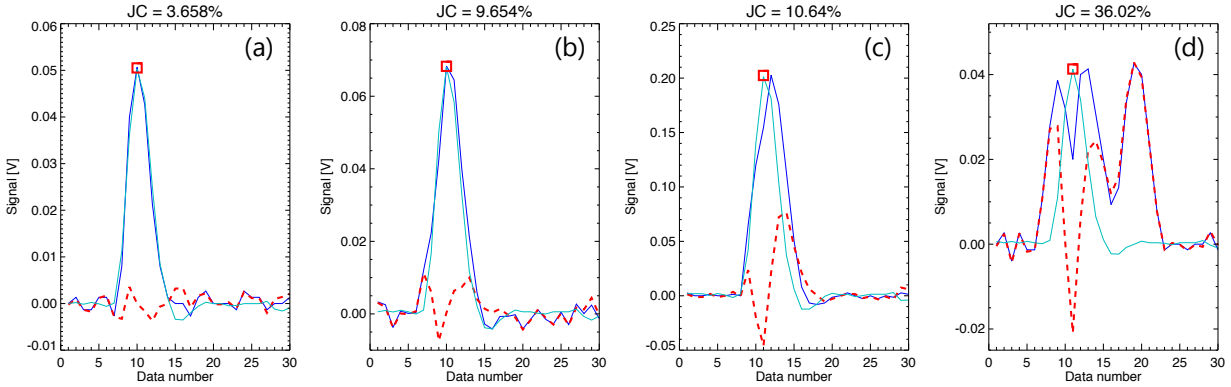

Figure 2.12: Comparison between fitting results with different judgment coefficient (JC). Decision limit of JC to use or not is 10 % and thus, result (a) and (b) are considered to be reasonable results while (c) and (d) are not.

Table 2.5: List of radioactive isotopes and energies of their photoelectric peaks. Effective peak energies were calculated by the averaged energy weighted by the emissivity when the energies of peaks are close.

Radioactive isotopes	photoelectric peak	effective peak energy
^{57}Co	122.0614 keV	∼124 keV
	136.4743 keV	
^{133}Ba	80.997 keV	∼81 keV
	276.398 keV	∼295 keV
	302.853 keV	
	356.017 keV	∼359 keV
	383.851 keV	
^{137}Cs	661.66 keV	∼662 keV

2.3.4 Calibration

By measuring x-rays radiated from radioactive isotopes having well known photoelectric peaks, the energy can be calibrated assuming that the x-ray energy is proportional to the pulse height.

We used three radioactive isotopes, ^{57}Co, ^{133}Ba and ^{137}Cs (Table 2.5). Since the energy resolution of the scintillator detector is several percent, when two photoelectric peaks have close energies, the peaks cannot be separated [81]. Therefore, for the two peaks of ^{57}Co and ^{133}Ba, the averaged energy weighted by the emissivity was used as the effective energy.

Figure 2.13 shows a typical photon detection result (blue curve in Fig. 2.13 (a)), pulse heights obtained by PHA (red square in Fig. 2.13 (a)), resultant spectrum for three radio active isotopes, ^{57}Co, ^{133}Ba and ^{137}Cs (top plot in Fig. 2.13 (b)) and relationship between output voltage and x-ray energies (bottom plot in Fig. 2.13 (b)).

2.3.5 Collimation and shielding

Shielding in HXR measurements is extremely important not only for limiting the field of view to be measured, but also for preventing spurious signals generated by the x-rays detected without passing scintillator crystal.

The shielding performance basically depends strongly on its density, thus a higher density material can stop HXR more effectively with a smaller volume. The most commonly used shielding material is lead due to its high density of $\rho = 11.34$ g/cm^3 and the low cost (see Fig. 2.14 (a) for comparison). In this study, we designed shielding materials using lead with the requirement of suppressing transmission of HXRs up to 300 keV to 0.1 % or less. Figure 2.14 (b) shows x-ray mass attenuation coefficients μ/ρ obtained from NIST database [91] (top) and transmittance of Pb with the thickness of 2.1 cm (blue curves in bottom) and 1.5 cm (red curves in bottom). Transmission calculation using x-ray mass attenuation coefficients (see also Sec. 3.1.2 for details of calculation) indicates that Pb with a thickness of 1.5 cm can be used as a shielding material for HXRs with the photon energy of 300 keV or less. However, considering the HXR scattering, the effective transmittance is not so good. The effect of the scattering is expressed by a build-up coefficient B. The build-up coefficient needs to be evaluated by experiments or simulations because it involves geometrical conditions as well as HXR energy, material composition and thickness. The build-up coefficient for simple geometries can be obtained from the Boltzmann equation and has been calculated for 26 types of shielding materials so far [92,93]. In the most simple case, build-up coefficients can be approximated as $B = 1+\mu\tau$, here μ and τ are the mass attenuation coefficient and the thickness, respectively [81]. Transmittance calculated using this build-up coefficients indicates higher transmission and 2.1 cm thickness Pb will be necessary for

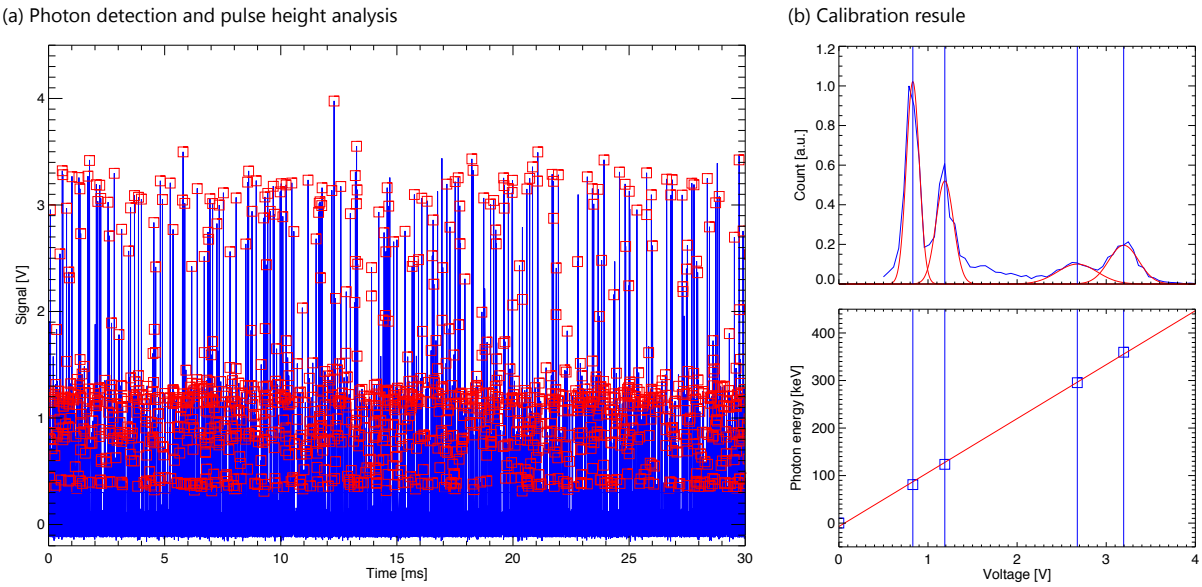

Figure 2.13: Results of photon detection (a) and calibration (b).

shielding HXR with the energy of 300 keV (shown in dashed curves in Fig. 2.14 (b)).

For HXR diagnostics of TST-2 plasmas, detectors are shielded and collimated by at least 2.0 cm thickness of lead. Note that the LG and PMT have a small sensitivity that is, x-ray like pulses are generated even in the case where the scintillator is not attached. Thus, whole detection system including LG and PMT should be shielded against not only visible light but also x-rays.

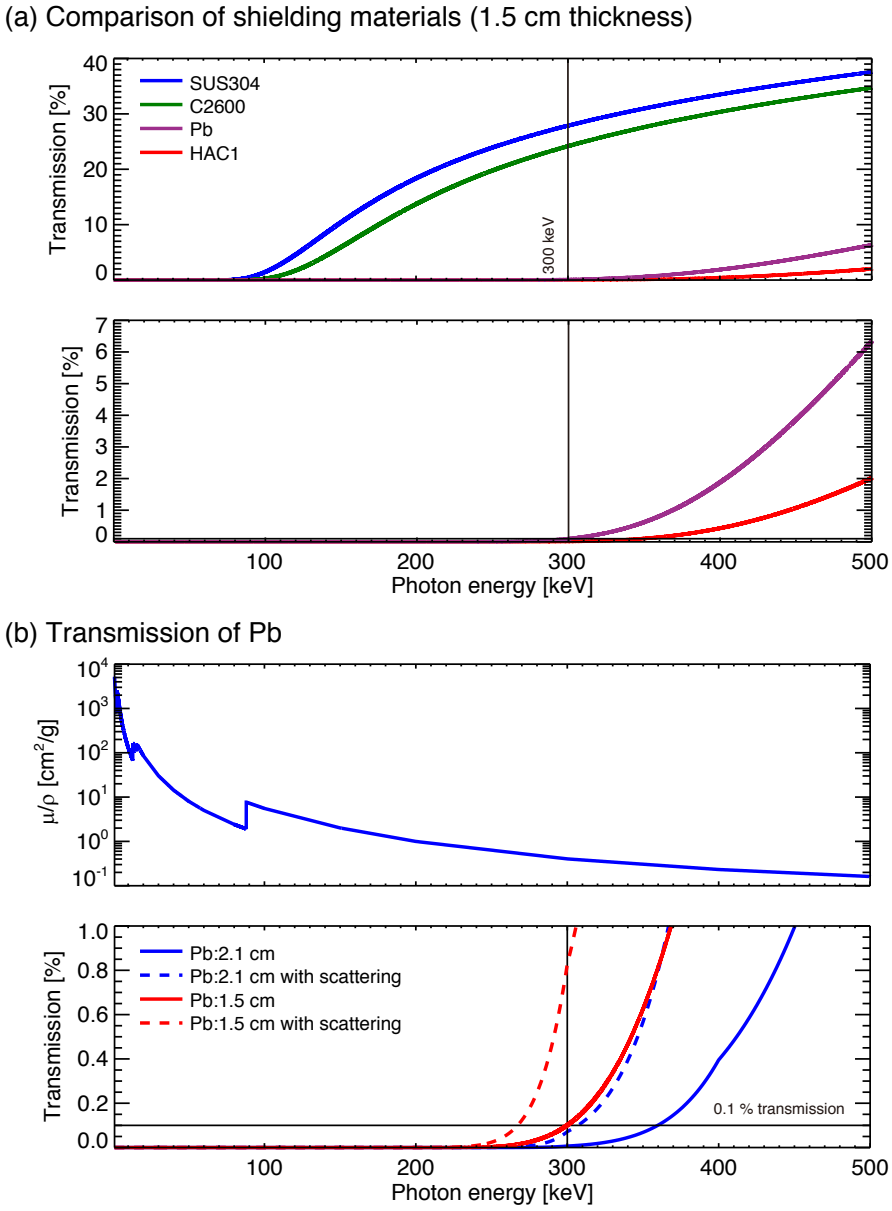

Figure 2.14: (a) Comparison between four metallic shielding materials with the thickness of 1.5 cm. HXRs with the photon energy above 100 keV can easily penetrate Stainless steel (blue curve) and Brass (green curve) while Pb (purple curve) and tungstain based heavy alloy (red curve) can suppress the transmittance at the photon energy of 300 keV to less than 0.1 %. (b) Transmittance of Pb with the thickness of 2.1 cm (blue curves) and 1.5 cm (red curves). The dashed curves show the transmittance including the scattering effect, and in the case of 1.5 cm, it exceeds 0.1 % for 300 keV HXRs while the transmittance of 2.1 cm Pb is not exceed 0.1 %.

PHITS calculations for evaluating effects of scattering

Scattering of HXRs deteriorate not only the shielding performance but also the absorption efficiency of a detector or a scintillator. In order to evaluate more realistic influence of the scattering, we calculated some arrangements of shielding material and scintillator crystal using the Monte Carlo code PHITS. Figure 2.15 shows two arrangements, placing the scintillator crystal near or far from the Pb collimator (Fig. 2.15 (a)) and the spectra expected to be obtained by the scintillator (Fig. 2.15 (b)). PHITS simulation indicates that when the scintillator is placed near the collimator (Arrangement #1), the resulting spectrum includes flux due to Compton scattering by the collimator between 150–300 keV and characteristic x-rays of lead around 10–30 keV and 90 keV [94, 95]. Therefore, it is favorable to put the scintillator sufficiently away from the collimator. However, it should be noted that the collimated beam should be smaller than the scintillator size and should be incident on the center of the crystal. Otherwise, the x-ray incident on the scintillator penetrates without being photoelectric absorbed.

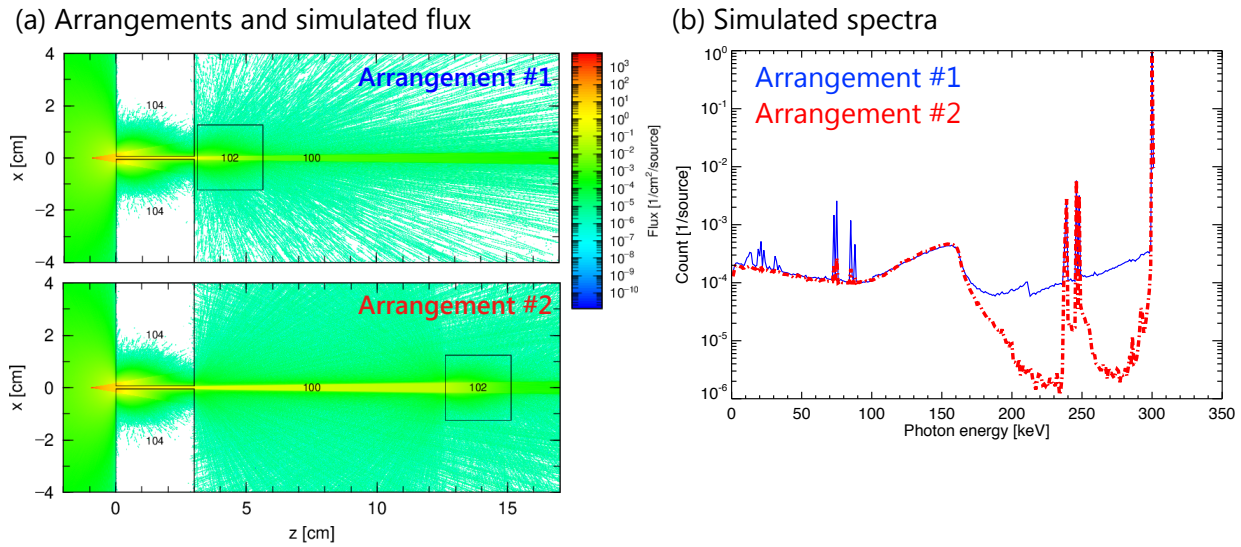

Figure 2.15: PHITS simulation for two arrangements of the position of collimator and scintillator (a). Here, indicies denote the materials (104: lead, 102: scintillator, 100: vacuum). 300 keV mono energetic XRs are injected from the point (x, z)=(0 cm, -1 cm). Spectra obtained by the scintillator for the source XRs of 300 keV are compared (b). Solid blue curve indicates arrangement #1 and dashed red curve indicates arrangement #2, and a larger influence due to scattering is observed for arrangement #1 (solid blue curve). Note that the spectra are normalized by number of x-rays impinging on the scintillator.

Lead glass for shielding back scattering x-rays

Since the scintillator crystal is connected to LG and PMT, x-rays incident from the photocathode behind the crystal can be a noise source. Lead glass, lead doped borosilicate glass, was tested for shielding material against a back scattering x-rays, which can shield x-rays injected to the crystal from the back, but can transmit scintillation light to LG or PMT. The characteristics of the lead glass are $\sim$ 85 % transmittance for 450 nm scintillation light, density of 4.36 g/cm^3 (c.f. density of standard borosilicate glass is $\sim$ 2.3 g/cm^3), and the effective thickness of lead is $\sim$ 2 mm for the tested lead glass.

Figure 2.16 shows the change of the spectrum by attaching the lead glass. While the signal intensity obtained was reduced by $\sim$37 %, the count rate of x-rays radiated from the radioactive isotopes put at the rear decreased from 250 cps to 80 cps in total. No signs of deterioration to the calibration spectrum are observed, thus the effect of shielding x-rays from the rear is confirmed.

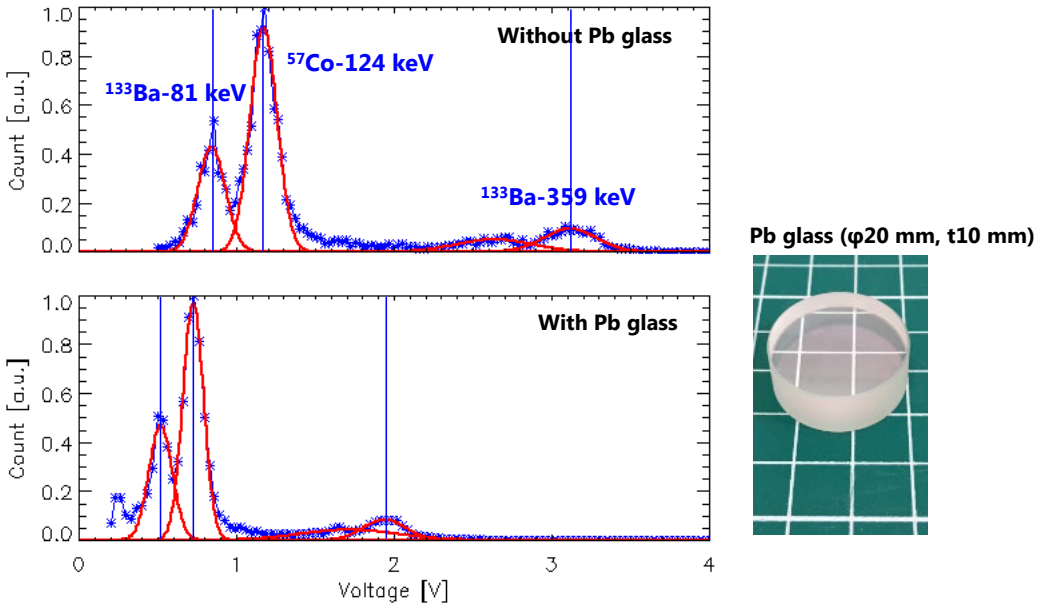

Figure 2.16: Spectra from radio active materials with and without lead glass. Photon signal is attenuated to ≈ 63 % of the original intensity.

2.3.6 Design of hard x-ray detector

Profile measurement system using NaI scintillator

We developed a hard x-ray profile measurements system using NaI scintillator, light guide (LG) made of acrylic and a PMT [86, 87]. It is installed on the mid-plane, and it can measure $R_{\rm tan}$ from 260 mm to 560 mm illustrated by red lines in Fig. 2.17. Since the PMT should be located far from the TF coils, scintillation light is transmitted by the acrylic LG.

Hard x-ray detector using LYSO scintillator

The short decay time of scintillation light and the high density are great advantages of an LYSO scintillator. An HXR detector using LYSO crystal have been developed and tested for expanding measurable count rate and energy range.

For taking advantage of the short decay time of the scintillation light, a fast trans–impedance amplifier circuit that can provide pulses 25 % faster in the rise time and 70 % faster in the decay time than the circuit used for NaI scintillator was developed (Fig. 2.18(a)). A higher density of LYSO enables more efficient measurement of high energy HXRs (see Fig. 2.18(b) for comparing x-ray sensitivities and Fig. 2.19 for PHITS simulation).

An HXR radiation due to the spontaneous decay of radioactive materials contained in LYSO crystals (Fig. 2.20 (a)) is one of the disadvantages, but as a result of PHA, the amount of radiation is about 3.5 kcps (Fig. 2.20 (b)) for this system. Since the count rate in the typical HXR measurements on TST-2 is several hundred kcps, it was found that the error due to the self contamination is about 1 %.

Figure 2.21 shows the calibration result using radio active isotopes ^{57}Co and ^{133}Ba. The self contamination spectrum of LYSO was also observed, suggesting that *in situ* calibration using this photopeaks is possible.

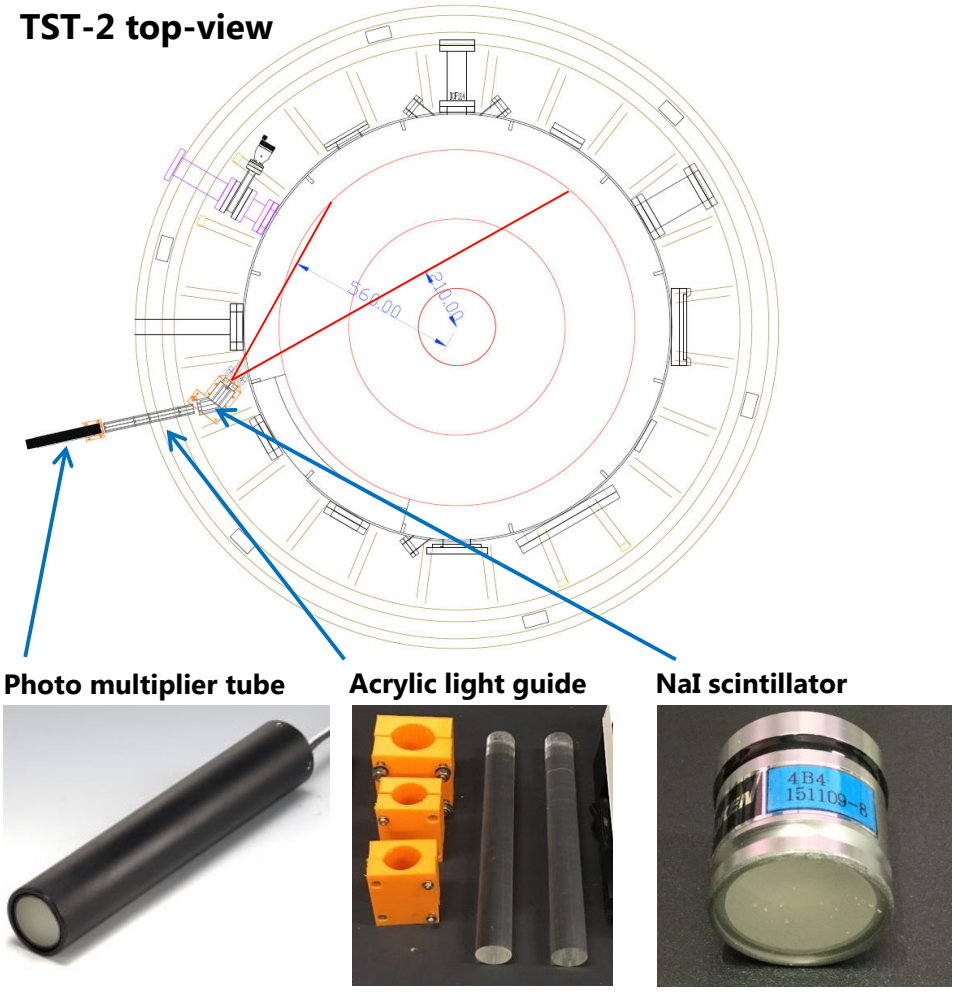

Figure 2.17: Schematic drawing of the top view of TST-2 and HXR profile measurements system installed on mid-plane. A measurable range is depicted by red line.

(a) Pulse shape comparing LYSO and NaI

(b) Comparison of x-ray absorption

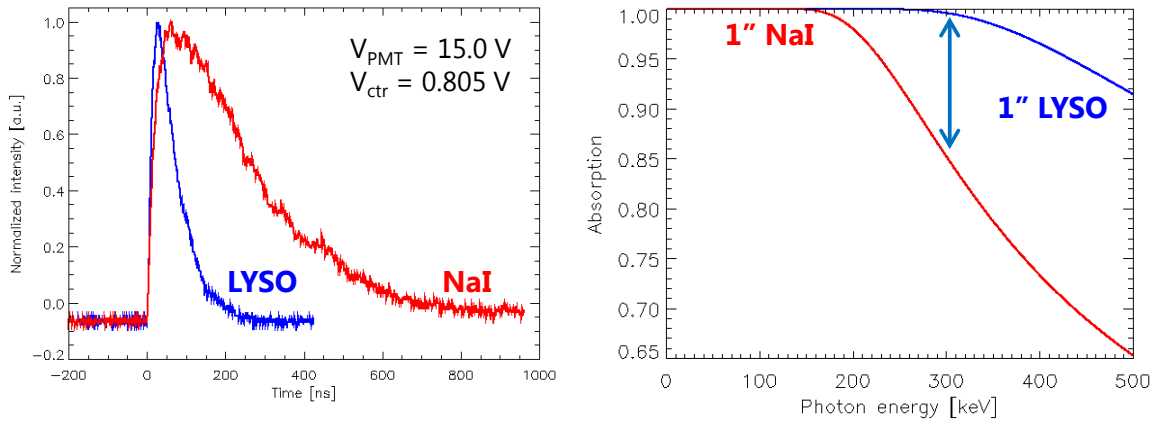

Figure 2.18: Comparison between LYSO and NaI scintillator. (a) A pulse shape from LYSO (blue curve) and NaI (red curve) scintillator. (b) Calculated absorption as a function of photon energy for scintillator thickness of 1 inch.

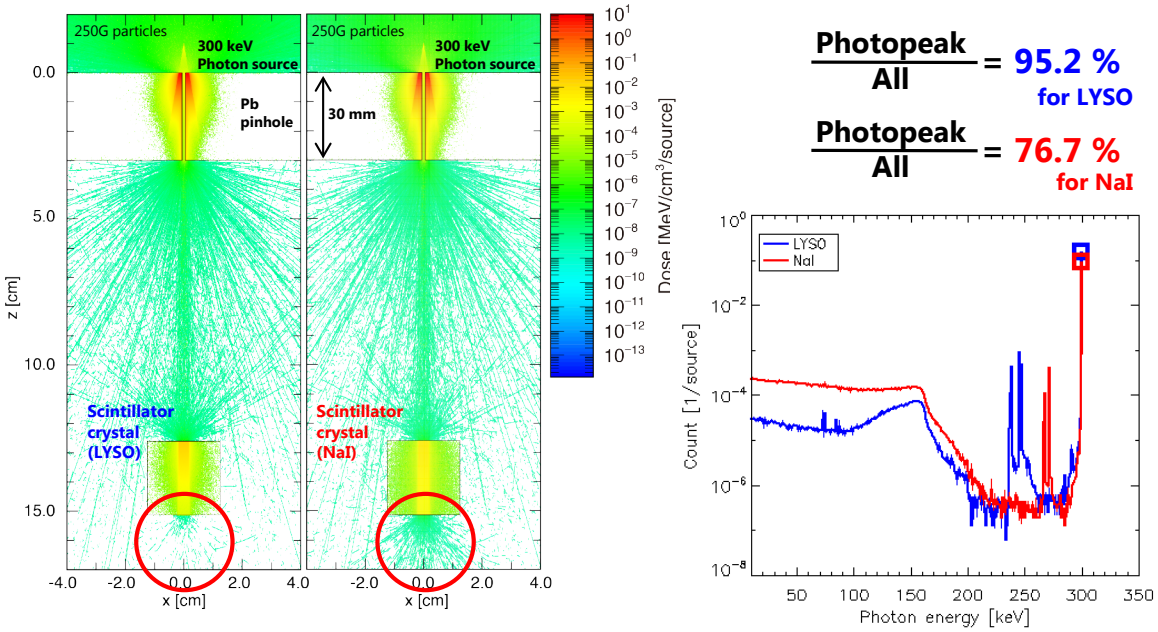

Figure 2.19: Comparison between LYSO and NaI scintillator. Influence of the scattering in the crystal was simulated by PHITS.

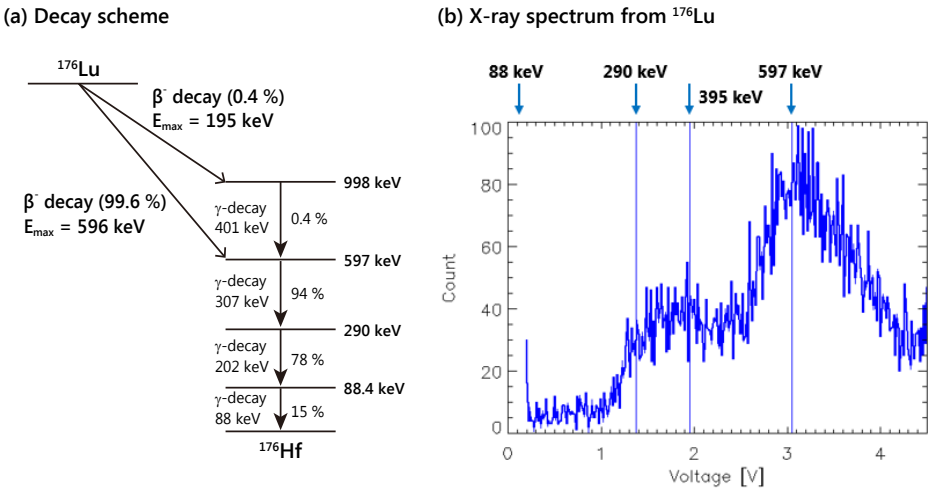

Figure 2.20: Decay scheme of ^{176}Lu in LYSO scintillator (a) and resultant spectrum of self contamination (b).

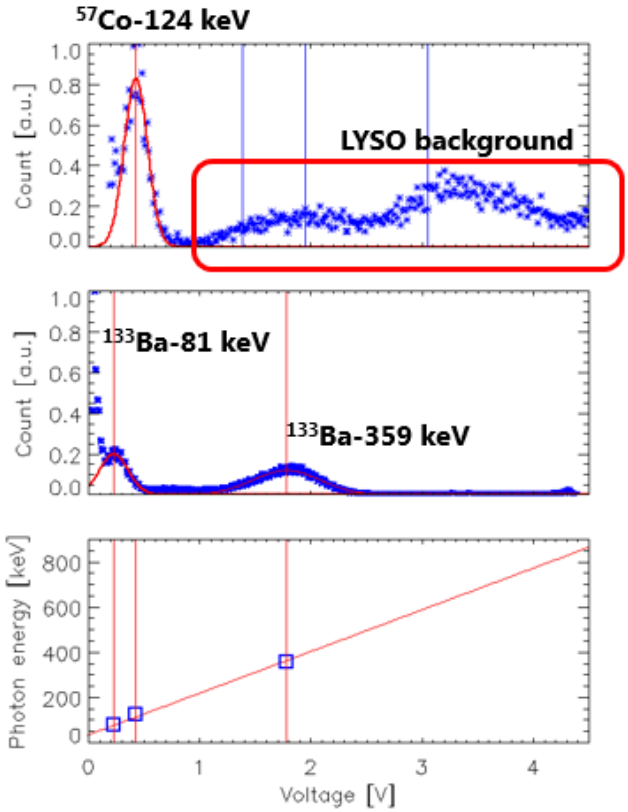

Figure 2.21: Energy calibration of an LYSO scintillator using radio active isotopes ^{57}Co and ^{133}Ba. Radiation from ^{176}Lu (shown in Fig. 2.20 (b)) contained in LYSO scintillator are also measured and photopeaks at 395 keV and 597 keV can be identified.

Vertical measurement using a PEEK flange

Polyether ether ketone (PEEK) is a semi–crystalline thermoplastic polymer with the chemical formula of $(–C_6H_4–O–C_6H_4–O–C_6H_4–CO–)_n$, of which features are good dimensional stability and dielectric strength (24 kV/mm), and excellent characteristics of flexural and elastic modulus [96, 97]. Outgassing rate is approximately 2–10 times smaller than Polyimide (PI, known as Kapton film) which is commonly used inside of vacuum [98,99]. In addition to these features, PEEK consists of the light atoms, hydrogen, carbon, and oxygen. These features can be used to make an ideal large area vacuum window for XR measurements.

A measuring system with a vertical sight line using a PEEK flange has been developed. The aims are not only to avoid metallic structures in the field of view, but also to measure HXRs with lower energies that cannot be measured in the conventional system by measuring through PEEK window.

The PMT must be located far away from the coils to avoid influence of the magnetic field. Compared to the measurement on the equator plane, the poloidal field (PF) coils make a strong magnetic field close to the vertical port, an atmospheric light transmission in a long distance is necessary, and acrylic LG and PMT with the same diameter as the scintillator crystal were used.

In order to measure lower energy HXRs, the PEEK flange must be as thin as possible while being able to withstand the pressure. Here the deformation of the center of the flange $\omega_{\max}$ due to the atmospheric pressure can be approximated [100] as,

$$\omega_{\max} = \frac{(5+\nu)R^4 p}{64(1+\nu)D}, \quad \sigma_{\max} = \frac{(3+\nu)R^2 p}{8\tau^2}, \tag{2.4}$$

where $D = E\tau^3/(12(1-\nu^2))$ (Fig. 2.22). We used the parameters listed in Table 2.6 [97] The limit of maximum displacement is assumed to be 10 % of the thickness τ (blue dashed line in Fig. 2.22) and the maximum stress is defined using the modulus of rupture of PEEK 80 MPa=80 N/mm^2 (red dashed line in Fig. 2.22). The thickness is decided to be $\tau = 6$ mm and the maximum displacement and the maximum stress are $\omega_{\max} \approx 0.7$ mm and $\sigma_{\max} \approx 12$ N/mm^2, respectively.

The x-ray transmittance of 6 mm thickness PEEK flange is illustrated in Fig. 2.23 (a) and the schematic drawing of the measurement configuration is shown in Fig. 2.23 (b).

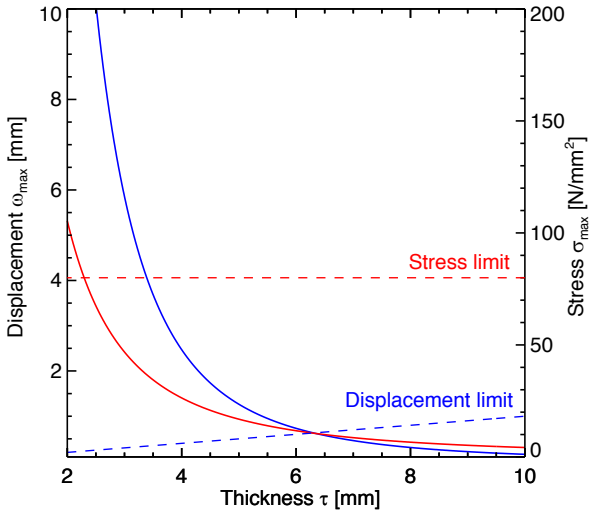

Figure 2.22: Calculated displacement (blue curves) and stress (red curves) using Eq. (2.4) as a function of the thickness of PEEK. The limitation values we assumed are illustrated by dashed lines.

Table 2.6: Parameters of the flange and the material properties of PEEK [97]

Property	Values
Pressure p	1 atm = 0.1 N/mm^2
Radius R	57.5 mm
Young's modulus E	4200 N/mm^2
Poisson's Ratio ν	0.4

(a) Transmittance of PEEK and SiO_2 window

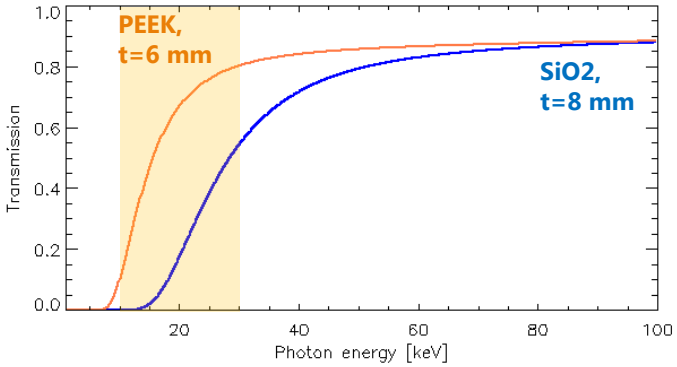

(b) Schematic drawing of vertical measurement with PEEK flange

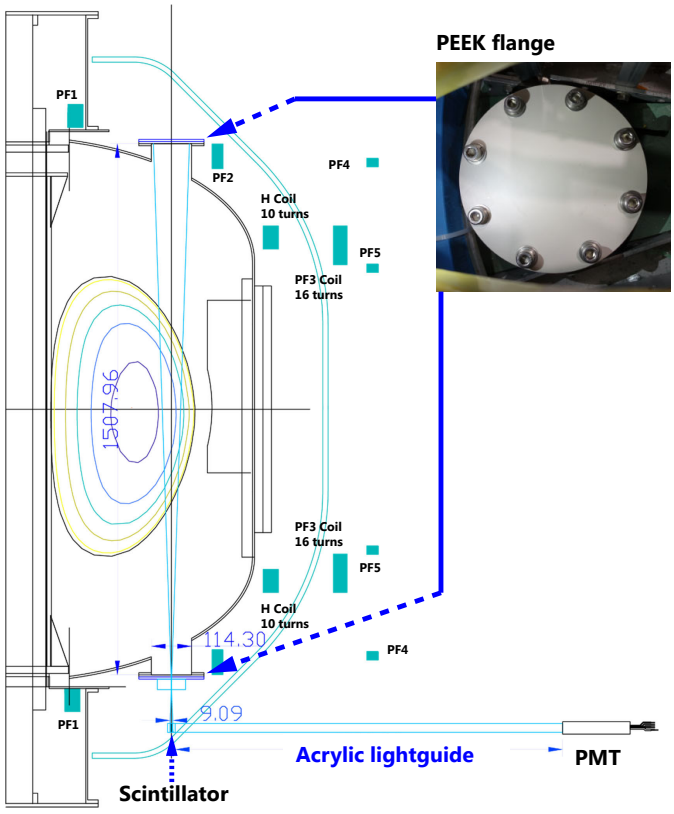

Figure 2.23: Schematic drawing of the poloidal cross section of TST-2 and diagnostic sight line.

2.3.7 Calibrations and tests for HXR measurements

Results of energy calibration of the detectors

In this section, calibration results are presented and reviewed. A method of calibration and the energies of photopeak are described in Sec. 2.3.4.

Figure 2.24 shows calibration results for two detectors using NaI crystal. Both detectors use the same NaI crystal, PMT and circuit, but without (Fig. 2.24 (a)) or with (Fig. 2.24 (b)) acrylic LG. The resultant plots show that in the case using acrylic LG (Fig. 2.24 (b)), the signal intensity is reduced to about 1/3, but the resolution and linearity are not deteriorated.

The calibration results of the detector using LYSO crystal are shown in the Fig. 2.25. Spectra show that the influence of the self contamination due to an ^{176}Lu contained in the crystal is negligible, that is, the count of photopeaks of ^{176}Lu is relatively small compared to the count of HXRs emitted from ^{133}Ba. Note that the HXR count from ^{57}Co is very low because it has been used for several years longer than its half-life time.

Comparing the spectra obtained by LYSO and NaI, the LYSO spectrum shows a smaller Compton edge (between the 81 keV and 359 keV peaks of ^{133}Ba) and a relatively larger count of 359 keV peak. This is due to the high density of LYSO, and it suggests that LYSO is suitable for high energy HXR measurements.

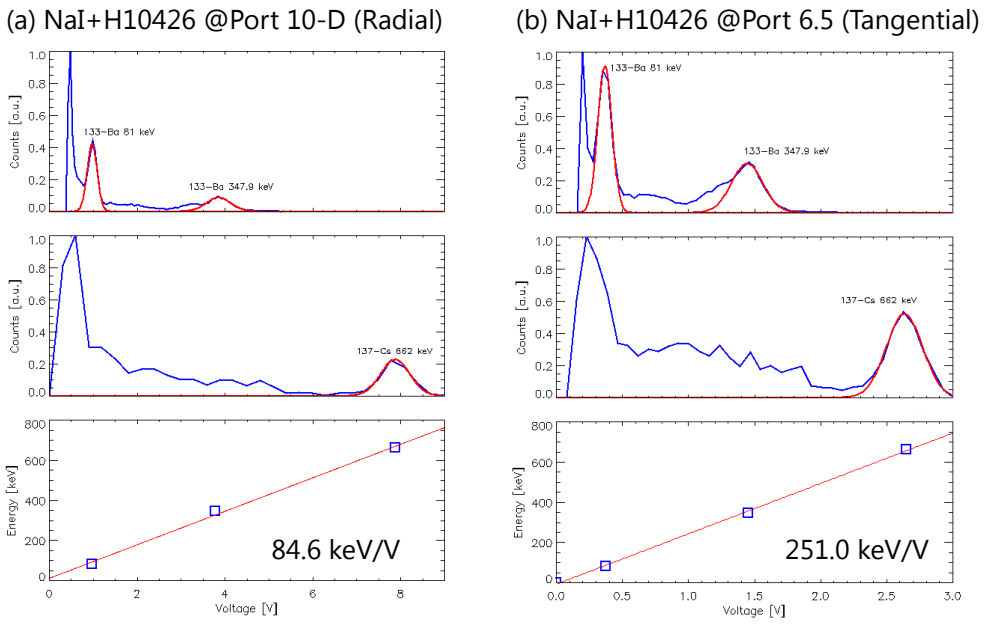

Figure 2.24: Result of calibration for two NaI detectors.

Tests of PMT sensitivity

A PMT's gain degradation due to magnetic fields is tested by inducing the magnetic field by poloidal magnetic field (PF) coil. Figure 2.26 shows results of scanning of the distance between PMT and PF coil and the align of PMT. Figures 2.26 (a) and (b) indicates that the PMTs should be oriented in a way that the ambient magnetic field is pointing in the PMT ' s vertical direction (direction-y illustrated in Fig. 2.26 (e)). Figures 2.26 (d) suggests that the distance of ∼1 m is necessary for avoiding influence of the magnetic field. The red curves in Fig. 2.26 indicate coil current of the PF coil.

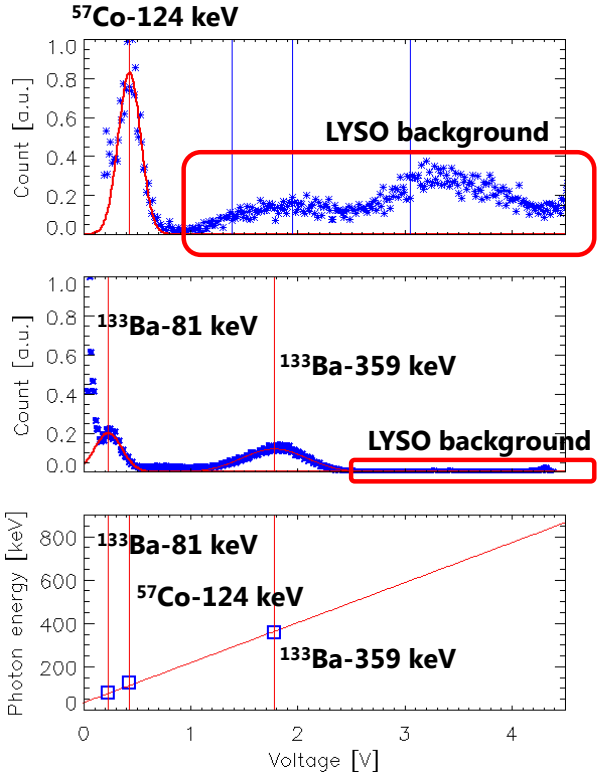

Figure 2.25: Result of calibration for LYSO scintillator.

Relationship between gain of PMT and applied control voltage was tested to make sure not to saturate the output signal. By the energy calibration, a control voltage of PMT for HXR measurements is set to be 1.0 V and thus, 0.9 V, 1.0 V and 1.1 V were applied and tested. The visible laser with an AM modulation of 1 kHz sine wave was used for the test, and the result indicates that the measured signal intensity (depicted by square in Fig. 2.27) completely traces the relationship shown in datasheet of PMT (solid curve in Fig. 2.27) [83] and there was no sign of saturation.

Noise estimation

In order to evaluate the performance of shielding and collimation, we compared two cases where the pinhole is shielded (illustrated by red curves in Fig. 2.28) and not (illustrated by blue curves in Fig. 2.28). The noise due to background x-rays, visible lights, and circuit noises, systems are also tested in a vacuum discharge.

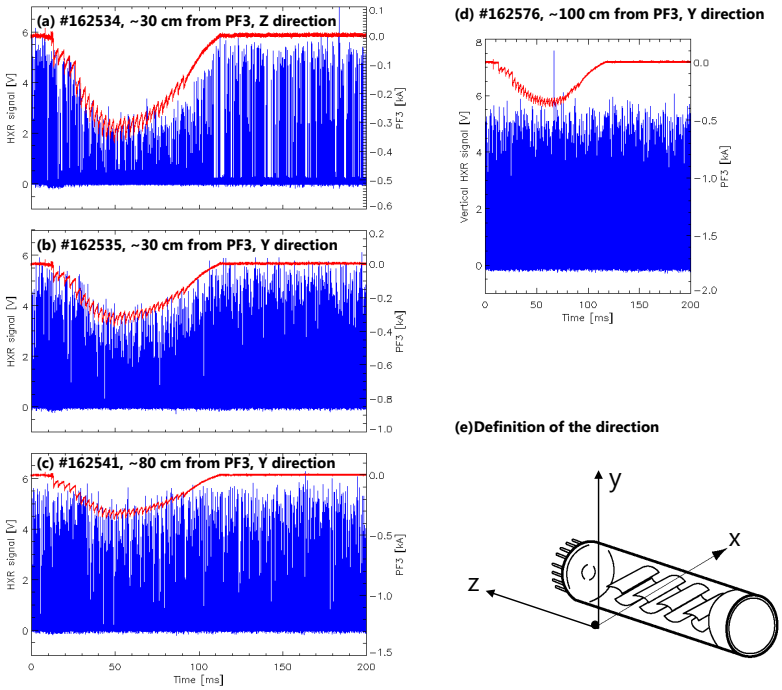

Figure 2.26: Signals of ^{133}Ba under the influence of the poloidal magnetic field. The gain sensitivity depends on the align and the distance. (a)-(c) Signal intensities decrease due to the magnetic field induced by PF3 coil. (e) No sign of decrease of the gain was found with the conditions of the distance of ∼1 m. (d) Definition of direction

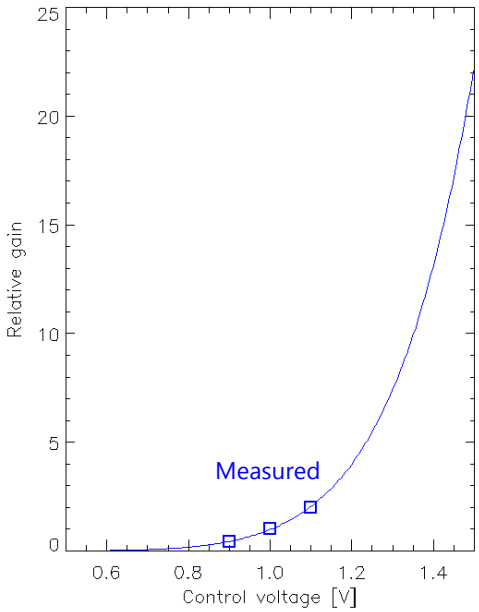

Figure 2.27: Sensitivity vs. applied control voltage. Solid curve indicates a relationship refered in datasheet and the blue squares indicate measured value.

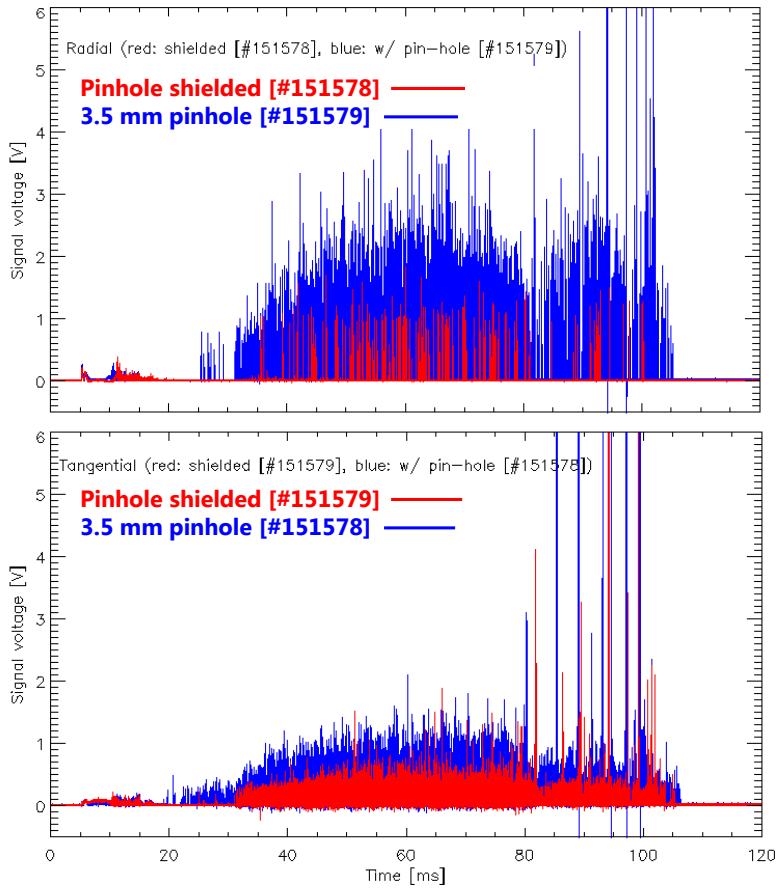

Figure 2.28: Evaluation of collimation.

Chapter 3

Multi energy soft x-ray imaging

With recent advances in x-ray detector, especially the CMOS based two-dimensional pixel array sensor, it is possible to measure x-rays in multiple energy ranges with high spatial resolution. A hybrid photon counting detector PILATUS [101–103] developed by CERN and Paul Sherrer Institute for synchrotron experiments, and commercialized by DECTRIS [104] is one of the successors and has been used for a multi-energy x-ray spectroscopy (Fig. 3.1). This detector has an adjustable energy threshold for photon detection decided individually on each pixel, which enables us to operate it with various arrangements that we can select an energy range with or without line emissions from plasmas.

In the fusion research, these detectors have been applied for x-ray crystal imaging spectrometers (XICS) in Alcator C-Mod [60–63], Large Helical Device (LHD) [64, 65], KSTAR [66] and EAST [67], and tested successfully for multi-energy soft x-ray (ME-SXR) cameras using second and third generation detector PILATUS2 and PILATUS3 in Alcator C-Mod [105, 106] and Madison Symmetric Torus (MST) [107–109].

This ME-SXR camera using PILATUS series of detector has a capability for simultaneously measuring a variety of plasma properties with spatial resolution, while the electron temperature T_e and $n_\mathrm{z}^2 Z_\mathrm{eff}$ can be inferred from the absolute intensity and shape of the continuum spectrum [111]. However, this resolution and signal to noise ratio strongly depend on their design and configuration. In order to satisfy the spatial, temporal and spectral resolutions, estimation of photons emitted from the target plasmas and impinging the pixel of the detector is necessary for their design. In addition, a highly accurate estimation of spectral resolved SXR radiation is necessary to decide and optimize a configuration of an adjustable energy threshold to bracket or eliminate a line emission from a certain impurity. Applying this technique and setting an appropriate energy thresholds, a simultaneous measurement of T_e, n_z and ΔZ_eff with high spatial, temporal and spectral resolution becomes possible.

For an analysis of experimental results, such calculations can be used to reconstruct $n_\mathrm{z}^2 Z_\mathrm{eff}$ profile by comparing spectrum of both continuum part and line emission part.

3.1 Modeling of x-ray emission from plasmas

In this section, methodology of calculation and modeling of x-ray emission from an arbitrary plasma is described. The objective of this calculation is obtaining a number of photons on each pixel of the detector. The total emitted power due to energy transitions could be theoretically obtained by calculating Bremsstrahlung (free–free), recombination (free–bound) and line (bound–bound) radiation using Eqs. (2.1)–(2.3). However, it is nearly impossible to calculate all line emission and recombination radiation for all impurities and charge states because of a large number of the free parameters. Thus, we adopt the following simplified code.

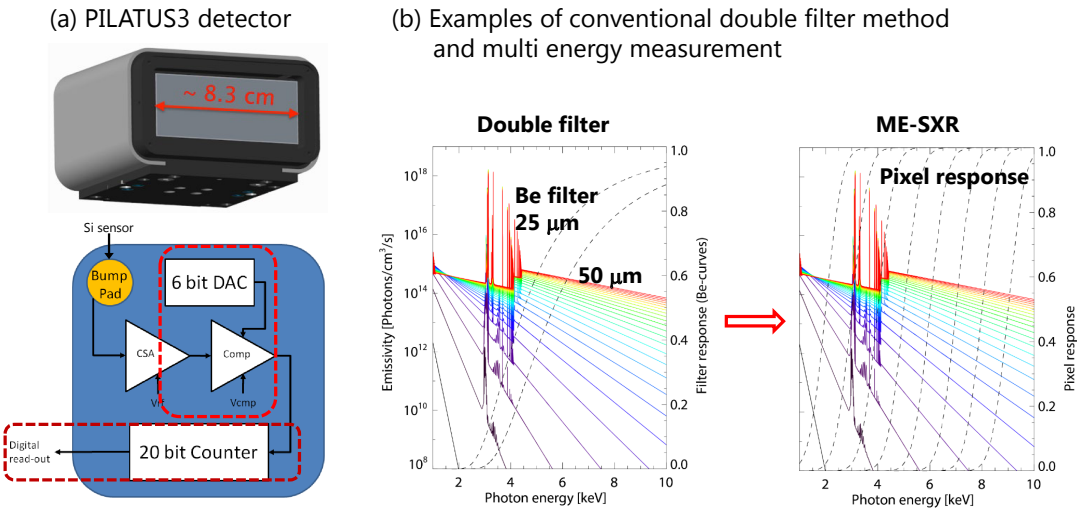

Figure 3.1: (a) Photograph of the PILATUS3 detector and a block diagram of photon counting circuit. (b) Comparison of the methods of conventional and novel SXR measurements.

In this work, spectra are calculated by the generalized collisional-radiative code FLYCHK [112, 113] developed by NIST instead of calculating equations listed above. In the FLYCHK, calculated spectrum F_Z for Z ion depends on the electron temperature, the electron density and the ion density.

3.1.1 Spectrum calculated by collisional-radiative code FLYCHK

In order to calculate soft x-ray emission from plasmas with arbitrary temperature and density, spectra and charge state populations for twelve different atoms, such as ${}_1$H, ${}_6$C, ${}_8$O, ${}_{13}$Al, ${}_{14}$Si, ${}_{18}$Ar, ${}_{21}$Ca, ${}_{26}$Fe, ${}_{28}$Ni, ${}_{42}$Mo, ${}_{54}$Xe, and ${}_{74}$W, were obtained from FLYCHK.

FLYCHK provides average charge state $\langle Z \rangle$ and charge state distributions as well as spectroscopic emissivity for a certain plasma parameters such as the atomic number of Z, electron temperature T_e and density n_e under local thermodynamic equilibrium (LTE) or non-LTE model. A similar collisional-radiative code FLY [114] had been used for analyzing spectra before FLYCHK was developed. While FLY was able to solve only for low-Z ions from helium ($Z = 2$) to iron ($Z = 26$), FLYCHK provides atomic level population distribution for mid- and high-Z atoms up to gold ($Z = 79$).

FLYCHK is a web-based software and a user should make an input configuration to get spectra for each parameters such as electron density, temperature and ion density. We have made and stored a huge database so that we can calculate spectra for an arbitrary plasma profile. Since the emissivity is proportional to both electron and ion densities, the database has been built at a single density $1.0 \times 10^{20}\mathrm{m}^{-3}$ but at multiple electron temperatures from 0.1 to 20 keV (note that the electron temperature range for silicon, aluminum, calcium and molybdenum is from 0.1 to 10 keV because the plasma including these impurities cannot reach a temperature exceeding 10 keV) and photon energies between 1.0 and 50 keV. The ion density used in the FLYCHK code is assumed to fulfill the quasi-neutrality as $n_\mathrm{i} = n_\mathrm{e} / \langle Z(T_\mathrm{e}) \rangle$ [115], therefore, the obtained emissivity scales with n_e^2 for a given T_e and concentration of impurities. Emissivity spectra for different elements and the n_e^2 scaling are shown in Fig. 3.2. Solid and dashed curves illustrate two different electron temperatures, 500 eV and 5 keV, and colors indicate electron densities from $1 \times 10^{18}\mathrm{m}^{-3}$ to $1 \times 10^{20}\mathrm{m}^{-3}$. Emissivity of both continuum and line emissions completely follow the n_e^2 scaling.

Figure 3.3 shows emissivities for twelve elements that we built the database as a function of photon energy E. The electron temperature T_e is scanned from 0.1 keV (shown by black curve) to 10 keV (shown

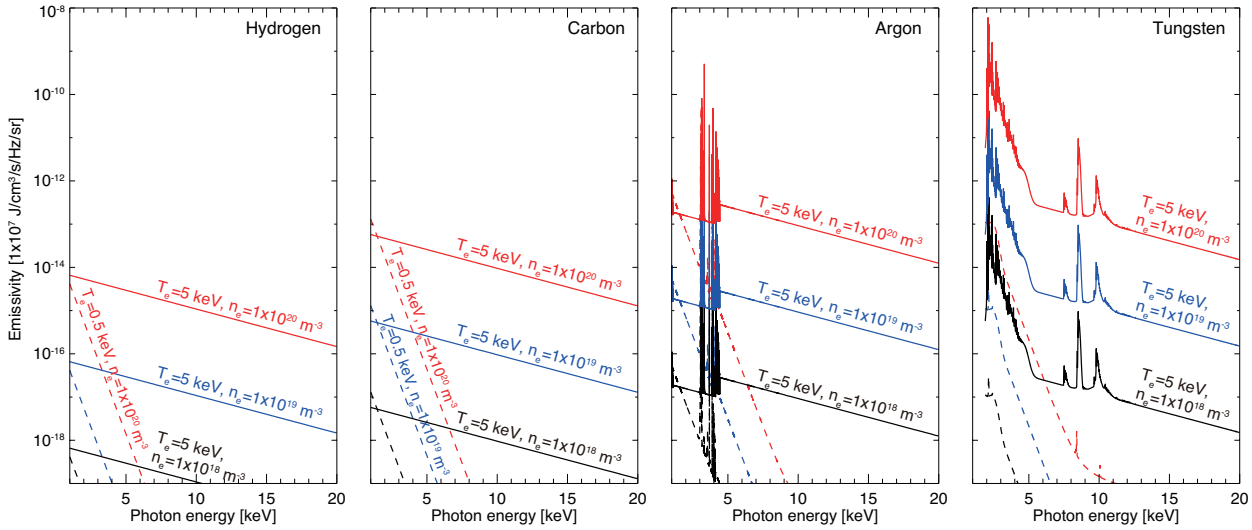

Figure 3.2: FLYCHK emissivity is scalable with electron density ($\propto n_{\rm e}^2$).

by red curve), and the electron density is assumed to be $n_{\rm e} = 10^{20}{\rm m}^{-3}$. Figures 3.3 (a)-(c) show only a continuum spectrum because ions are fully striped, while Figs. 3.3 (d)-(l) include bright line emissions as well as recombination edges.

Figures 3.4 indicates a relative ion charge state (Z) population obtained from FLYCHK for different electron temperatures. Figure 3.5 shows the average charge state $\langle Z \rangle$ as a function of electron temperature. With the increase in electron temperature $\langle Z \rangle$ increases. The blue dashed lines show the $\langle Z \rangle$ of the fully striped state, in which the plasma shows spectra without line emissions. Therefore, identification of line emissions with a energy resolved system provides the information on the electron temperature.

Emissivity ε from a plasma composed of species Z in the photon energy range E_0–E_1 with the electron temperature $T_{\rm e}$ and the electron density $n_{\rm e}$ is expressed as

$$\varepsilon_Z = \int_{E_0}^{E_1} \frac{F_Z(n_{\rm e}, T_{\rm e}, n_Z, E)}{E} \mathcal{T}_{\rm filter} \mathcal{T}_{\rm V} \mathcal{A}_{\rm detec} \mathcal{S}_{\rm detec}(E_{\rm C}, E) {\rm dE} \tag{3.1}$$

where F_Z is the spectrum calculated by FLYCHK for species Z, n_Z is its density, $\mathcal{T}_{\rm filter}(E)$ and $\mathcal{T}_{\rm V}(E)$ is the transmission of the filters to be used and that of the inter-component space which can be dealt with nearly 100 % for this calculation because the detector is installed in the vacuum, and $\mathcal{A}_{\rm detec}(E)$ is the x-ray absorption in the silicon detector lattice. Detector's electronic response curves $\mathcal{S}_{\rm detec}(E_{\rm C}, E)$ was calibrated using radio active isotopes and fitting function was obtained [108, 116], which can be approximated as

$$\mathcal{S}_{\rm detec}(E_{\rm C}, E) = 1 - \frac{1}{2} {\rm erfc} \left\{ -\frac{E - E_{\rm C}}{\sqrt{2} E_{\rm W}} \right\}, \tag{3.2}$$

where $E_{\rm W} (= 500$ eV) represents the width of the response. $E_{\rm C}$ is the adjustable energy threshold and the detector response S becomes 50 % at $E = E_{\rm C}$. Note that $E_{\rm C}$ is set by 6 bit DAC, and up to 64 energies can be set.

The resultant local deuterium concentration $n_{\rm D}/n_{\rm e}$ and plasma charge are calculated using quasineutrality,

$$\frac{n_{\rm D}}{n_{\rm e}} = 1 - \sum_i^n \frac{n_{{\rm Z}_i}}{n_{\rm e}} \cdot \langle Z\,(T_{\rm e}) \rangle_{{\rm F}_i}$$

$$Z_{\rm eff} = \frac{n_{\rm D}}{n_{\rm e}} + \sum_i^n \frac{n_{{\rm Z}_i}}{n_{\rm e}} \cdot \langle Z\,(T_{\rm e}) \rangle_{{\rm F}_i}^2,$$

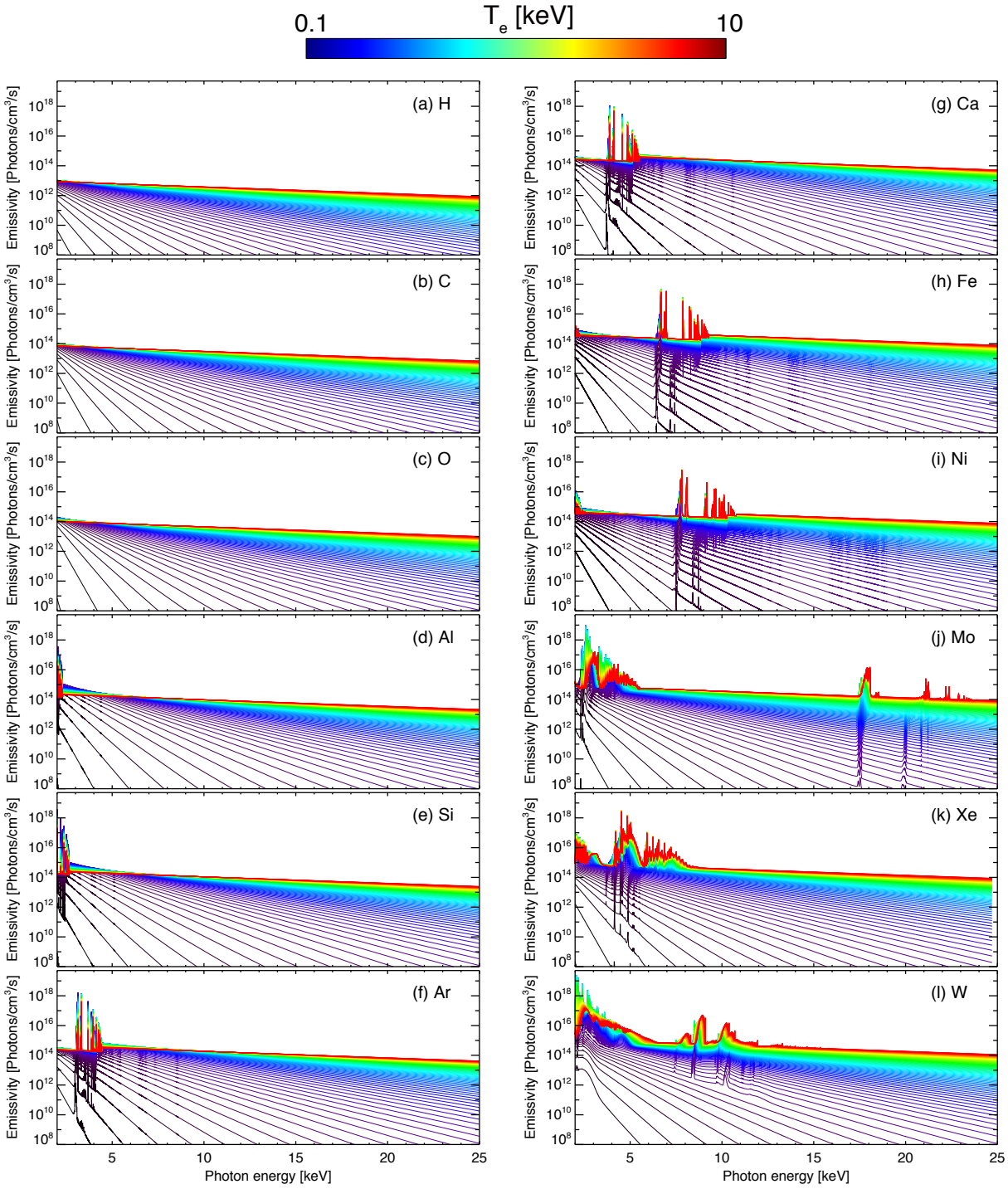

Figure 3.3: The spectra for twelve elements calculated by FLYCHK with the electron temperature from 0.1 keV through 10 keV and the electron density of 10^{20} m^{-3}. In SXR, mid-Z and high-Z materials consist of continuum and line emission, while low-Z materials (H, C and O) have only a continuum radiation.

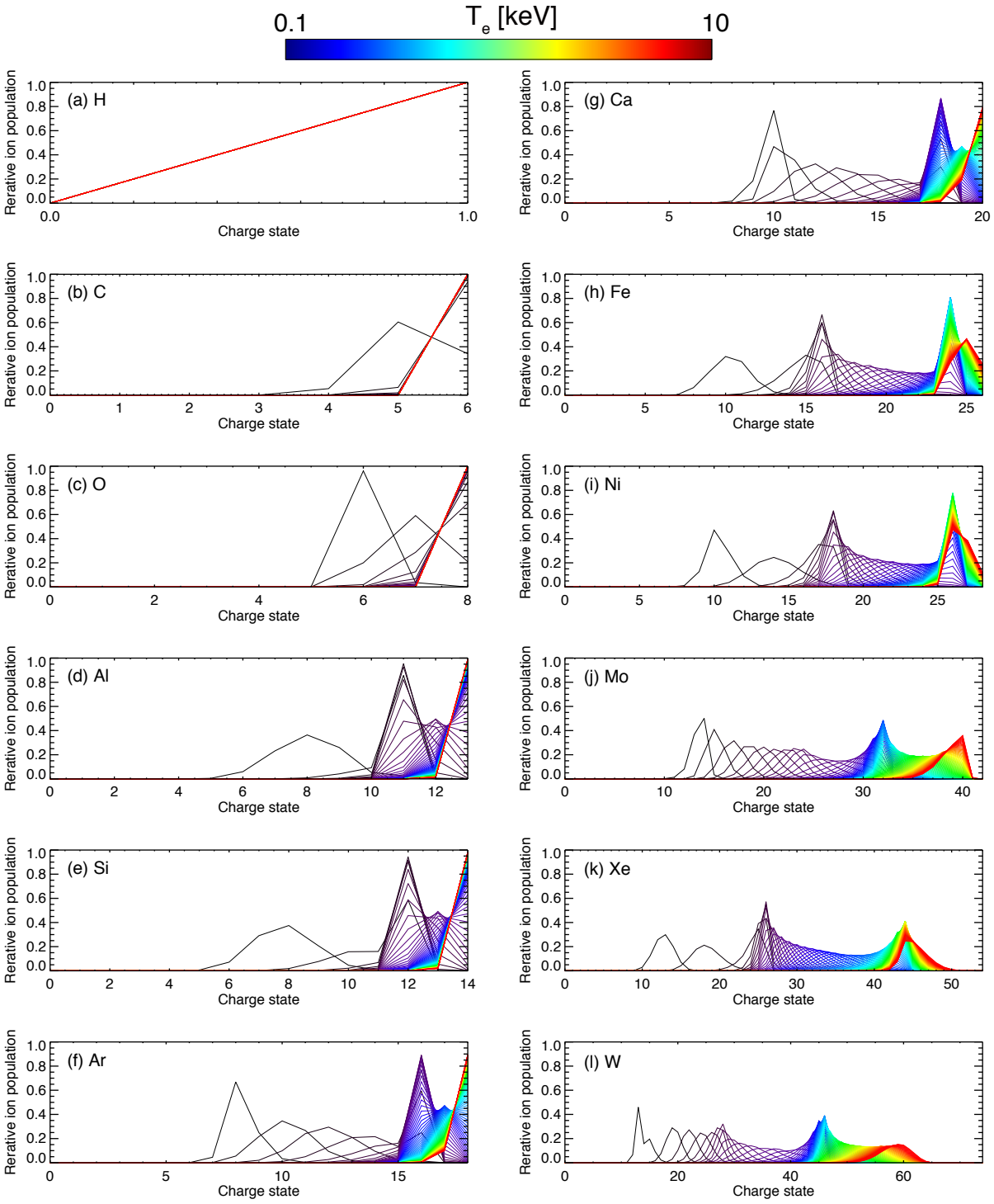

Figure 3.4: The ion population for twelve elements calculated by FLYCHK as a function of charge state.

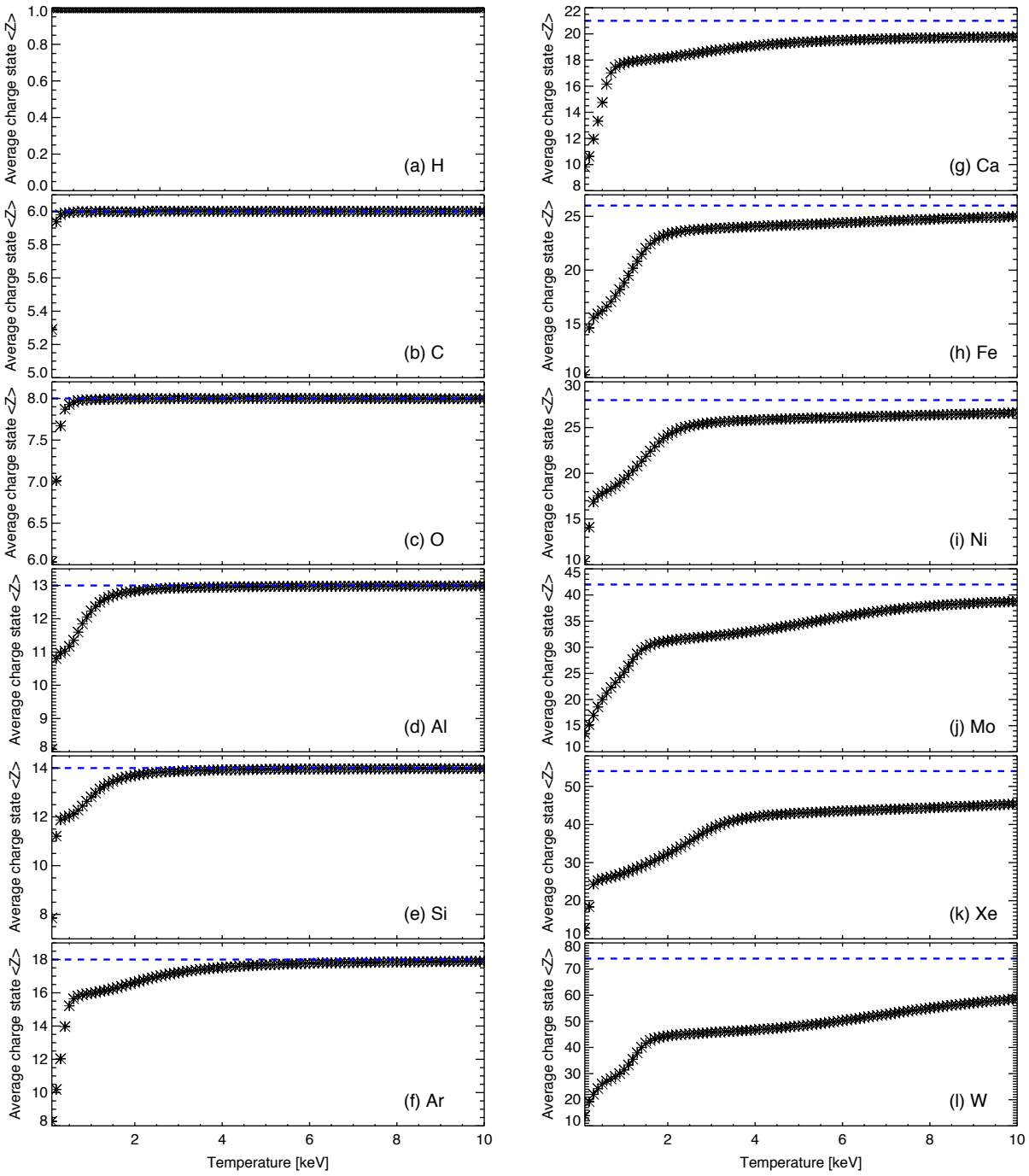

Figure 3.5: The average charge states for twelve elements calculated using relative ion population as a function of electron temperature. Charge number of the element is illustrated by blue dashed line. Low-Z elements (a-f) are easily ionized by the electron temperature of several keV, while the mid- and high-Z elements (g-l) are not fully stripped even in the 10 keV plasmas.

Table 3.1: Composition of commercial Be filter "IF-1".

Element	Actual	Percentage	Element	Actual	Percentage
Alminum	0.01	0.01	Lead	<0.0005	0.0001
Be	99.9	99.9	Magnesium	<0.006	0.0019
Be-O	0.01	0.01	Manganese	0.002	0.002
Calcium	<0.02	0.005	Molybdenum	<0.001	0.0005
Carbon	0.03	0.013	Nickel	0.01	0.01
Chromium	0.0025	0.002	Silicon	0.01	0.01
Cobalt	0.0004	0.0004	Silver	<0.0005	0.0001
Copper	0.002	0.002	Titanium	0.001	0.001
Iron	0.03	0.03	Zinc	<0.01	0.002
			Total:		100

where, $\langle Z\left(T_{\mathrm{e}}\right)\rangle_{\mathrm{F}_i}$ is the FLYCHK average charge state of the element Z as a function of the local electron temperature T_{e} (see Figs. 3.4 and 3.5). Here we assume deuterium D is the main ion components of the plasma.

The total emission at the one local point in space is the sum of the emission over all the ion species,

$$\varepsilon = \sum_{Z}^{n} \varepsilon_Z(R, Z).$$

3.1.2 X-ray interactions inside materials

X-ray attenuation, transmission and absorption in materials are calculated. When a collimated beam of photons with the energy E penetrates a thin slab with the thickness τ, a transmission $T(E)$ can be calculated as $T(E) = \exp\left(-\mu_{\mathrm{A}}\tau\right)$, here μ_{A} is mass attenuation coefficient obtained from NIST database [91]. An absorption is defined as $1 - T(E)$.

A transmission for complex material with the concentration C_j can be expressed as,

$$T_{\mathrm{complex}} = \Pi T_j^{C_j}\left(E, \tau_{\mathrm{complex}}\right) \tag{3.3}$$

here, T_j is a transmission for the single material of j and τ_{complex} is the thickness of the complex material.

Such calculations can be performed by x-ray oriented program (XOP) [117, 118]. XOP is a graphical user-interface (GUI) software and widely used for synchrotron facilities as well as x-ray research laboratories. It provides transmission and absorption not only in the single material but also in the complex materials such as Mylar foil and borosilicate glass window.

In the actual measurements, for example, Be filter which will be used for the vacuum wall between machine vacuum and rough vacuum of PILATUS detector is not a pure Be but has some compositions less than 1 %. Even though the compositions are small their effect cannot be neglected in the energy range of SXR. Table 3.1 shows the compositions of commercial Be filter "IF-1" [119], and Fig. 3.6 shows expanded view of the calculated transmission of IF-1 with the thickness of 100 μm.

Figure 3.7 shows the transmissions of a typical configuration of filters including a beryllium filter with the thickness of 50 μm (solid black curve) and that of a protective Mylar foil with a thicknesses of 12 μm (dashed orange curve) coated by 0.1 μm aluminum (solid green curve). Here, the Be filter is used to act as a vacuum-wall interface separating the machine and diagnostic vacuum ensuring the integrity of the main vacuum vessel. In order to avoid changes of the spectral response with respect to the incident angle we

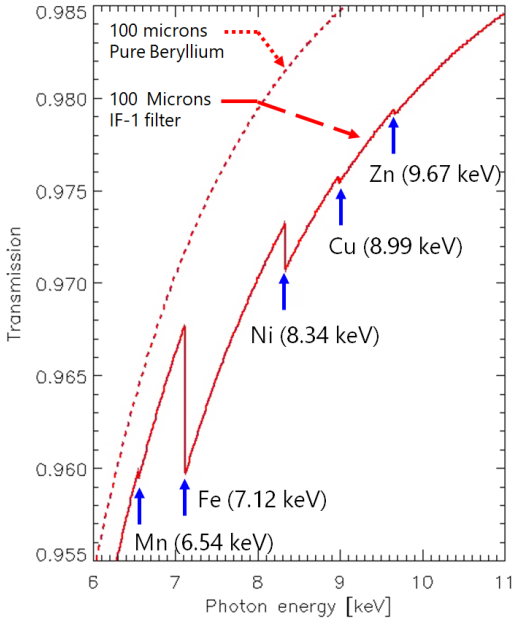

Figure 3.6: Expanded view of the transmission of 100 μm IF-1 filter.

propose the usage of a curved filter. The x-ray absorption on the PILATUS3 silicon lattice with a thickness of 450 μm is also illustrated by the blue dashed curve in Fig. 3.7. The total x-ray detection efficiency represented as,

$$\mathcal{T}_{\text{total}} = \mathcal{T}_{\text{filt}}\mathcal{A}_{\text{Si}} = \mathcal{T}_{\text{Al}}\mathcal{T}_{\text{Mylar}}\mathcal{T}_{\text{Be}}\mathcal{A}_{\text{Si}} \tag{3.4}$$

is illustrated by solid red curve.

3.1.3 One-dimensional calculation from emissivity to line-integrated brightness

The basic relation between the SXR brightness and the inverted emissivity can be expressed as

$$B_i = \sum_j L_{ij}\varepsilon_j \Longleftrightarrow \varepsilon_j = \sum_i L_{ji}^{-1} B_i \tag{3.5}$$

where, L_{ij} is a length matrix, B_i is the line-integrated brightness, ε_j is the local emissivity and subscript i and j denote a viewing chords of a pixel and an emission zone for the Abel reconstruction, respectively. Such matrix-based inversion technique [120] has already been applied to tangential imaging of charge exchange recombination spectroscopy and SXR imaging. The number of x-ray photons per-unit time (N_{ph}) impinging on each pixel is given by the product of the line-integrated brightness, the *etendue* and the integration time (Δt) as

$$N_{\text{ph}} = B_i \cdot \eta(\theta) \cdot \Delta t \tag{3.6}$$

Assuming that the thickness of the Be filter is smaller than the thickness of the pin-hole aperture, and that the latter is smaller than its 2D dimensions (see Fig. 3.8), the *etendue* can be approximated as

$$\eta\,(\theta) \approx \frac{A_{\text{pin}} \cdot A_{\text{px}}}{4\pi d^2} \cos^4\theta.$$

The *etendue* depends on the pinhole area A_{pin}, the pixel area of the PILATUS detector $A_{\text{px}} = (172\ \mu\text{m})^2$, the distance between the pinhole and pixel surface d and the incident angle θ.

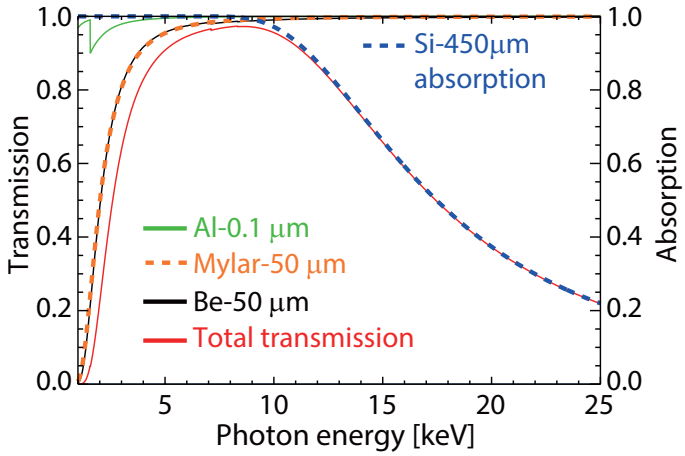

Figure 3.7: Transmission of filters: Mylar foil (orange dashed curve) with Al coating (green solid curve) and Be-filter (black solid curve), and absorption of the silicon detector (blue dashed curve) are calculated by XOP. Red solid curve indicates the total detection efficiency of the system.

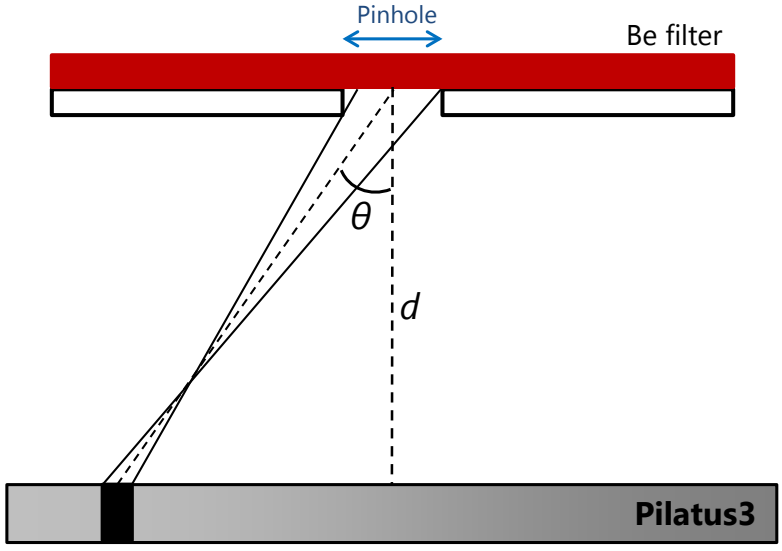

Figure 3.8: Schematic drawing of PILATUS detector, pinhole and Be filter.

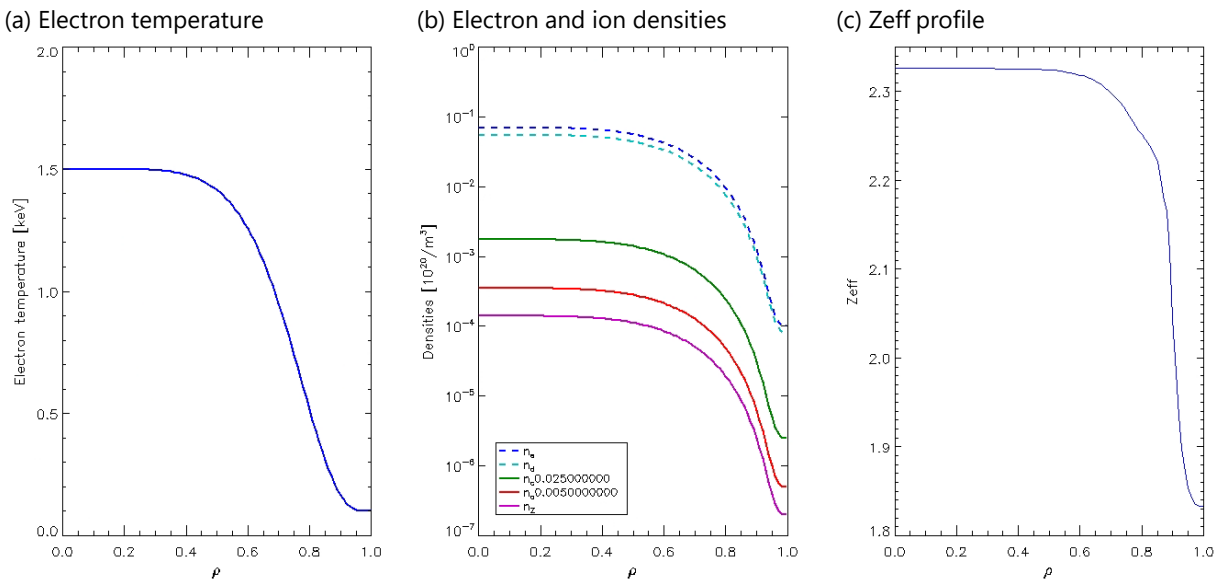

Figure 3.9: Input profiles for (a) electron temperature, (b) electron density and impurity densities and (c) Z_{eff} profile.

3.2 Benchmark and experimental result at MST

Using the computational tool described in the previous section, photon counts impinging on the detector is calculated for ME-SXR diagnostics on the Madison Symmetric Torus (MST) [107]. MST is a reversed field pinch magnetic confinement device at University of Wisconsin-Madison [121]. Device parameters are as follows; major radius: $R \sim 1.5$ m, minor radius: $a \sim 0.52$ m, typical plasma current: $200 < I_{\mathrm{p}} < 500$ kA, electron temperature and density: $T_{\mathrm{e}} \sim 2$ keV and $n_{\mathrm{e}} \sim 1 \times 10^{19}$ m^{-3} and discharge duration is < 100 ms. In MST, pulsed poloidal current drive (PPCD) plasmas in which tearing modes are surppressed and the confinement is improved [122–124] and quasi-single helicity (QSH) plasmas which have a non-reversed mode are studied [125].

3.2.1 Profiles and geometry

The electron temperature and density profiles in MST, which are the input information for the computational tool, are expressed by a parameterized function based on measurement as,

$$f(R) = f_0 \left(1 - \left(\frac{R}{a}\right)^{\alpha}\right)^{\beta} + f_{\mathrm{offset}}.$$

Figure 3.9 shows profiles in MST, in which f_0 and f_{offset} are $f_0 = T_{\mathrm{e}_0} = 2.0$ keV and $f_{\mathrm{offset}} = T_{\mathrm{e_offset}} = 0.1$ keV for electron temperature profile, $f_0 = n_{\mathrm{e}_0} = 1.2 \times 10^{19}$ m^{-3} and $f_{\mathrm{offset}} = n_{\mathrm{e_offset}} = 1.2 \times 10^{15}$ m^{-3} for electron density profile respectively. α and β defining for both temperature and density profiles are $\alpha_T = 6$ and $\beta_T = 4$, and $\alpha_n = 4.2$ and $\beta_n = 4$, respectively. These parameters are obtained from the analysis of several measurements in MST, and we can rely on them for the present benchmark. Impurity concentrations are assumed to be homogeneous across the minor radius, and their profiles have a constant fraction of the electron density profile (Fig. 3.9 (b)). The concentrations are set to be 2.5 % for carbon, 0.5 % for oxygen and 0.2 % for aluminum [126].

Pixel responses of PILATUS3, filter transmissions and an absorption of detector are calculated and illustrated in Fig. 3.10. The pixel responses (Fig. 3.10(a)) on each pixels are defined by Eq. 3.2 with E_{C}

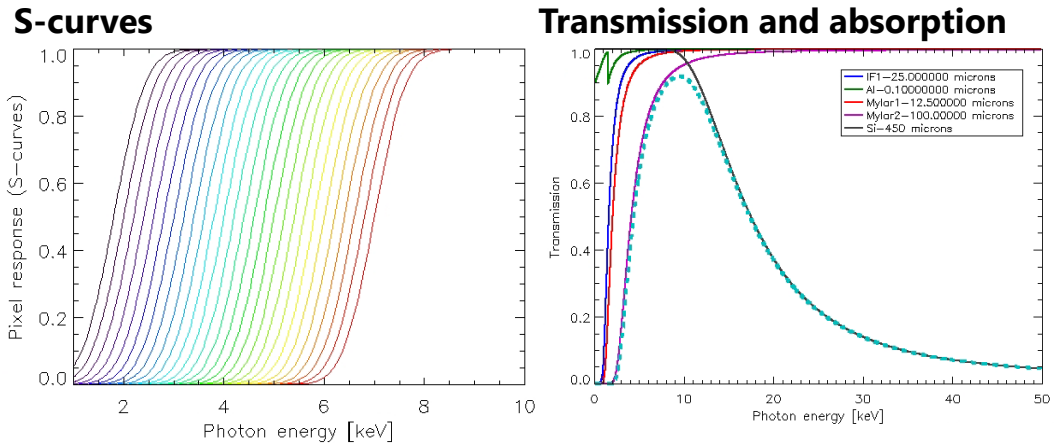

Figure 3.10: Transmission of filters (b). Two Mylar foils (purple and red solid curve) with Al coating (green solid curve) and Be-filter (blue solid curve) and absorption of the silicon detector (black solid curve) are calculated. Cyan dashed curve indicates the total sensitivity of filters and detector.

from 1.8 to 7 keV with 0.2 keV steps, and the filters (Fig. 3.10(b)) are a beryllium filter with the thickness of 25 μm (solid blue curve), a protective Mylar foils with the thicknesses of 100 μm (solid purple curve) and 12 μm (solid red curve) coated by 0.1 μm aluminum (solid green curve), respectively. The absorption of the silicon detector is denoted by black solid curve. Cyan dashed curve indicates the total efficiency of the system calculated as $\mathcal{T}_{\rm total}(E) = T_{\rm Be}(E)T_{\rm Mylar:12.5\mu m}(E)T_{\rm Mylar:100\mu m}(E)T_{\rm Al}(E)A_{\rm S}(E)$.

We have designed the geometries for the ME-SXR measurements on MST and fabricated and installed. The geometrical parameters are as follows: the pinhole area $A_{\rm pin} = 1.0$ mm $\times$ 4.0 mm, the pixel area $A_{\rm px} = (172\ \mu{\rm m})^2$, the distance between the pinhole and pixel surface is $d = 30.56$ mm. The incident angles satisfy $-55\ ^\circ < \theta < 55\ ^\circ$ with a central ($\theta = 0$) *etendue* of $\approx 1.0 \times 10^{-7}$ cm^2 calculated from Eq. (3.7), and these values are used for the calculation of this benchmark.

3.2.2 Calculation and initial experimental result

The third generation of ME-SXR detector, "PILATUS3" has been installed on MST, and photon counts estimation was carried out to compare the experimental data and evaluating the calculated result [109].

Figure 3.12 shows photon counts as functions of pixel number in radial direction and the energy threshold $E_{\rm C}$ from 1.8 keV (red curve) to 7.0 keV (black curve). The experimental result is shown in Fig. 3.13. The top figure indicates two dimensional pixel map and the bottom plot shows toroidally integrated brightness as a function of sight-line. The maximum photon count expected numerically is $\approx$110 photons/pixel/ms for $E_{\rm C} = 2.0$ keV, which agrees well with the experimental result $N_{\rm max} \approx 80$ photons/pixel/ms within a factor of 2.

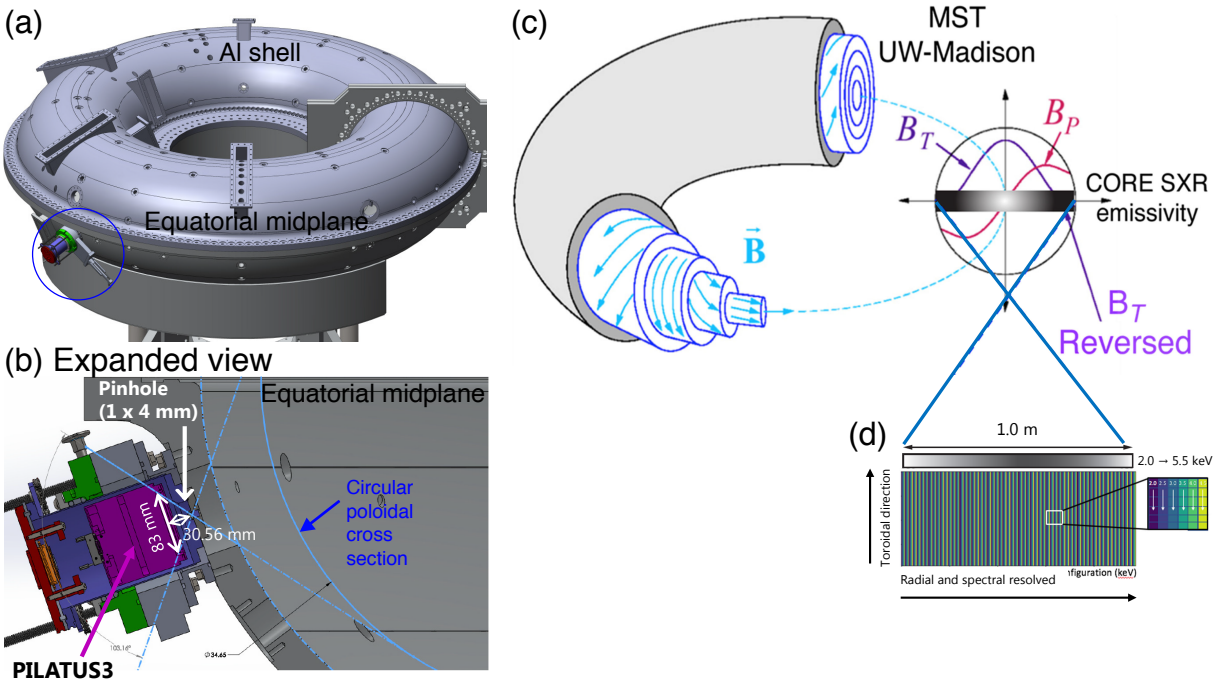

Figure 3.11: Installation geometry and pixel map. (a) MST outer shell, (b) expanded view of PILATUS detector and (c) MST plasma with sightline. (d) PILATUS3 pixel map using radial one dimensional measurement.

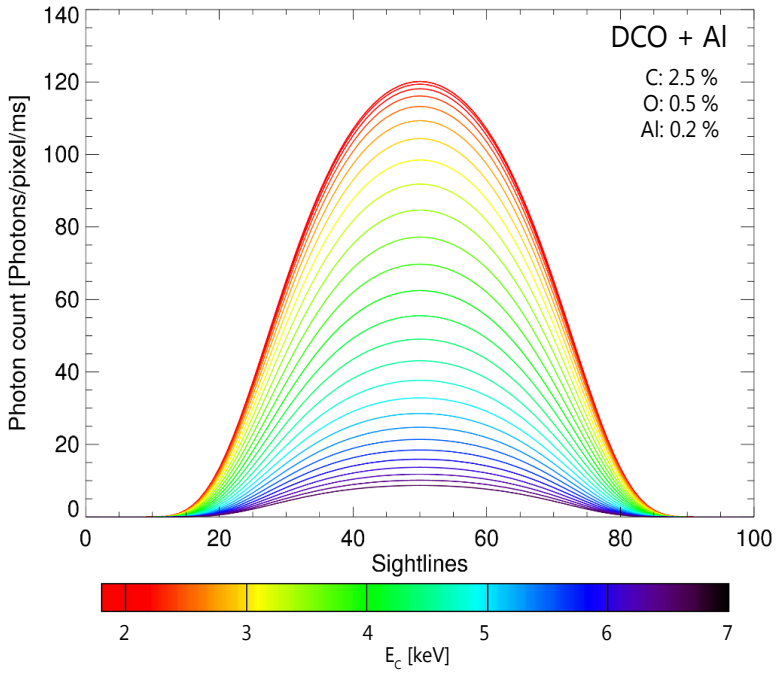

Figure 3.12: The calculation results with the energy threshold E_C from 1.8 keV (red curve) to 7.0 keV (black curve). The sightline number 0 indicates the sight line for the edge and the chord number 50 indicates the core.

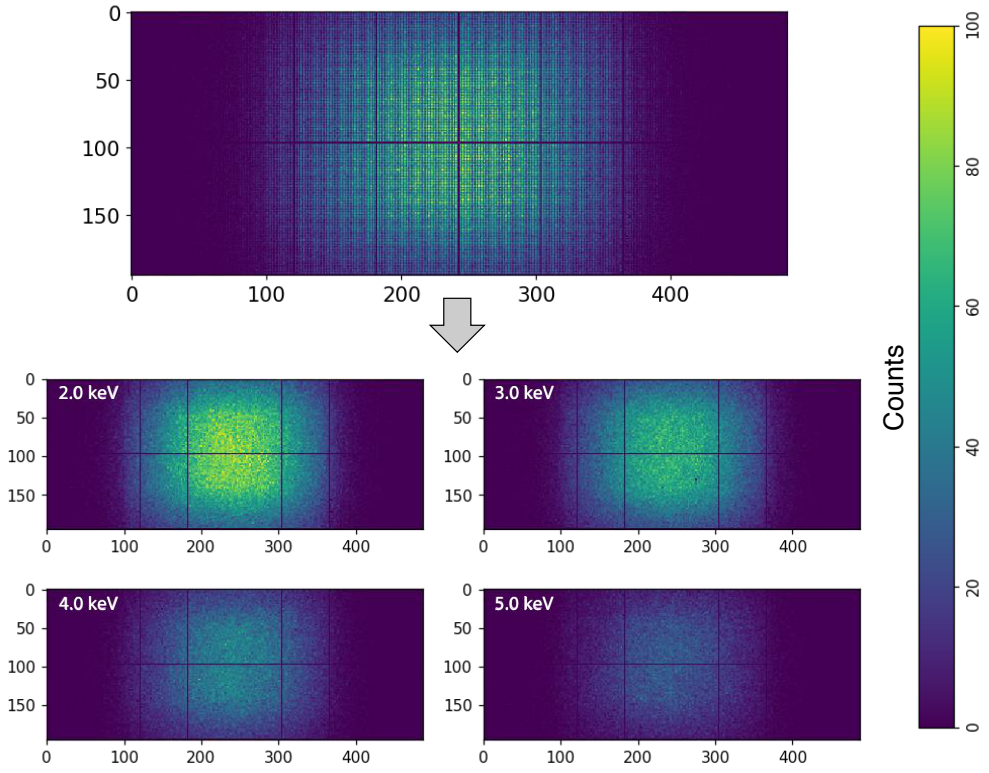

Figure 3.13: Experimental result obtained in PPCD discharge at $t = 20$ ms–21 ms. The top plot shows the original image and the bottom plots show the split images with different E_{C} [110].

3.3 Simulations for several devices

3.3.1 DIII-D like plasmas

DIII-D is a mid-size tokamak located at the General Atomics in San diego, USA and it started operation in 1986 [127]. On DIII-D we are now proposing a research plan, in which an ME-SXR system is installed to measure the whole plasma [111]. The main objective of the research is to study the impurity transport by active injection of various impurities. DIII-D is one of the devices suitable for this study because of their various means for injecting impurities and controlling plasmas [128]. Impurities can be introduced using gas puffs, pellet injection systems, laser blow off systems and impurity granule injector [129]. In addition carbon based machine remains ideal reference DCO profile for studying medium- to high- Z impurity transport.

In this section, typical H-mode and L-mode plasmas in DIII-D is assumed, and various concentration of various elements are assumed. In addition, photon noise is calculated to show the tailoring of spatial and temporal resolution.

Profiles and geometry

The electron temperature and density profiles used in the calculation are shown in Fig. 3.15 (a). For a high-confinement (H-mode) case we have used realistic profiles measured by Thomson scattering measurement at DIII-D [130] in the core region, while the edge profile is approximated by a tangent hyperbolic function using the measured data as a function of a cylindrical normalized radius $\rho = R/a$, where the minor radius is $a = 0.57$ m. For an example of the low-confinement (L-mode) case, we have used a parameterized function defined by,

$$f(r) = f_0 \left(1 - (\rho)^{\alpha}\right)^{\beta} + f_{\text{offset}},$$

to express the temperature and density profiles. The central value $f_0 + f_{\text{offset}}$ is adjusted to be 2.8 keV for electron temperature and 0.8×10^{20} m^{-3} for electron density, respectively. These are the same as those in the H-mode scenario. The values of α and β are $\alpha_T = 8$ and $\beta_T = 5$, and $\alpha_n = 8$ and $\beta_n = 2$, for electron temperature and density respectively.

In this work, we have assumed a reference "DCO" plasma using deuterium (D) plus constant carbon (C) and oxygen (O) concentrations of 2.5 % and 0.25 % which result in a core $Z_{\text{eff}} \approx 1.9$. We also calculated the cases with additional (heavier) impurities, in which the additional impurity concentration is assumed to be homogeneous across the minor radius, and is set to be either 0.052 % for argon or 0.022 % for nickel or 0.015 % for molybdenum. The concentrations were determined so that the Z_{eff} at the core increased only by the trace limit as $\Delta Z_{\text{eff}} \sim 0.1$.

In order to simulate an impurity transport experiment we also considered several localized impurity concentration cases, in which the density profile of a selected impurity is localized only at the edge ($\rho = 0.9$) or at the mid-radius ($\rho = 0.5$) (Fig. 3.15 (b)). This impurity perturbations are approximated by a Gaussian function as

$$\delta n_{\text{Z}} = \Delta n_{\text{Z}} \exp\left\{ - \left(\frac{\rho - \delta_\rho}{\sqrt{2}\Delta\rho} \right)^2 \right\},$$

here the width parameter of is $\Delta\rho = 0.01$ for $\delta_\rho = 0.9$ (edge) and $\Delta\rho = 0.03$ for $\delta_\rho = 0.5$ (mid-radius), respectively. Peak concentration Δn_{Z} and maximum ΔZ_{eff} for the extrinsic impurities are listed in Table 3.2.

Impurity profile considering the "peaking factor" was also taking into account for transport studying. Impurity transport is a very complicated function of collisionality and plasma profiles, but phenomenologically, a peaking factor expressed under the steady state condition $\partial n_{\text{Z}}(r,t)/\partial t \sim 0$ is written

Table 3.2: Parameters of Gaussian impurity profile

$\delta_\rho = 0.9$ (edge)			$\delta_\rho = 0.5$ (mid-radius)		
Impurities	Concentrations n_Z/n_e	ΔZ_{eff}	Impurities	Concentrations n_Z/n_e	ΔZ_{eff}
Ar	0.117 %	~0.3	Ar	0.037 %	~0.1
Ca	0.098 %	~0.3	Ca	0.031 %	~0.1
Ni	0.083 %	~0.3	Ni	0.016 %	~0.1
Mo	0.052 %	~0.3	Mo	0.010 %	~0.1

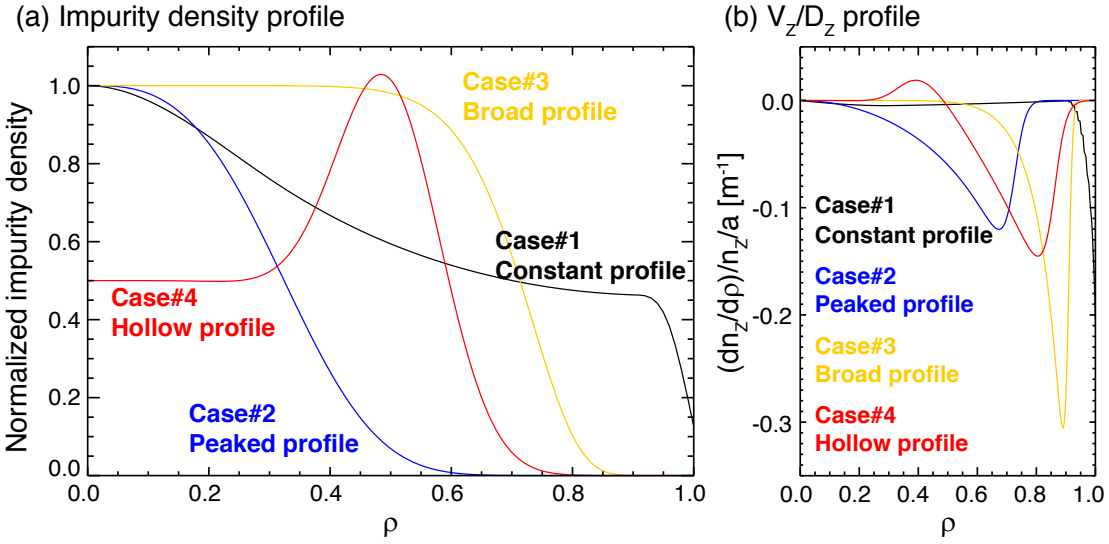

Figure 3.14: (a) Impurity density profile as a function of ρ and (b) V_Z/D_Z ratio profile derived from density profile.

as [131, 132]

$$\Gamma_Z(r,t) = -D_Z(r,t)\frac{\partial n_Z(r,t)}{\partial r} + n_Z(r,t)V_Z(r,t) = 0$$

$$\therefore \ \frac{V_Z}{D_Z} = \frac{1}{n_Z}\frac{dn_Z}{d\rho}\frac{1}{a}.$$

The ratio V_Z/D_Z can be determined from the spatial evolution of an impurity density [133]. Figure 3.14 depicts impurity density profiles and V_Z/D_Z ratio profiles for the four cases we considered.

A schematic top-down view of the DIII-D tokamak and that of the planned tangential view and tangency radii (R_{tan}) are shown in Fig. 3.16. The blue lines indicate the original configuration to image the DIII-D core, while the red lines show the high-resolution configuration for imaging the low-field-side (LFS) edge.

Local emissivities

The local emissivities for both H-mode and L-mode DCO plasmas as a function of major radius R and detector cutoff energies are shown in Fig. 3.17. Comparing H-mode and L-mode emissivity profiles, strong emission at the edge due to the pedestal structure located around $\rho = 0.9$ is obtained. The contribution on the overall emission by small change in $\Delta Z_{eff} \sim 0.15$ using an extrinsic impurity can be easily observed in

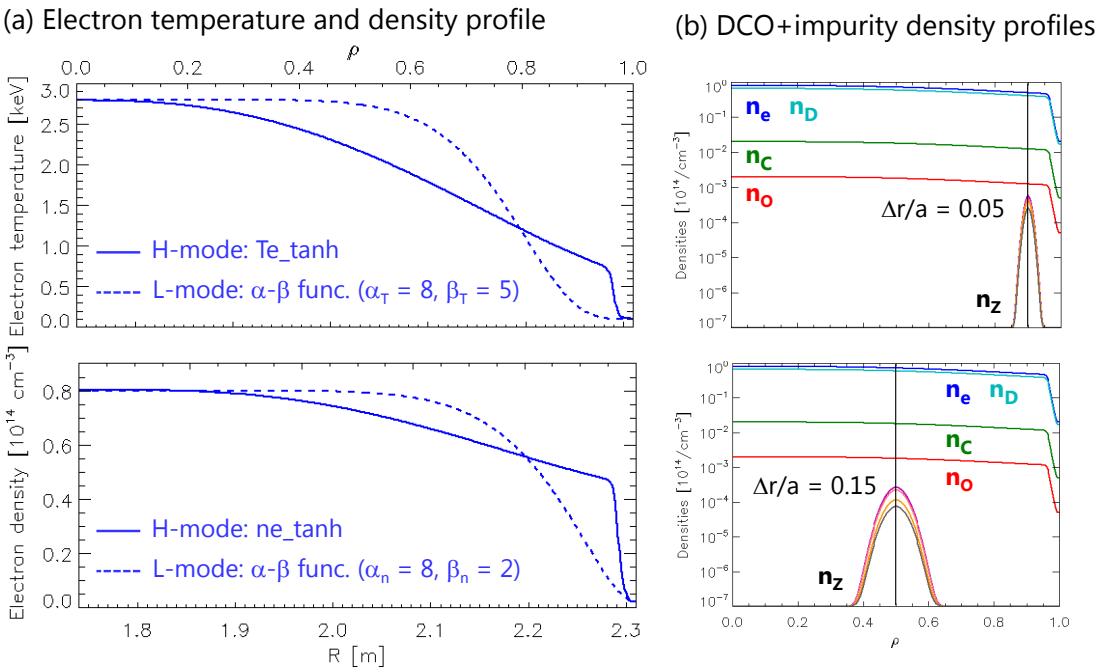

Figure 3.15: Input profiles for DIII-D H-mode and L-mode plasmas.

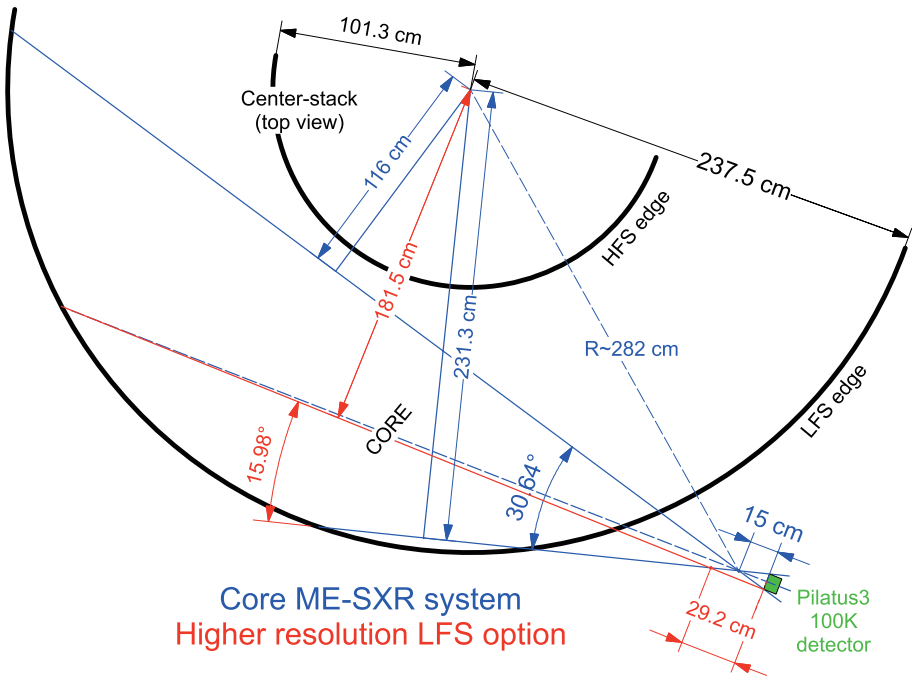

Figure 3.16: A schematic top-view of the DIII-D tokamak and measurable ranges of ME-SXR system.

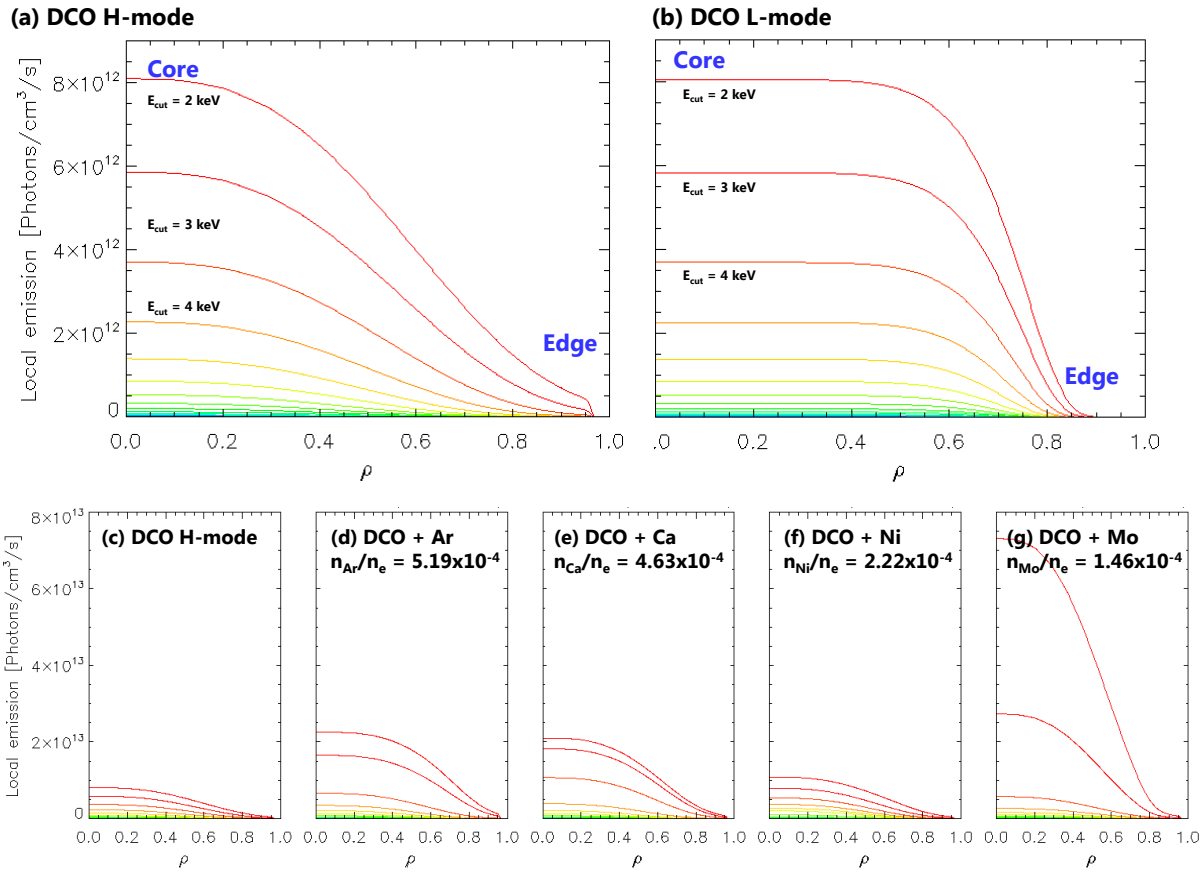

Figure 3.17: Calculated emissivities for (a) DIII-D H-mode DCO plasma, (b) L-mode DCO plasma, (c-g) DCO plus impurities Ar, Ca, Ni and Mo, respectively.

Fig. 3.17(c)–(g). The contrast between the reference DCO case (Fig. 3.17 (a)) and the impurity-seeded cases (Figs. 3.17 (c)–(g)) is quite large and the difference increase further when comparing with cleaner reference plasmas with $Z_{\rm eff} \sim 1$. Note that the emissivity from Ni measured using lower cutoff energy $E_{\rm C}$ <7 keV is small because its line emission exists only around the photon energies from 7 to 11 keV while the line spectra from Ar and Mo exist below 5 keV. This results show that the Ar and Mo can be useful as seed impurity for intensity enhancement. In addition, we expect to find experimentally a strong contribution from the Ar recombination edges as a result of the recombination (steps) around 4 and 4.5 keV. This enhancement - not considered in this simulations - corresponds to the radiative capture of free electrons by hydrogen-like Ar into the ground state of helium-like Ar mostly induced by outward particle transport as observed in PLT [135].

The emissivity profiles of H-mode plasmas with the impurity localized to the mid-radius or the edge are simulated. The enhanced emission from Ar and Ca gas puffs or Ni and Mo injection at the LFS-edge is demonstrated in Figs. 3.18 (b)-(e), and it was found that the argon emissivity is stronger than that from other elements, calcium, nickel and molybdenum due to the low electron temperature. This simulation also shows that the SXR emissivity at the top of the H-mode pedestals can be greatly enhanced with the use of an Ar puff at the edge. In contrast, the molybdenum emissivity at mid-radius is a factor of three stronger than that of argon due to the change of the electron temperature (Figs. 3.18 (f)-(j)).

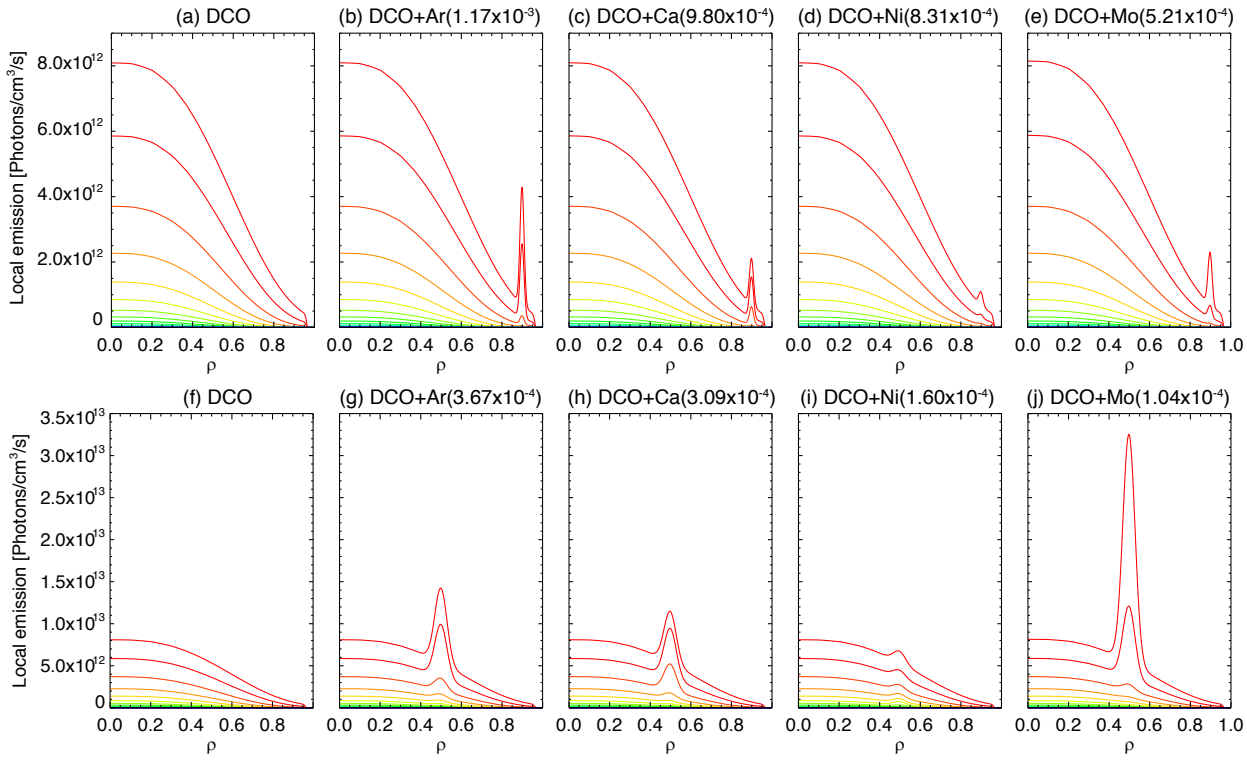

Figure 3.18: Calculated emissivities for (a), (f) DIII-D H-mode DCO plasma, (b-e) impurity injected to the edge, (f-i) impurity injected to the mid-radius.

Photon counts on the detector

Photon counts on the PILATUS3 detector was calculated using Eqs. (3.5), (3.6) for H-mode DCO plasma and Ar and Mo injected cases. Since photon counts are one of the main noise sources, it is important to predict them for given plasma parameter and geometrical configuration. Through the prediction, we can optimize the spatial and energy (and temporal) resolution of the ME-SXR measurement system.

A PILATUS3 has 195 pixels in the vertical direction and 487 pixels in the horizontal direction. For a 1–D measurement, pixels in the horizontal direction can be used for spatial profile and pixels in the vertical direction can be used for energy spectrum. However, when we consider the noise and required spatial and energy (and temporal) resolution, we may bin several pixels in the horizontal and vertical directions. Such binning and energy resolution are practical and available due to the huge energy resolved pixels of a PILATUS3, and the computational tool we developed is quite useful to optimize the performance of the ME-SXR system.

Figure 3.19 shows the two different arrangements:

(a) Moderate spatial resolution: 487 pixels in the horizontal direction are used for spatial and energy resolutions, and the pixels of an entire row in the vertical direction are binned to obtain sufficient number of photons for good signal-to-noise ratio.

(b) High spatial resolution: 487 pixels in the horizontal direction are used only for spatial resolution, and 195 pixels are used to set multi-filters.

In arrangement (a), binning and energy setup are adjusted to achieve moderate spatial and energy resolutions, which are necessary to study impurity transport in DIII-D. In the cases of MST, 60 sight-lines with 8 different energy filters, and each sight-line with a certain energy filter has 195 pixels for the integration. In contrast, the arrangement (b) can use up to 487 sight-lines and 19 different energy filters with 10 binned pixels,

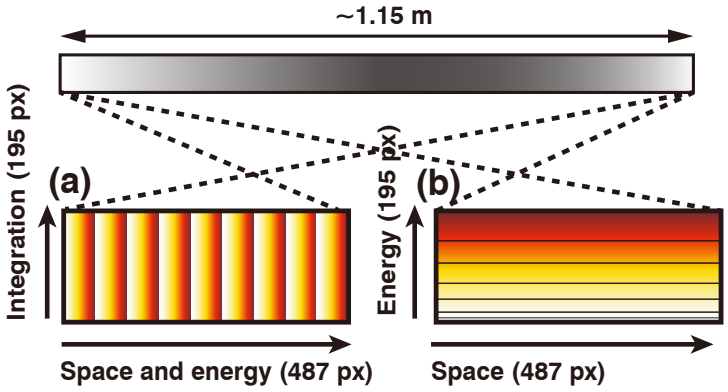

Figure 3.19: Two examples of pixel arrangement for the 1-D measurement. Top gray box shows a horizontal slice of a DIII-D plasma with relatively short height. Bottom colored boxes show two cases of 2-D detector area (487×195 pixels) with different energy threshold $E_{\rm cut}$ (indicated by color) settings. (a) moderate spatial and high energy resolution case, and (b) high spatial and low energy resolution case are shown.

which allow us to measure a profile with significantly high spatial resolution as long as sufficient photons are obtained.

In this calculations, we assume 230 sight-lines with 0.5 cm spacing in the core covering a tangency radii from $R_{\rm tan} = 1.16$ in the HFS to 2.31 m in the LFS as shown in Fig. 3.16, and we also assume 19 energy thresholds from $E_{\rm C} = 2$ keV to 20 keV with 1 keV for spectral resolution. Here we adopt an arrangement similar to (b), where 487 pixels in the horizontal direction are binned to 230 sight-lines and 195 pixels in the vertical direction are used for 19 different cut-off energy filters. Thus, two rows in the horizontal direction are used for the same viewing chord, and 10 rows in the vertical direction has the same cut-off energy filter.

The count of x-ray photons as a function of chord number and cut-off energy for the DCO case and that with injections at the edge and mid-radius are shown in Figs. 3.20. The maximum count of x-rays computed from all cases is less than 8×10^2 counts/pixel/ms and do not exceed PILATUS3's maximum count rate 10^4 counts/pixel/ms, which indicates there is enough throughput to operate at even higher temperatures and densities as well as higher impurity concentrations. In the case where the photon count is larger than the maximum count rate, it is necessary to decrease the pinhole vertical dimension so as not to affect the radial spatial resolution.

For the cases in which Ar and Mo are injected at the edge, the signals are enhanced over the DCO hydrogenic Bremsstralung (compare Figs. 3.20-(a) with (b) and (c)) but are not comparable to that at the core (compare Figs. 3.20-(d) with (e) and (f)). The Ar and Mo emission at mid radius shown in Figs. 3.20 (b) and (f) will be easily reconstructed from the line integrated brightness, because the reconstructed local emissivity is proportional to the derivative of the line integrated brightness with respect to the tangency radius.

Resolution and discussion

The signal to noise ratio (SNR) depends on the total photon counts of each binned pixels. In this configuration, we can bin 2 pixels in the horizontal directionand 10 pixels in the vertical direction leading to 19 energy thresholds (Fig. 3.19). From the calculated photon numbers we can estimate SNRs assuming Poisson processes.

In order to evaluate spacial and spectral resolution, a photon emissivity profile was reconstructed using a computed photon count profile and the reconstructed profile was compared with original emissivity profile. Here we show two cases – (i) good SNR with low spacial resolution and (ii) high spacial resolution but low

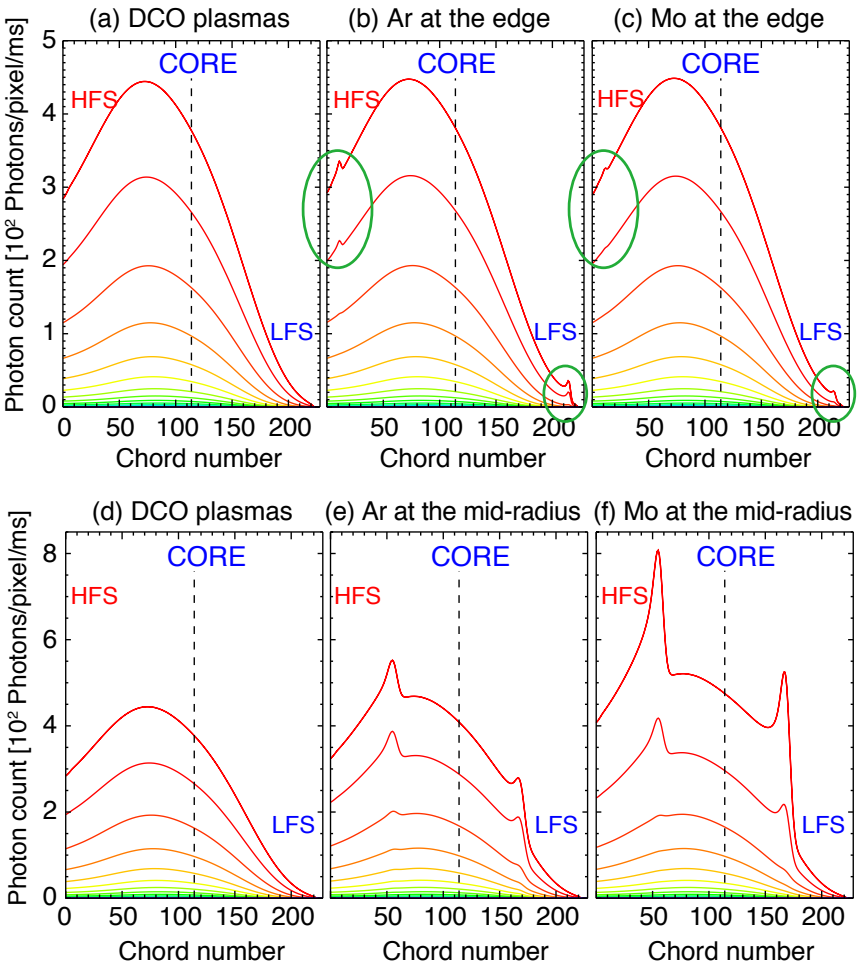

Figure 3.20: Photon counts as a function of chord number for (a), (d) DCO case and with (b) Ar and (c) Mo injections at the mid-radius, and (e) Ar and (f) Mo injections at the edge.

SNR – illustrated in Fig. 3.21, using photon count profile of the Ar injection at the edge (see Fig. 3.18 (b) and Fig. 3.20 (b)) with adding a Poisson noise calculated as $\delta = \sqrt{\mathcal{N}_{\rm total}}$, where $\mathcal{N}_{\rm total}$ is a photon count on one sight-line. In case (i), total 100 sight-lines with 1.15 cm spacing is assumed and therefore the photon count $\mathcal{N}$ is obtained by computed photon count times 100 (binned 5 pixels in vertical and 20 pixels in horizontal). Figure 3.21 (a) shows the reconstructed emissivity profile and its expanded view of the LFS is shown in Fig. 3.21 (c) by color curves. The black curves depict the original emissivity profiles (same as Fig. 3.18 (b)). In this configuration, we can clearly distinguish each signals obtained by different cutoff energy setting and can measure the contribution by Ar injection. On the other hand, in case (ii), we assume total 497 sight lines with ~ 0.2 cm spacial resolution, and only 20 pixels in horizontal direction is binned. In Fig. 3.18 (c) and (d), pedestal structure is clearly reproduced, but evaluation of argon's emission contribution is difficult due to low SNR especially for HFS. However, the identification of the shoulder position of the H-mode pedestal becomes possible by:

1. Using the reconstructed profile of the lower cut-off energies below 2 keV
2. Increasing the exposure time by double or more
3. Removal of the Mylar protective cover which will result in the signal increase by 50%
4. Adopting a high-resolution LFS optional design with a secondary pinhole at $d \sim 29$ cm as shown in Fig. 3.16.

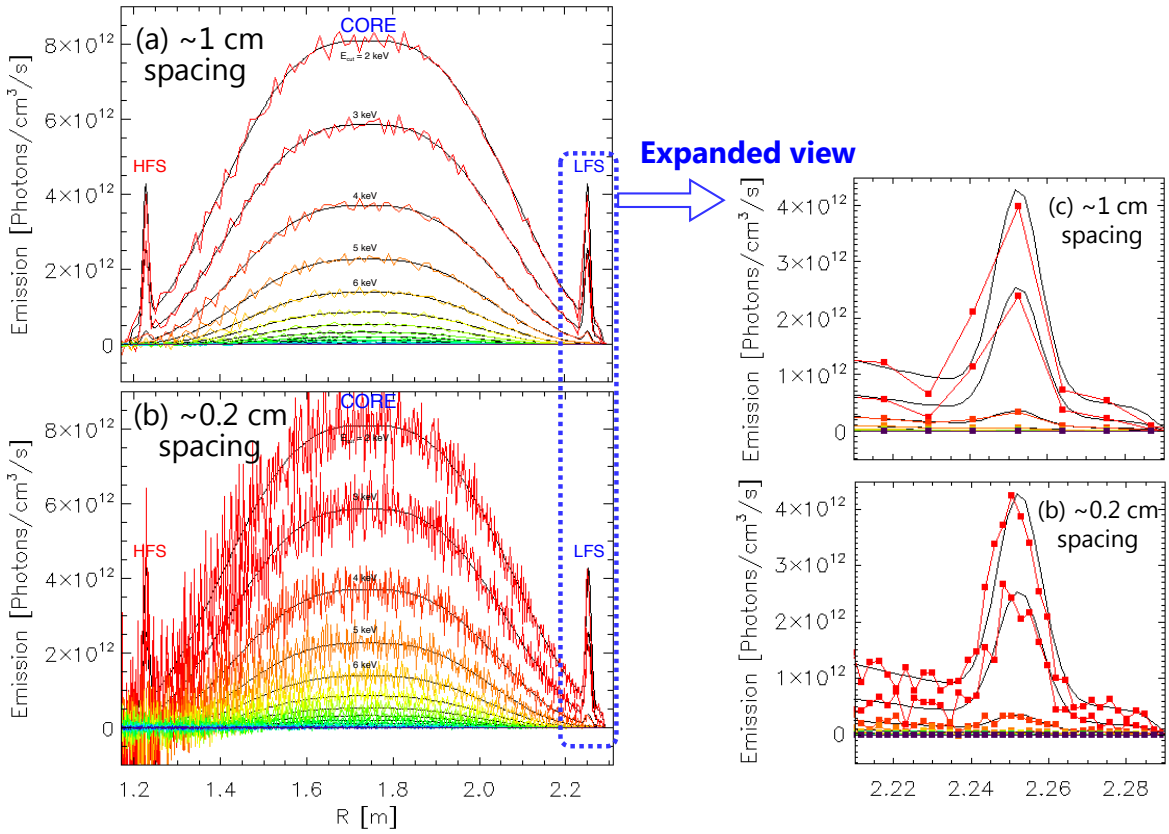

Figure 3.21: Reconstructed emissivity profile (color curves) and original profile (black curve) for (a) low spacial resolution case and (b) high spacial resolution case. Expanded view at the LFS is shown in (b) and (d).

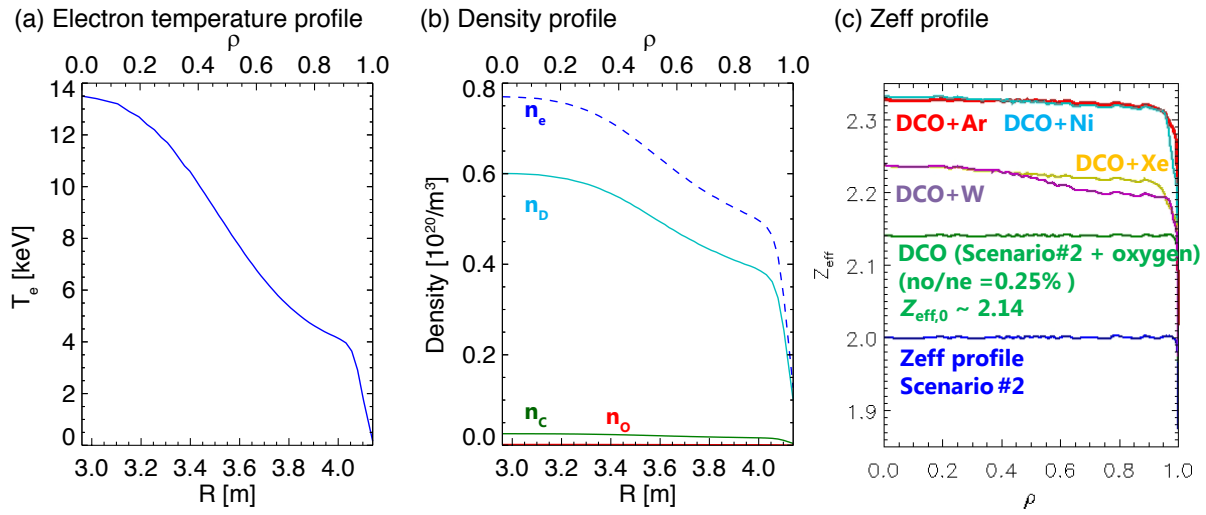

Figure 3.22: Input profile of JT-60SA scenario no.2 [136]

3.3.2 JT-60SA plasmas

JT-60SA is a large size tokamak and currently under construction in Naka, Japan, as a part of international project, which will start operation in 2020, with first deuterium experiments in 2023. The JT-60SA device has been designed to achieve a break-even-condition class high temperature and density with a duration of 100 s.

We applied our computational tool to JT-60SA high temperature plasmas (operational scenario no.2 [136]) and performed feasibility study for future measurements. The target profiles used for evaluating the detector response are shown in Fig. 3.22. Firstly, deuterium plasma with a constant carbon and oxygen concentrations of 2.5 % and 0.25 % which result in a core $Z_{\mathrm{eff},0} \approx 2.14$ was considered (green curve in Fig. 3.22 (c)). In order to evaluate signal enhancement due to the impurities, we considered four impurities, argon, nickel, xenon and tungsten with a constant concentration and calculated the local emissivity profiles.

Results of calculated emissivity profile is shown in Fig. 3.23. As a result of the calculation, it was found that in the case where the presence of Ar and Ni was assumed the line emission intensity was increased by a factor of 1.5-2 at the pixels having the energy thresholds between 2 and 3 keV and 2 and 7 keV, respectively. In the case where Xe or W was induced, it was found that strong emission was expected at $\rho \sim 0.4$ for the Xe-case (Fig. 3.23 (c)), and at $\rho \sim 0.6$ for the W-case (Fig. 3.23 (d)).

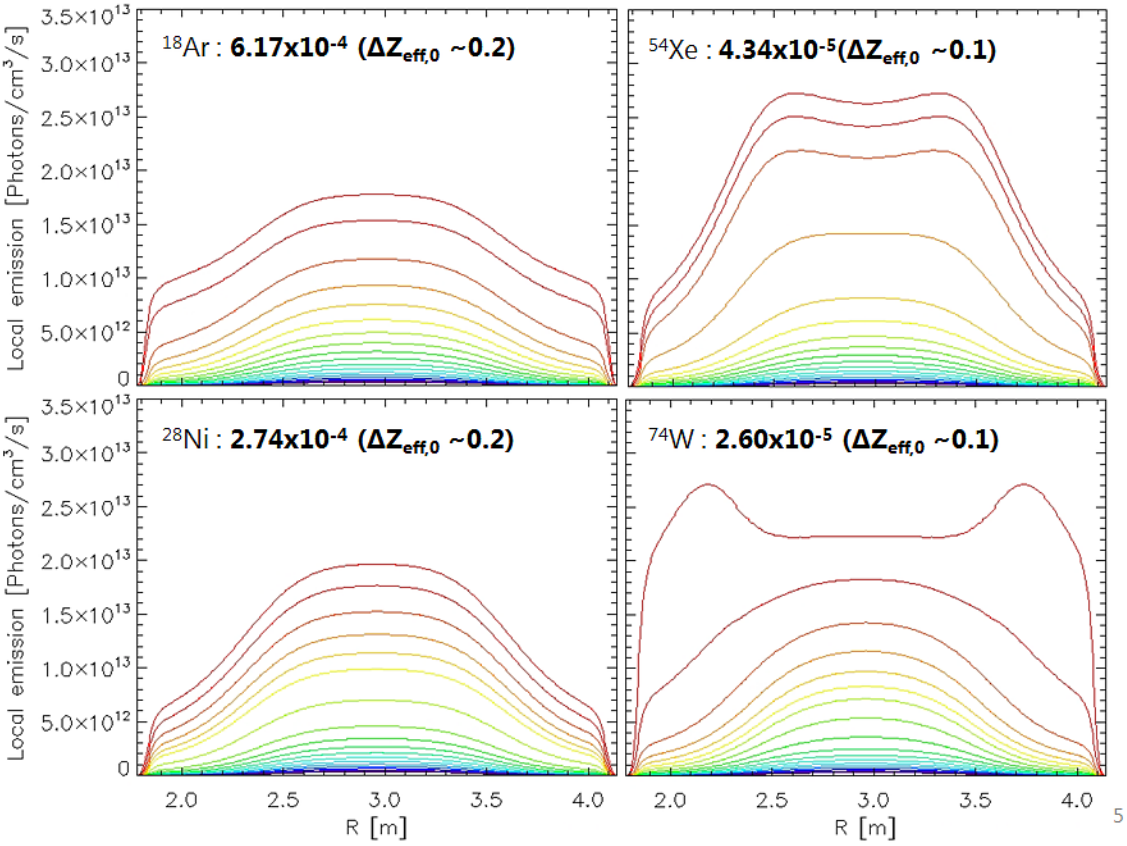

Figure 3.23: Calculation results with variety of impurities, (a) Ar, (b) Ni, (c) W and (d) Xe.

3.4 Design for TST-2 lower hybrid current driven plasmas

The ME-SXR system in TST-2 has been designed to measure HXRs with the photon energies below 20 keV from fast electrons generated by LHW. Since the FLYCHK calculation assumes a Maxwellian for the electron distribution function, emissivity of the plasmas with non-Maxwellian distribution function cannot be calculated. Therefore, we performed two approaches to estimate SXR radiation and to design camera settings.

Assuming a second Maxwellian with a constant fraction of $n_{\mathrm{fast}}/n_{\mathrm{e}}$

In order to calculate emissivities using FLYCHK, fast electron distribution function is assumed as a second Maxwellian. In this calculation, ratio of the fast electron density is set as 3 % of bulk electron density. Effective temperature of the fast electron is set to be 20 keV, which is a highest temperature in the database we developed.

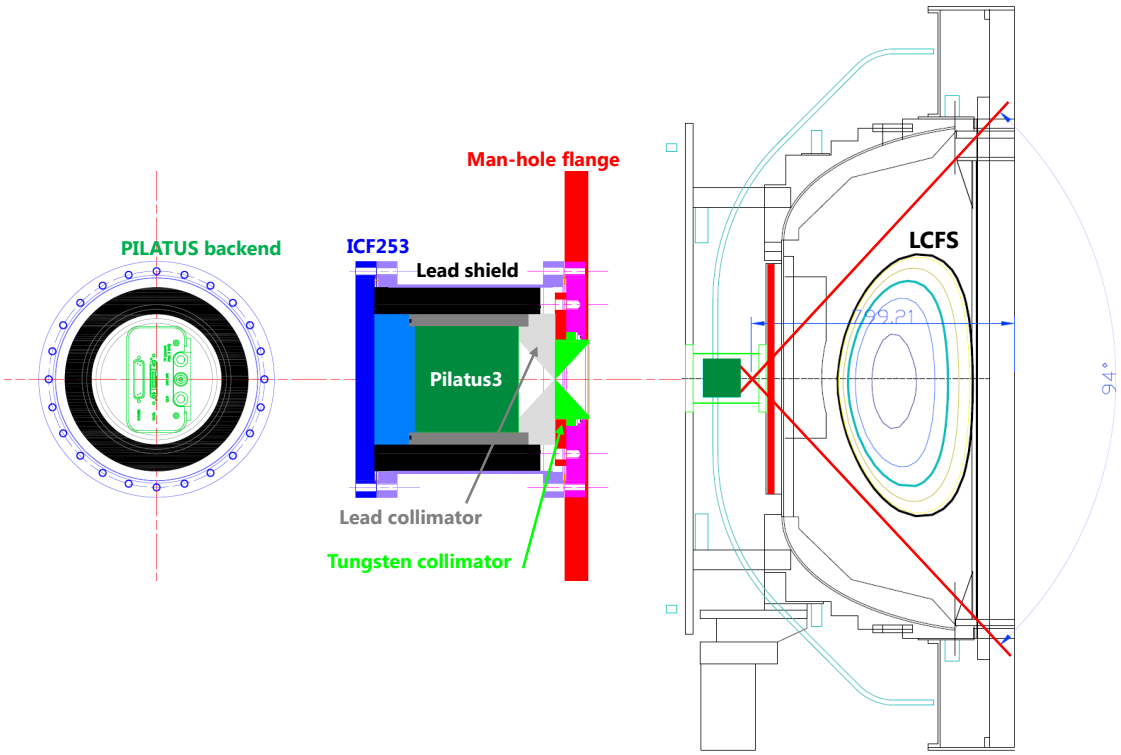

Figure 3.24: Design for the ME-SXR measurements for TST-2 LHCD plasmas.

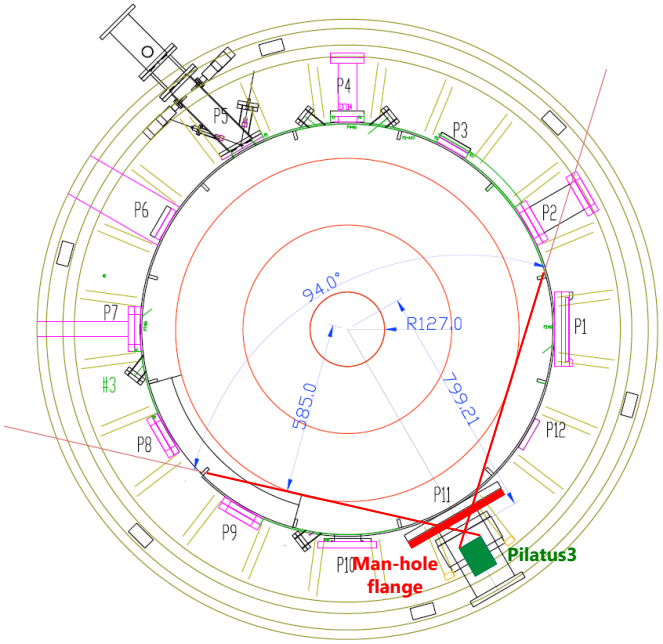

Figure 3.25: Design for the ME-SXR measurements for TST-2 LHCD plasmas.

Chapter 4

Experimental results

4.1 Results of double filter soft x-ray measurements in LH power modulation experiments

In order to detect a thick target emission from stainless steel, which is the main material of vacuum vessel and other metallic components, soft x-ray measurements with two different filters have been performed.

We used Fe: 10 μm and Al: 200 μm filters to detect the characteristic line emissions of stainless steel. Figure 4.1 shows result in LH power modulation experiment. The left two plots indicate signals of SBDs with both iron and aluminum filters and their ratio $I_{\mathrm{Al}}/I_{\mathrm{Fe}}$ and the right plots are the waveforms of plasma current I_{p}, injected LH power P_{LH} and line integrated density n_{el}. I_{p} and n_{el} showed weak modulation less than 5 % as a result of 100 % modulation at 1011 Hz for LH power. The expanded view of the ratio is shown in Fig. 4.2, which indicates the fluctuation of the ratio synchronized with modulation. It should be noted that I_{Al}, which is expected to reflect the continuum part of the x-ray spectrum do not respond to the P_{LH} modulation.

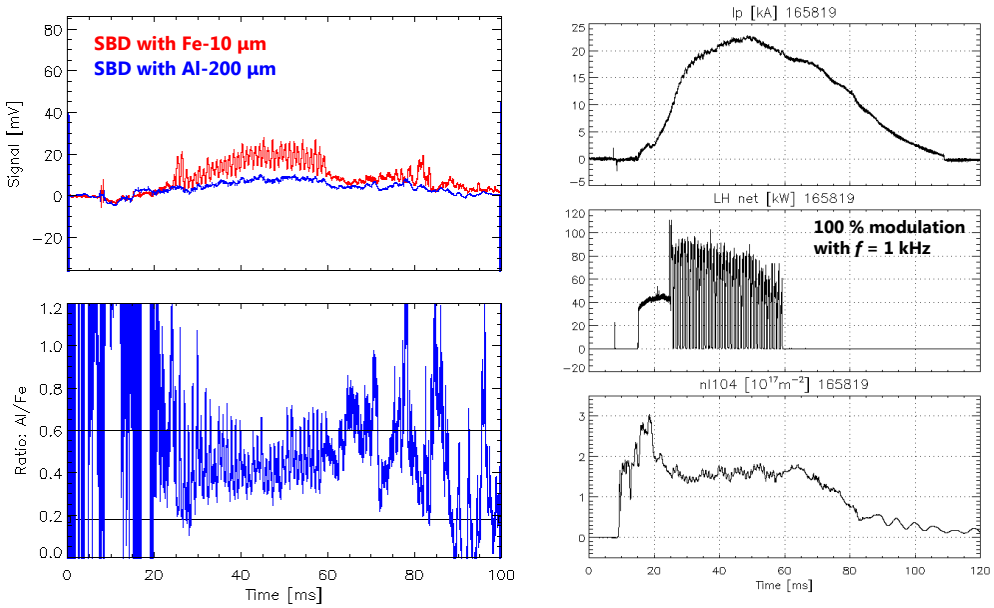

Figure 4.1: Result of power modulation experiments using double filter.

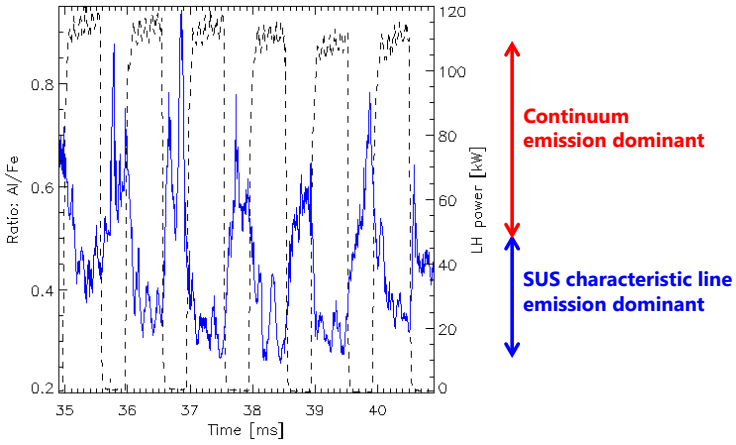

Figure 4.2: Enlarged view for a time window between 35 to 45 ms of the signal ration.

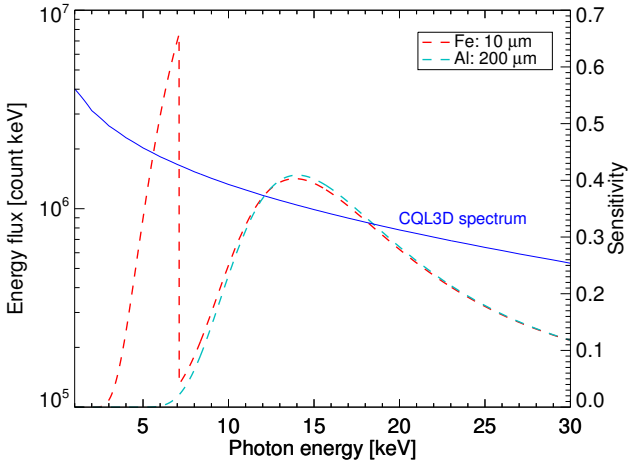

Figure 4.3: HXR spectrum simulated by GENRAY/CQL3D (shown by blue curve) and total sensitivities for two filters (shown by dashed curves).

As calculated in Table. 2.2, the signal ratio is predicted to be 18 % when the line radiation from stainless steel is measured, and around 85 % when a thick target emission from molybdenum is measured.

As a result, it was found that the SXR emission observed during the LH power is ON was dominated by the characteristic line radiation from stainless steel. On the other hand, the ratio is recovered within ∼1 ms when the injected LH is dropped off.

Here we calculated the signal ratio for the case where the radiated spectrum is continuum (Bremmsstrahlung) emission from LHW plasmas. The spectrum is simulated by the Fokker-Plank equation solver CQL3D coupled to a ray tracing code GENRAY and the calculated ratio of the two filters is 66.7 % (Fig. 4.3). This result also suggests that the x-ray spectrum measured at the time when LH power is OFF is not dominated by the thick-target radiation. The quick response of the ratio to the P_{LH} modulation indicates the fast electrons inducing the thick target radiation have a very short confinement time. This fact suggests that the fast electrons exist at the plasma edge region, where high energy particles easily hit the wall and do not contribute to the plasma current I_{p}. In contrast to the I_{Fe}, I_{p}, n_{e} do not show a large response to P_{LH} modulation, and these results suggest that the I_{Al} (and the continuous x-rays) reflects the fast electrons sustaining the plasma current I_{p}.

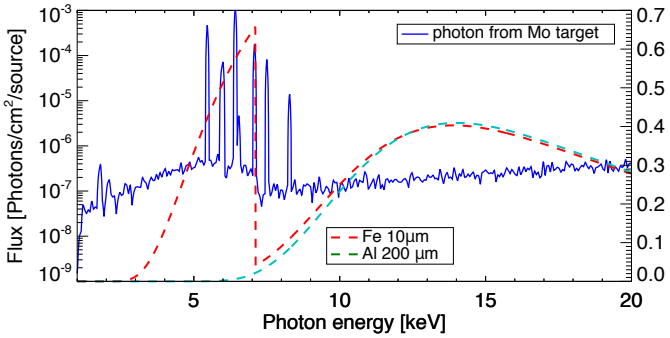

Figure 4.4: Characteristic line emission from SUS calculated by PHITS (solid line) and transmission curves for two different filters: Fe and Al.

It should be noted that the characteristic x-rays of SUS are emitted not only by the fast electron injection but also by the injection of the x-ray with the photon energy larger than the values of absorption edges. Figure 4.4 shows line emission from SUS wall by x-ray injection with the temperature of 10 keV. This line emission can also be detected by the double filter method. Therefore, it is difficult to distinguish between electrons and x-rays that cause thick target radiation from SUS.

4.2 Results of hard x-ray measurements on TST-2

As described in Sec. 2, x-ray radiation from a plasma consists of line spectrum and continuum spectrum. Since TST-2 plasma has relatively low electron temperatures: 40 eV at the core for LHCD plasmas, or 400 eV for OH plasmas, Bremsstrahlung from fast electrons generated by LHW is a main component of the HXR radiation. Figure 4.5 shows x-ray spectra measured at LHCD and OH plasmas by scintillation detector located at mid-plane, which indicates that the high flux and high energy HXRs are observed only at LHCD plasmas. It is notable that some electrons in OH discharges can be accelerated by the positive loop voltage during plasma current ramp-down phase, and they would emit a high energy Bremsstrahlung x-ray. A critical energy which represents minimum energy of electron to start acceleration under the given loop voltage V_l is estimated as [137]

$$E_c = \frac{n_e e^3 \ln\Lambda}{8\pi\varepsilon_0 E} \approx 0.21 \times 10^{-19} n_e \frac{\ln\Lambda}{V_l/2\pi R_0}. \tag{4.1}$$

In the case of a typical TST-2 OH plasma, electrons with the energy above few keVs can be accelerated to several hundreds keVs during the plasma current ramp-down phase.

In this section, HXR spectra measured by several probes during LHCD experiments conducted on TST-2 are described.

4.2.1 Spectral comparison among outboard- and top-launch CCC antennas

HXR profile measurements were performed by the NaI scintillation detector on the mid-plane and the effective temperature $T_{\rm eff}$ calculated from its slopes was obtained. Figure 4.6 shows waveforms of the discharges with different antenna and resultant spectra. The two discharges have the same plasma current and the density but the discharge indicated by blue curves was sustained by using the top antenna and one indicated by red curves was sustained by the outboard antenna. Note that the plasma sustained by the top antenna was ramped up by the outboard antenna and later, it was switched to the top antenna because plasma ramp up with the top antenna alone was quite difficult. The data for each sight line was obtained by accumulating five

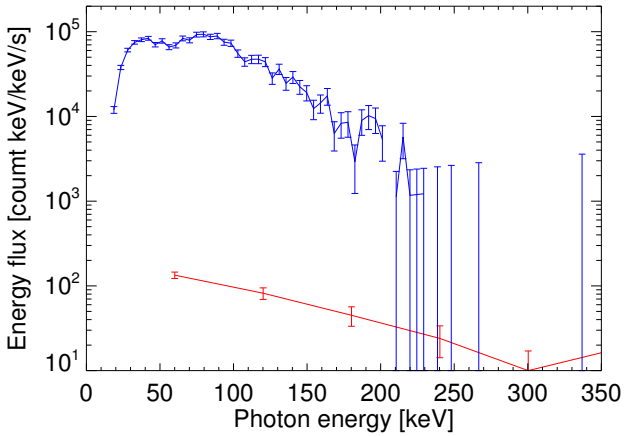

Figure 4.5: An x-ray spectrum with fast electron generated by LHW (blue curve) compared to spectrum at OH discharge (red curve).

reproducible discharges for 50–55 ms, where I_p was a flat top because the fast electrons can be accelerated by the positive loop voltage when the plasma current starts decreasing. PHA was performed for the data and a spectrum is calculated.

The resultant spectra shows that the higher energy flux and the higher effective temperature at the high field side (HFS) in the top-launched cases, while in the outboard-launched cases the energy flux and the effective temperature do not depend on sightlines. It should be noted that the effective temperature is calculated from the data in the region above 100 keV because the lower energy data are sensitive to the low transmittance of windows so that the data contain large uncertainty.

The spectral trends obtained from discharges with different antennas are qualitatively consistent with the results predicted by the simulation, but the radiated energy flux is much larger than that of the numerical results. It is strongly suggested that there is a loss of LH power used for current drive and a mechanism of HXR radiation that is not considered in the numerical simulation (discuss in Chapter 5).

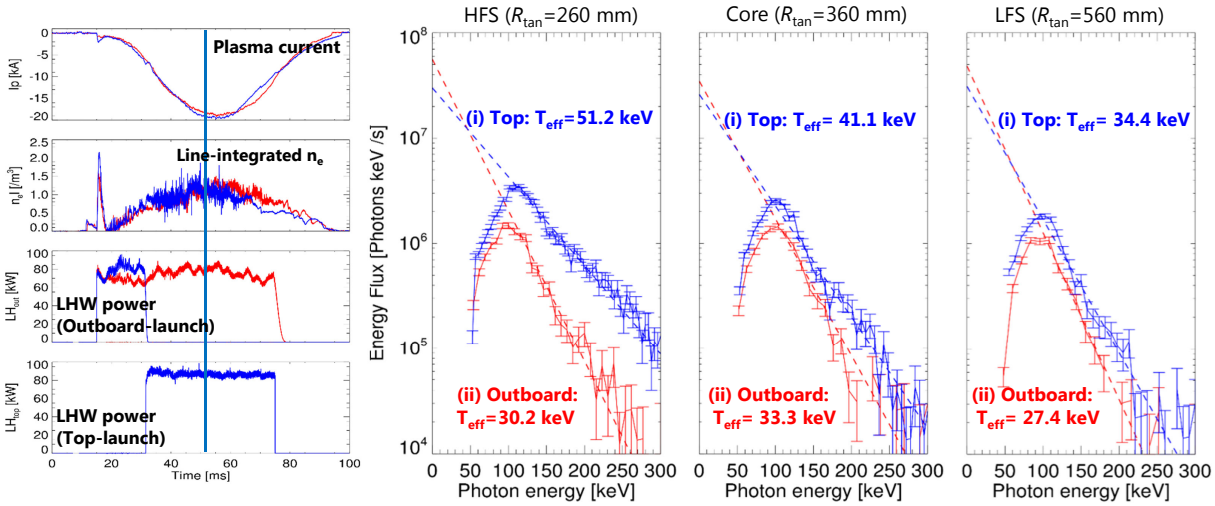

Figure 4.6: Results of HXR profile measurements. Blue curves indicate a discharge sustained by using the top antenna and red curves indicate that of using the outboard antenna.

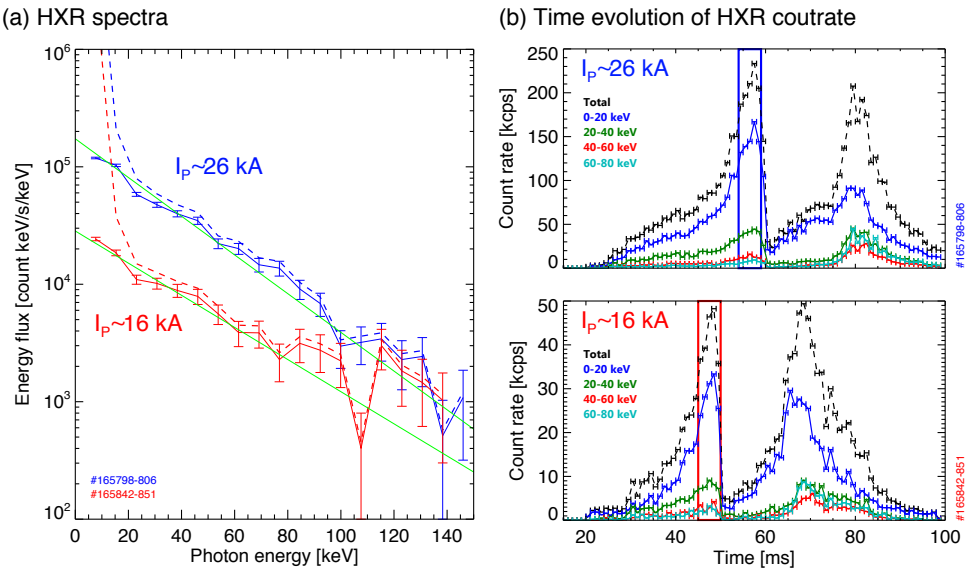

Figure 4.7: Resultant spectra measured by vertical sightlines (a) and time evolution of the HXR count rate (b).

4.2.2 Vertical sightline measurements through thin PEEK flange

The aims of this vertical sightline measurements are to eliminate thick target emission from the metallic structure and to focus on lower energy x-rays (20-100 keV), and thus the vertical sightline was designed not to see the metallic structure. Figure 4.7 shows results of two types of discharge with the plasma current $I_{\rm p} \sim 26$ kA (indicated by blue curve in (a)) and $I_{\rm p} \sim 16$ kA (indicated by red curve in (b)). Since the count rate is low because of the small solid angle, ten reproducible discharges are analyzed for each case. Detected HXR was attenuated by the PEEK flange and reflected in the scintillator crystal. The corrected spectra taking into account an absorption of the scintillator crystal and a transmittance of PEEK (see Fig. 2.23 (a)) are illustrated by dashed curves. Thanks to the good characteristics of X-ray transmission of the thin PEEK flange, HXR spectra with low energy ranges are measured and these spectra show the structure that strongly depending the plasma current.

The time evolution of HXR count rates with four different energy bands with the energy steps of 30 keV are obtained and illustrated in Fig. 4.7 (b). The LHW is injected from $t = 15$ ms to 60 ms for high $I_{\rm p}$ discharge and from 15 ms to 50 ms for low $I_{\rm p}$ discharge. Results indicate that the HXR flux decreased rapidly right after the LH is turned off. Note that the large HXR flux in the latter half of the discharge is due to the electrons accelerated by the loop voltage induced by the decrease of plasma current.

4.2.3 Evaluation of the fast electron confinement time

Time evolution of HXR radiation

The time evolution of HXR flux was investigated for both radial and vertical sightline measurements. Since a pulse count is not enough to obtain a spectrum in a short time width, the time evolution of the count rate without discrimination was obtained. First, by turning off the LH injection during the plasma ramp-up phase, relaxation time of the fast electron was estimated.

Figure 4.8 shows the discharge waveforms of the plasma with the plasma current of ~ 17 kA (Fig. 4.8 (a)) sustained using the top antenna, and the injected LH power was turned off at $t = 32.7$ ms (Fig. 4.8 (b)). Figures 4.8 (c) and (d) indicate time evolution of HXR count rate with the time steps of 0.1 ms measured

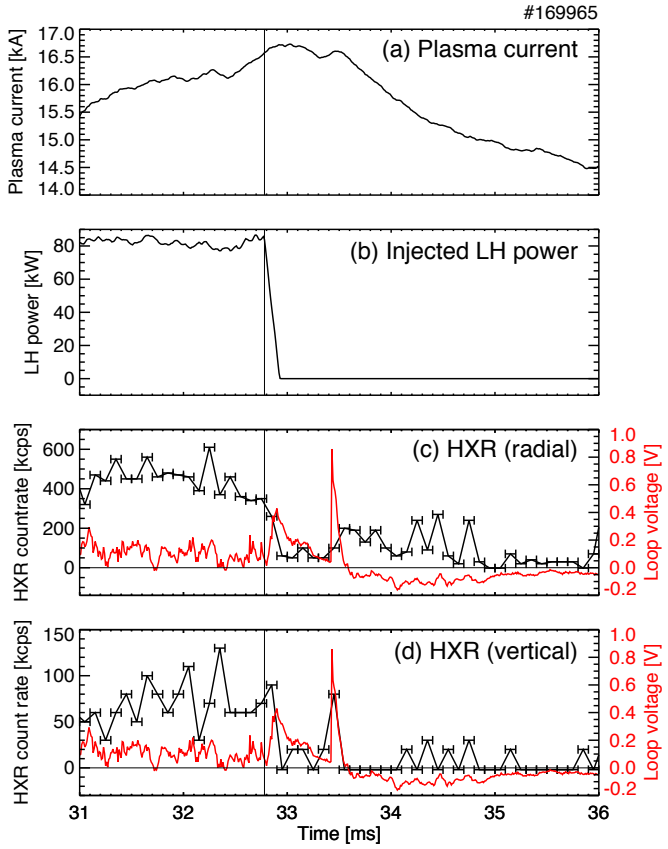

Figure 4.8: Time evolution of HXR count rate for both radial and vertical sightline. Waveforms of (a) plasma current and (b) injected LH power. (c) Time evolution of the HXR count rate by radial sightline and (d) by vertical sightline. Time evolution of the loop voltage is plotted in (c) and (d) by red curves.

by radial and vertical sightlines (black curves). The HXR count rate decreased at the same time that the LH was turned off, and showed very fast changes within 0.2 ms for radial sightline, and 0.1 ms for vertical sightline. The time evolution of the loop voltage illustrated by red curves in Figs. 4.8 (c)-(d) is synchronized with the decrease in the HXR count rate measured by radial sightline. It is considered that the loop voltage is applied due to the rapid decreasing of the fast electron sustaining the plasma current, and the electrons in the lower energy region (i.e. bulk electron) start carrying the plasma current.

RF power modulation

In order to estimate the relaxation time more accurately, LH power modulation experiments are performed and much higher count of HXR was obtained by integrating multiple periods of the modulation.

The results of double filter soft x-ray measurements (Sec. 4.1) suggest that the x-ray radiation during the OFF phase of P_{LH} is not contaminated with thick target radiation and reflects confined fast electrons contributing the plasma current. Therefore, modulation experiments are also helpful to study the wave physics and the current drive mechanism. In these experiments, the amplitude of the incident LHW power P_{LH} was modulated.

As a result of 100 % power modulation for the top-launched discharge, the x-ray count with the photon energies above 50 keV showed $\sim$ 80 % modulation in synchronization with the phase of the injected LH power (Fig. 4.9 (a) and (b)). The amplitude of the fluctuation of the HXR count rate and the fall time does

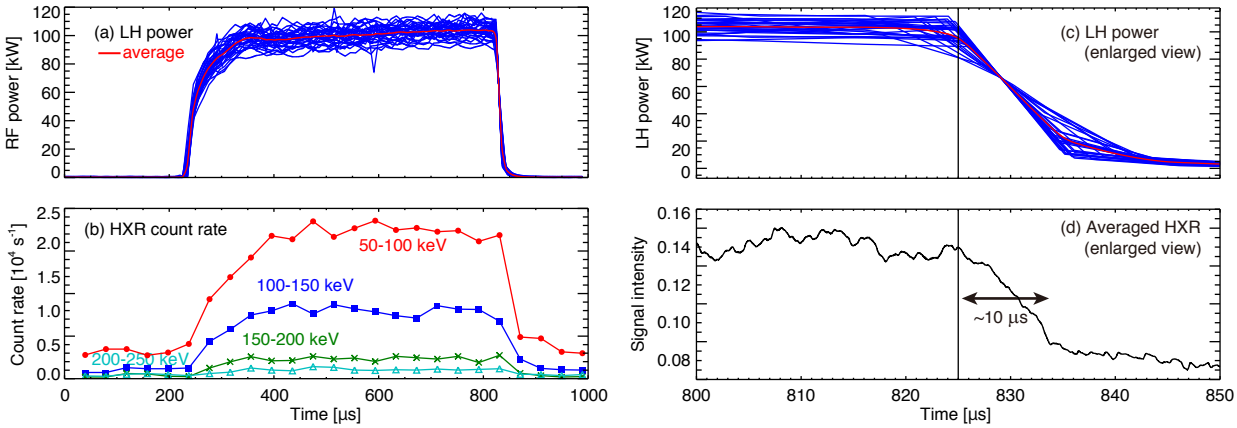

Figure 4.9: HXR spectrum of modulation experiment with a frequency of 1011 Hz. The blue curves in (a) and (c) indicate injected LH power for each periods and red curve illustrates an average power. Figure (b) shows time evolution of the count rate of the HXR radiation for several energy regions with the photon energy steps of ~ 50 keV. Figure (d) shows an averaged HXR signal intensity which indicates the relaxation time of ~ 10 μs.

not depend on their photon energy. By averaging the HXR intensities for all photon energies in each period, the time evolution was obtained. Figures 4.9 (c) and (d) are enlarged views of the time window of LH-OFF, and the average intensity of HXR suggests that the confinement time of fast electrons was about 10 μs.

Here, the electron–ion relaxation time τ_{ei} can be estimated as [2],

$$\tau_{\mathrm{ei}} = 1.51 \times 10^{-4} \frac{T_{\mathrm{e}}^{3/2}}{Z_{\mathrm{i}}^2 (n_{\mathrm{i}} 10^{-20} \ln \Lambda)} \approx 130 \text{ ms}, \tag{4.2}$$

where T_{eff} is an effective electron temperature $T_{\mathrm{eff}} = 40$ keV, Z_{i} is an ion charge ≈ 2, an ion density $n_{\mathrm{i}} \approx 5 \times 10^{17}$ m^{-3}, and $\ln \Lambda$ is known as "Coulomb logarithm" of which typical value is about 15 [138]. The relaxation time we estimated experimentally is extremely short compared to the theoretical fast electron confinement time of ~ 100 ms.

Here, we assume fast electrons with the density of less than 1 % of the bulk electron density carries a plasma current, stored energy of the fast electron can be approximated as ~ 100 J. If measured HXR reflects bremsstrahlung of the fast electron, RF power must be 10 MW or more to sustain fast electrons with 100 J of stored energy in a steady state with a confinement time of 10 μs, which is inconsistent with experimental conditions. Therefore, the existence of HXR radiation by a mechanism other than collision with ions is suggested.

4.2.4 X-ray radiation depending on plasma position

Dependence of the HXR flux on the plasma position was investigated by using both radial and vertical sightlines. Two discharges #169199 and #169219 shown in black curve and red curve in Fig. 4.10 respectively, have fixed plasma current (Fig. 4.10 (a)), LH power (Fig. 4.10 (b)) but different radial positions (Fig. 4.10 (c)). Figure 4.10 (d) and (g) show the time evolution in the count rate of HXR flux measured by radial and vertical sightlines, and Fig. 4.10 (e)-(f) and (h)-(i) show the count rate for each energy region analyzed by PHA.

As a result of the measurement, the radial sightline indicates a large difference in that the signal decreased when the radial position of the last closed flux surface (LCFS) is large, while HXR count rate measured by the vertical sightline showed a small dependence on the plasma position. Figure 4.11 indicates that the

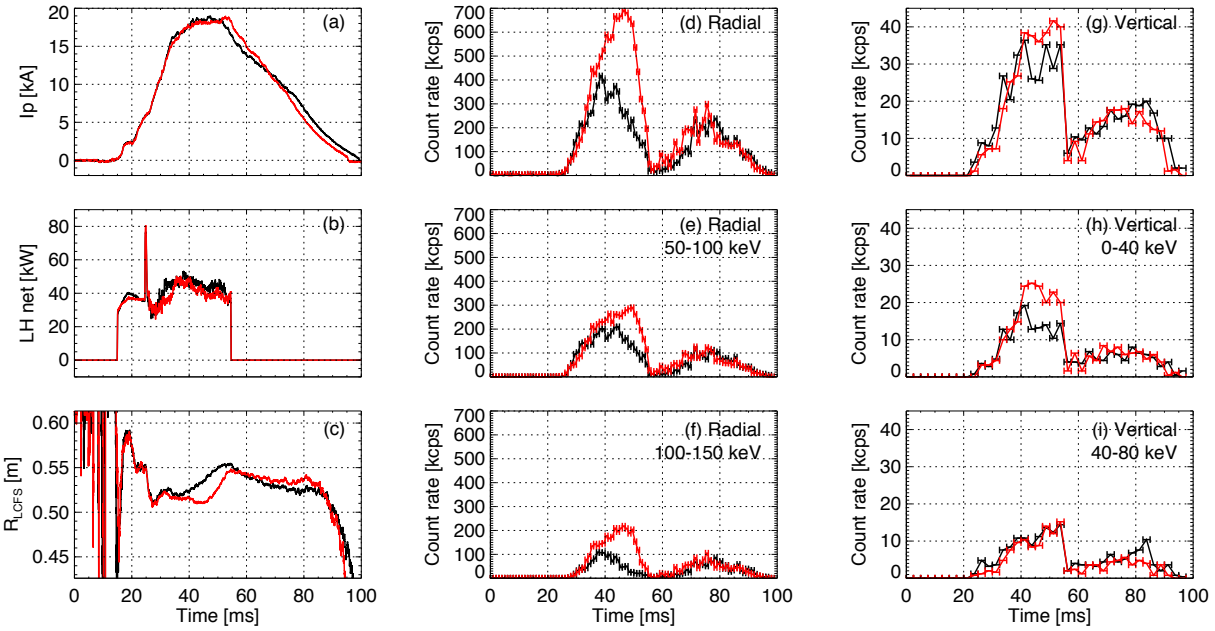

Figure 4.10: Time evolution of HXR count rate for difference discharges:#169199 (black) and #169219 (red). Wave forms of (a) plasma current $I_{\rm p}$, (b) injected LH power and (c) radial position of LCFS. Time evolution of HXR count rate are obtained by radial sightline (d)-(f), and vertical sightline (g)-(i).

average energy of the radiated HXR $\langle E_{\rm ph}\rangle$ (Figs. 4.11 (b) for #169199 and (d) for #169219) depends on the distance (Figs. 4.11 (a) for #169199 and (c) for #169219) between radial position of the plasma LCFS $R_{\rm LCFS}$ and the antenna limiter $R_{\rm lim} = 585$ mm. This results also show that the correlation between ΔR and $\langle E_{\rm ph}\rangle$ has a delay of ~ 2 ms.

Figure 4.11 (e) shows $\langle E_{\rm ph}\rangle$ versus ΔR from $t = 30$ ms to $t = 60$ ms with the time steps of 1 ms for two discharges, and it was found that the radiated photon energy $\langle E_{\rm ph}\rangle$ is linearly correlated with the distance between plasma and the outboard limiter (blue line in Fig. 4.11 (e)). This relationship leads to the possibility of the mechanism that the fast electrons accelerated in the plasma collide with the antenna limiter and emit HXRs.

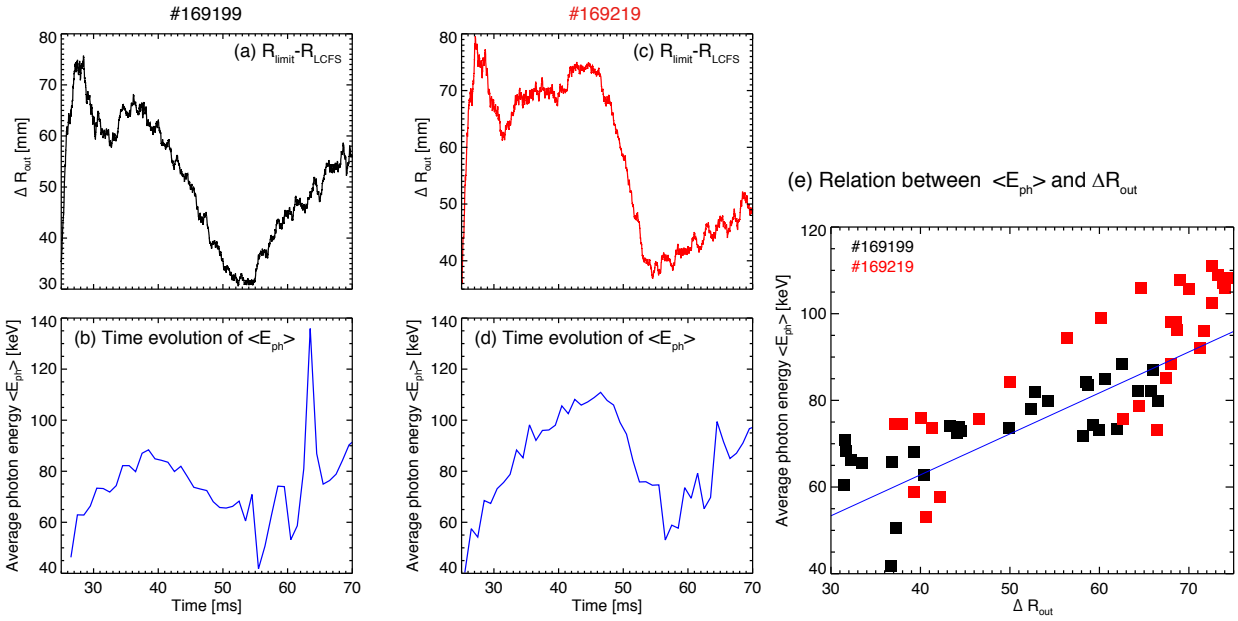

Figure 4.11: The average energy of the radiated HXR $\langle E_{\mathrm{ph}} \rangle$ depends on the distance ΔR between radial position of the last closed flux surface (LCFS) plasma R_{LCFS} and the antenna limiter $R_{\mathrm{lim}} = 585$ ms.

Chapter 5

Discussion

5.1 Comparison between experimental results and simulations

Comparing measurement and simulation results is one of the key topics of this study. As described in Sec. 4.2.1, HXR profile measurements show the difference in energy flux and effective temperature depending on the antenna position and sight line. This trend that the higher effective temperature - which suggests that the fast electrons are generated more efficiently - in the top-launched case compared to the outboard-launched case is consistent to the simulation result of the ray tracing code GENRAY shown in Fig. 5.1 [48]. Figure 5.1 shows that the LH waves incident from the top side of the plasma show a strong up-shift on the HFS side of the device (Fig. 5.1 (a)), while LH waves incident from the outboard side propagate with slowly increasing $n_{\parallel}$. However, according to the results of a double filter soft x-ray measurement (see Sec. 4.1), the resultant spectra may be "contaminated" by thick target x-ray radiation. Since stainless steel has characteristic lines with photon energies only below 10 keV, the contamination in HXR range (above 20 keV) is a continuum spectrum and thus, the Bremsstrahlung spectrum shape (including T_{eff}) is not distorted, but the energy flux is changed.

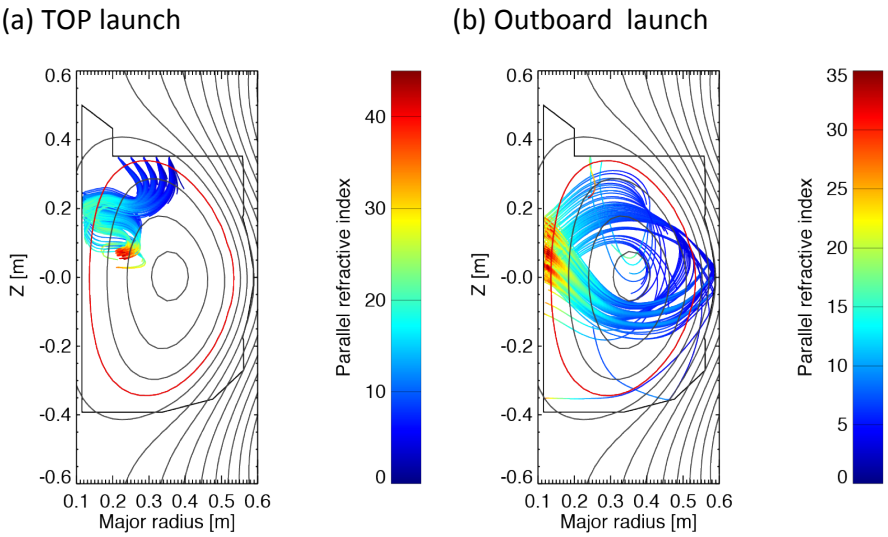

Figure 5.1: Wave propagations simulated by a ray tracing code GENRAY [48] for (a) top-launched case and (b) outboard-launched case [139].

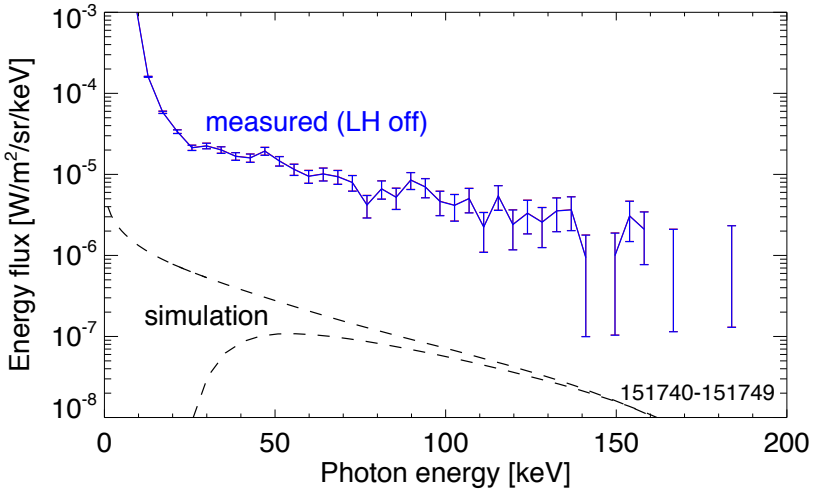

Figure 5.2: Comparison between simulated and measureed spectra.

We measured spectra using PEEK flange with vertical sight line in order to eliminate a thick target x-ray radiation. The x-ray radiance $\mathcal{F}$ from plasmas can be calculated from the energy flux measured by HXR detector $F_{\rm meas}$ as

$$\begin{aligned}\mathcal{F}(E) &= F_{\rm meas}(E) \times 10^3 \ [\text{count} \cdot \text{eV}] \times 1.6 \times 10^{-19}/S/\Omega/\Delta E \\ &\approx 2.5 \times 10^{-9} F_{\rm meas}(E) \ [\text{W/m}^2/\text{sr/keV}],\end{aligned}$$

where, the cross section of pinhole is $S = \pi(0.0035\ [\text{m}]/2)^2$, solid angle is $\Omega = 0.005$ [sr], bin size of the spectrum is ΔE =1 [keV]. Figure 5.2 shows comparison between the experimental radiance $\mathcal{F}$ and the radiance simulated by the Fokker-Plank equation solver CQL3D coupled with GENRAY. The spectrum is measured by vertical sight line and during the LH power is off, and it is therefore considered unaffected by thick target radiation. However the experimental x-ray radiation is still anomalously higher than the simulation result.

In the comparisons between measurement and simulation, driven plasma current shows a large discrepancy as well as the x-ray radiation. The simulated plasma current was higher for top-launch, which quantitatively consistent with the experimental result, but the predicted plasma current is higher than the experiment one by a factor of 3-5 (Fig. 5.3) [141]. This fact leads to two possibilities: (1) the calculated fast electron distribution function generated by LHW is quite different from the distribution in the experiment and (2) a major part of the generated fast electrons do not carry the plasma current and lost immediately. The former possibility is considered to be denied because the spectra measured by the discharges using different antenna configurations qualitatively match the calculation result. The latter is considered reasonable because the time evolution of the HXR count rate in the modulation experiment showed a much faster variation than that of the plasma current. That is, the fast electrons that do not carry the current are not confined and emit a large amount of HXRs. Experimentally estimated fast electron confinement time is much shorter than theoretical one, and the results also support this possibility that the fast electrons are rapidly lost. In addition, as described in Sec. 4.2.4, a radiation process is considered that the fast electrons in the plasma collide with the antenna limiter and emit HXRs.

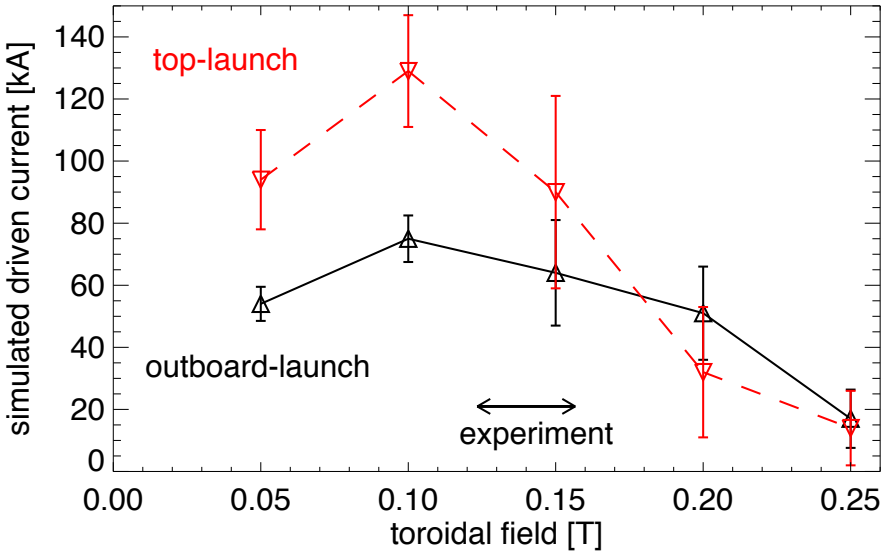

Figure 5.3: Predicted plasma current by simulation. Simulated driven currents are higher than the experiment regime (depicted by arrow) by a factor of 3–5 [141].

5.2 X-ray radiation from the outboard limiter

The experimental results suggest that the x-ray radiation due to the fast electron loss other than bremsstrahlung is considered to be a major loss mechanism in the LHCD plasmas. One of the candidates is a thick target radiation from the antenna limiter due to the collision of fast electrons accelerated by the LHW. In order to estimate the thick target radiation at the antenna limiter, transport and diffusion of the fast electron are modeled by considering an RF induced radial transport [142]. The RF induced radial transport has originally been suggested for describing effect of the ion cyclotron range of frequencies (ICRF) waves on radial transport of ions in tokamak plasmas [143]. Applying the RF induced transport model to the TST-2 LHCD plasmas, electron parallel velocities $v_{\parallel}$s are calculated. The acceleration of electrons by LHW is assumed to occur at the inboard side which is predicted by previous numerical simulations [49,140], and the deceleration due to the collisions with bulk electrons, ions and neutrals are calculated through a random walk [142]. When the velocity of the fast electron becomes large and its orbit reaches the outboard antenna limiter, the fast electron is lost by the collision with the Mo (Molybdenum limiter) attached on the antenna (Fig. 5.4 (a)). Figures 5.4 (b)-(d) show simulated spectra of the thick target x-ray emission from Mo (Fig. 5.4 (b)), spectra of the x-rays after a reflection at the SUS wall (Fig. 5.4 (c)) and plasma bremsstrahlung from fast electrons with the effective temperature of 30 keV (Fig. 5.4 (d)). Colors indicate two cases with different R_{LCFS} (red curves for $R_{\mathrm{LCFS}} = 0.515$ m and black curves for $R_{\mathrm{LCFS}} = 0.540$ m). Since the HXR detector is located outside the vacuum vessel, transmission of the SUS wall is also taken into account in these spectra.

Figure 5.5 (a) shows the thick target radiation from the outboard limiter (solid curves) and experimental results of the HXR spectra obtained by radial sightline in during the period from $t = 46$ ms to 48 ms (illustrated by symbols) . Comparison between the simulation and the measurement showed that the tendency that higher energy flux is radiated when R_{LCFS} is small was in good agreement for the two cases with different R_{LCFS}. Note that the values of simulated radiation are multiplied by a factor of $1/3000$ in the plot because thick target radiation is much larger than the experimental result.

In the model, the kinetic energy of the fast electron colliding against the limiter is approximated as

$m_e V_{loss}^2/2$, and the velocity V_{loss} can be expressed by using model parameters R_{sout}, R_{sin} and Ω_{pe} as

$$V_{loss} = \Delta R_{LCFS} \frac{R_{sout}}{R_{sout} - R_{sin}} \Omega_{pe},$$

where, R_{sout} and R_{sin} represent the initial outboard and inboard midplane striking position, and Ω_{pe} is the electron cyclotron frequency for a given poloidal magnetic field B_p. Therefore, the energy lost in the limiter ΔE_{loss} is expected to be proportional to ΔR_{LCFS}^2. Figure 5.5 (b) shows plot of the ΔR_{LCFS} versus averaged photon energy $\langle E_{ph} \rangle$ during the I_p flat top phase (from $t = 40$ ms to 52 ms). Dashed curve in Fig. 5.5 (b) indicates the quadratic polynomial fitting for the experimental data illustrated by square symbols. It strongly supported ΔR_{LCFS}^2 dependence, and the model was validated qualitatively.

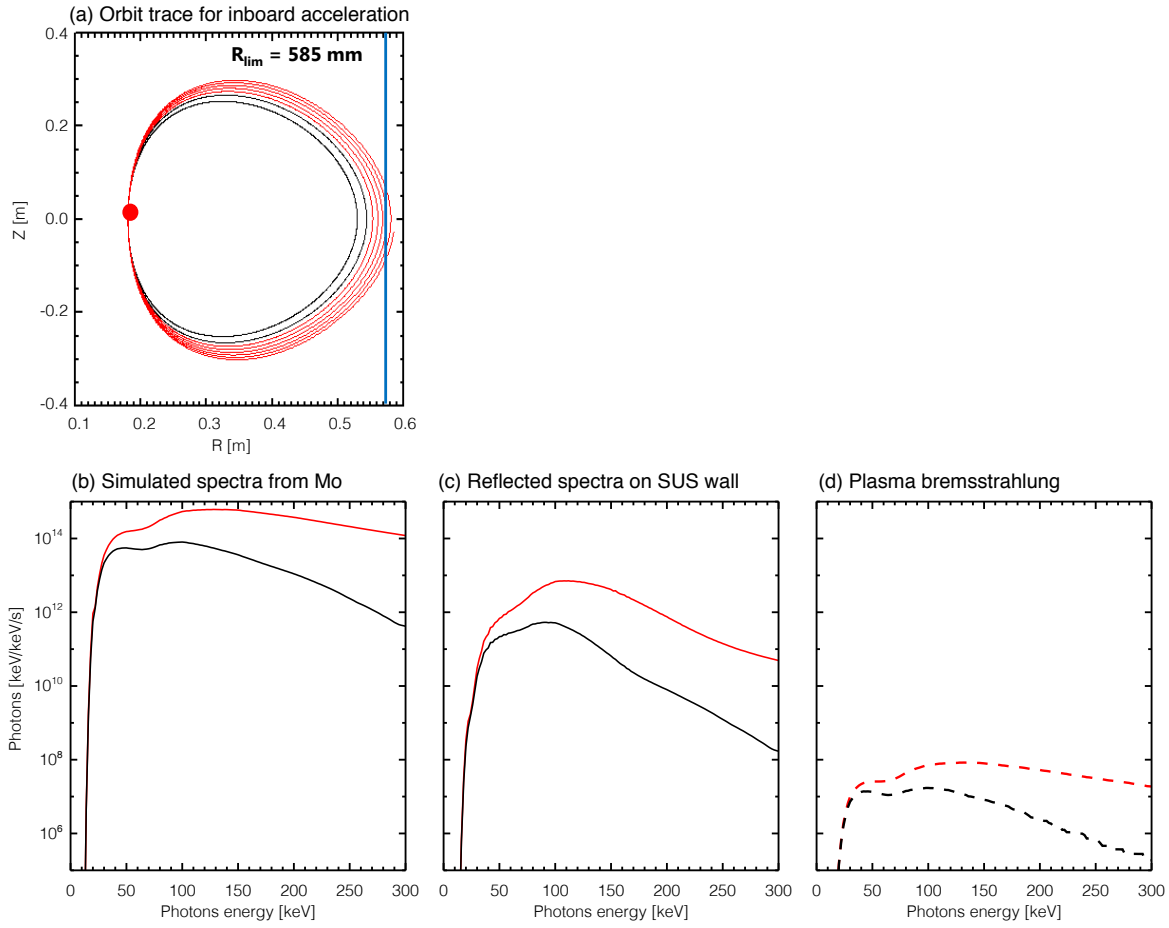

Figure 5.4: Results of calculation of the RF induced radial transport model for two cases with a difference R_{LCFS} position. (a) Trace of the orbit of the fast electron started from one particular point in the real space. Its orbit expand outward with the energy, and the electron is lost when the orbit reaches the limiter position illustrated by the blue line. (b) Simulated spectra from thick target emission from Mo limiter. (c) Simulated spectra from Mo with a reflection and transmission at the SUS wall. (d) Calculated plasma bremsstrahlung radiation.

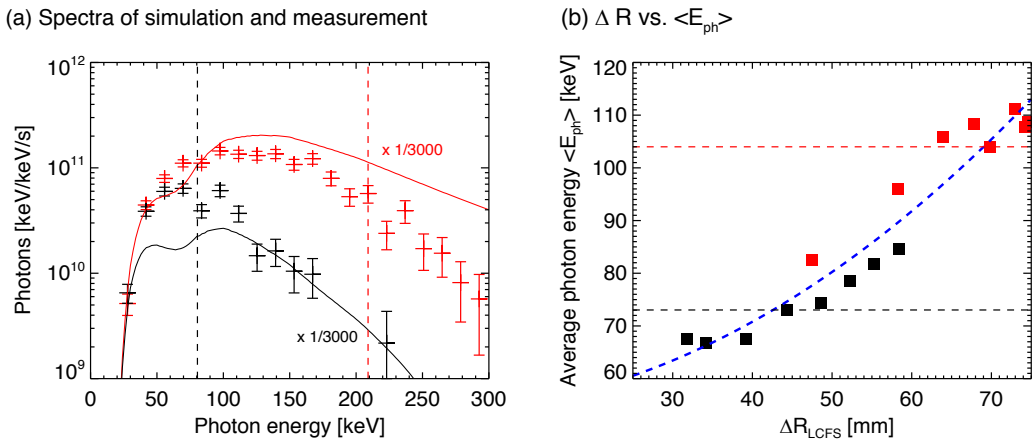

Figure 5.5: (a) Spectra of both simulation (solid curves) and measurement (symbols). Note that the thick target spectra from Mo are multiplied by a factor of 1/3000 in the plot. Dashed lines indicate the theoretical typical electron energy $m_e V_{loss}^2/2$ for two cases. (b) plot of the measured average photon energy of every 1 ms as a function of ΔR_{LCFS}. The fitting result is illustrated by a dashed curve, which indicates a ΔR_{LCFS}^2 dependence.

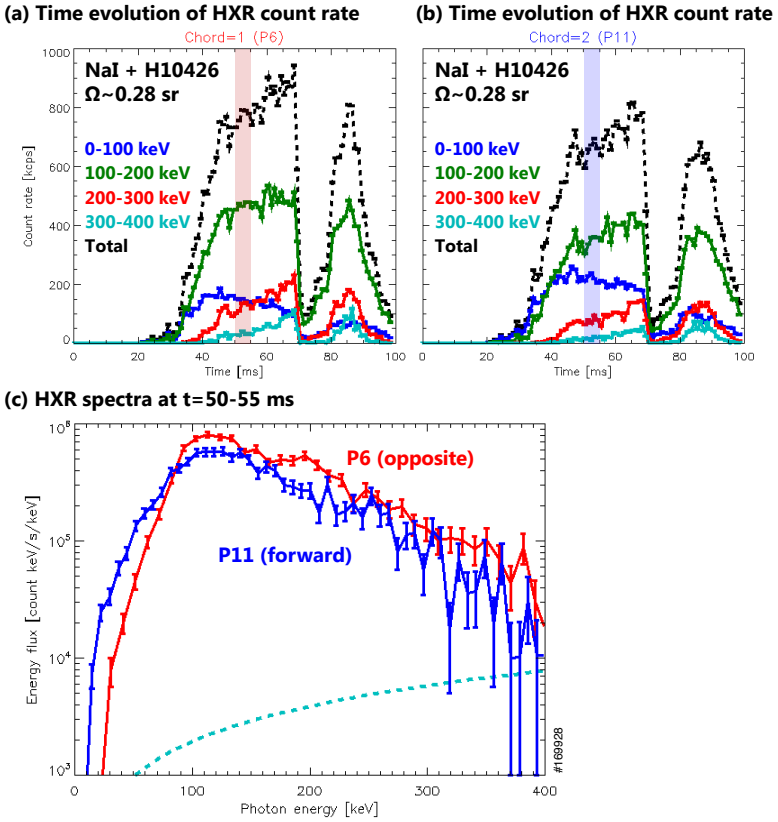

Figure 5.6: Energy flux measured from P6 (opposite) side (red curve in (c)) is larger than that measured from P11 (forward) side (blue curve in (c))

As described above, simulated thick target spectra and measured spectra are quantitatively consistent but it showed a discrepancy of roughly three orders of magnitude. This factor may be due to the anisotropy and localization of thick target emission from Mo. In order to validate this possibility, we performed same measurements but the detector is located on the opposite side of the vacuum vessel. In this case, it was expected that the signal increases due to the anisotropic radiation depending on the direction of the fast electron velocity. Resultant spectra are shown in Fig. 5.6. As a result of measurement by two sightlines, it was confirmed that the spectrum measured from the opposite direction (illustrated by red curves) showed a larger flux compared to that in the forward direction. This result suggests that the model is qualitatively correct. However, the emission anisotropy have a large uncertainty, and it is difficult to evaluate them preciously.

In addition to the anisotropy and localization, we must consider the reflection. The detector is located at the opposite side of the electron colliding surface and thus, the x-rays emitted from the limiter can reach the detector when it is reflected at the vacuum vessel. Note that the results of the double filter soft x-ray measurement described in Sec. 4.1 showing the presence of SUS lines are consist also with this model. We believe that this hypothesis can be verified by a future measurement of HXRs with the field of view that includes Mo target which causes the thick target x-ray emission.

5.3 Future plans and suggestions

Additional work needs to be performed to establish RF induced radial transport and to validate this model. One of the important experiments is the direct measurement of the thick target emission from the Mo target. Schematic drawing of this measurement is shown in Fig. 5.7. The target is inserted to $R_{\mathrm{target}} \sim 570$ mm by linear motion drive attached on Port 6 and the thick target emission will be detected by scintillation detector installed on Port 3. In the experiment, it is expected that not only the direct measurement of the thick target HXRs emitted from Mo but also the dependence between $\Delta R_{\mathrm{target}}$ and averaged energy $\langle E_{\mathrm{ph}} \rangle$ can be obtained in more detail by scanning its radial position.

Finally, methods to suppress RF induced radial transport and perform LHCD experiments more effectively are discussed. According to the calculation, more than half of the RF energy absorbed by the plasma is considered to be lost by fast electron hitting the limiter. Since the parallel velocity of the electron is accelerated by LHW and decelerated by collisions with bulk electrons, ions and neutrals, higher electron density and Z_{eff}, can reduce the energy loss by the thick target emission. In addition, acceleration point of electrons by LHW is expected to have a strong dependence on their orbit. The current model assumes that the electrons are accelerated near the HFS (inboard side) edge which is the position of RF power deposition according to the simulation Genray/CQL3D [49], but the LFS (ourboard) power deposition can suppress the outward expansion of the orbits and can improve their confinement.

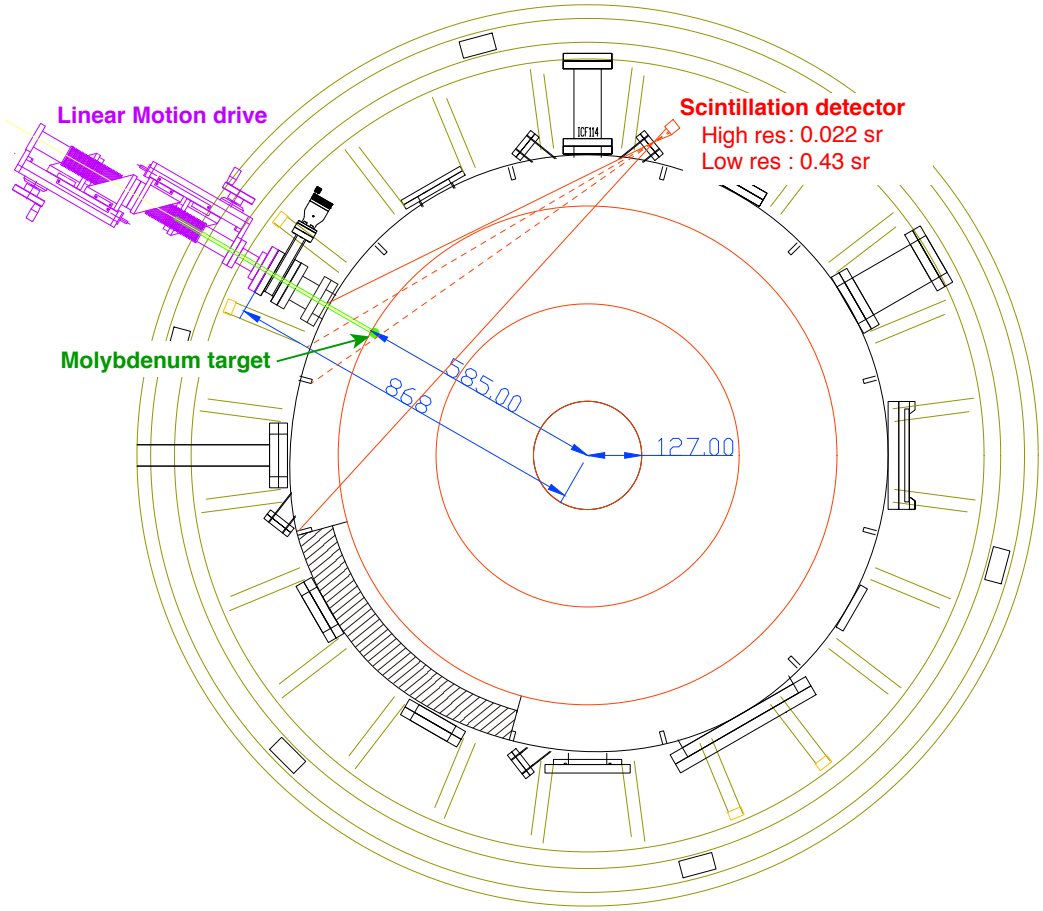

Figure 5.7: Future plan for thick target measurements. The molybdenum target is inserted by linear motion drives installed on Port-6 and measured by a scintillation detector.

Chapter 6

Conclusions

In this study, we performed experiments and measurements on TST-2 in order to investigate the formation, transport and the loss mechanism of fast electrons during the lower hybrid current drive (LHCD) in an ST configuration.

In the TST-2 spherical tokamak, we developed soft and hard x-ray measurement systems for identifying the soft x-rays emitted from a stainless steel, and for measuring the hard x-rays emitted from fast electrons, and investigated the spectra under various discharge conditions. Our work has led us to the conclusion that the major part of the LH power is lost by fast electrons colliding the antenna limiter, and the transport of the fast electron is described by the mechanism of RF induced radial transport.

We also developed a computational tool for simulation and design of ME-SXR pin-hole cameras for fusion plasmas. We performed calculation for estimating photon count impinging on each pixels of the ME-SXR detector and optimization of the spatial spectral and temporal resolution. This tool provides a powerful methodology to design and to optimize configurations of the ME-SXR methods for magnetic confinement fusion devices in the world.

Study of X-ray measurements on TST-2

In the modulation experiment, time variations synchronized with the power modulation of LHW was observed. As a result of soft x-ray measurement using two filters, Fe: 10 μm and Al: 200 μm, the signal ratio during LH-ON phase was about 20 %, suggesting the presence of the characteristic line emission from stainless steel components. On the other hand, it was found that the signal ratio was 60 % or more during an LH-OFF phase, and it indicates the measured spectrum is considered to be a continuum spectrum. These results suggest that a significant part of the x-rays during LH arises from the fast electrons hitting the walls or the limiters. These x-rays from the wall or the limiters are called thick target x-rays.

For HXR measurements, a new system using an LYSO scintillator has been developed, and it was demonstrated that the LYSO scintillation detector has an excellent sensitivity for high energy x-rays as well as a good time resolution. We also newly developed a vertical sightline HXR detector using a PEEK flange for measuring HXRs with low photon energies. The measurements shows the photon energies below 100 keV was measured successfully and the dependance on the plasma current was obtained. These spectra were considered to reflect the energy distribution function of the fast electrons.

As a result of taking advantage of the newly realized high time resolution, time evolution of the HXR count rate is obtained and it was found that the HXR flux dropped within 100 μs right after the LH power turn-off. In addition, the result of modulation experiments shows that the flux in all energy ranges decreases rapidly within 10 μs. Considering the results of the double filter SXR measurements, the spectrum during the LH-OFF phase would appear to indicate the spectrum of the fast electrons, but the slowing down time of fast electrons is much longer than the time scale of HXR flux temporal variation, and thus, It has been

suggested that the slowing down due to collisions with ions is not a dominant loss process of the fast electrons, and another loss mechanism should be searched.

We investigated the relationship between the plasma position and the HXR radiation, and consequently, we found that the averaged HXR energy detected by a radial sightline is strongly correlated with the plasma position. We developed a simulation model considering an RF induced radial transport to simulate an x-ray radiation caused by the fast electron hitting the antenna limiters. Measurements with the HXR detector located on the opposite side of the vacuum vessel were also carried out, and the results qualitatively agree with the simulation model. Expected dependence between the position and the radiated HXR energy was confirmed. Consequently, a significant RF induced transport was suggested. Although the simulated thick target x-ray spectra and the measured spectra are qualitatively consistent, the present model still shows a large deviation from the measurement results. Further experimental study is necessary.

In summary for the x-ray measurements, double filter soft x-ray measurements were developed for identifying the thick target radiation, and the presence of thick target radiation in the LH-ON phase was clarified. The HXR detector using LYSO crystal and PEEK flange has been developed, and it can cover over a wide photon energy range that could not be measured by conventional HXR detectors. Energy discrimination with high temporal resolution and evaluation of the confinement time of the fast electrons were also demonstrated. Fast electron losses due to the RF induced radial transport were modeled and discussed, and the experimental HXR radiation was qualitatively explained for the first time.

This work revealed the transport and loss mechanism of the fast electrons generated by LHW in ST configuration by measuring soft and hard x-rays.

Development of a computational tool for simulation and design of ME-SXR

For the purpose of designing the ME-SXR measurement system, a computational tool for calculating the amount of soft x-ray emission from plasma and estimating the signal of the detector was developed. This makes it possible to calculate soft x-ray emission from plasma with arbitrary electron temperature, electron density, and impurity density distribution. In addition, the signal at each pixel of the detector can be calculated considering the measurement settings such as pinhole camera geometry, energy threshold settings, exposure time, and etc.

Using this tool, we have estimated a signal intensity on the detector and optimized signal to noise ratio, and designed the ME-SXR pinhole camera system for 1-D radial profile measurements of PPCD plasmas on the MST device. The first measurement using the PILATUS3 detector was carried out. The maximum photon count rate expected to be ≈110 photons/pixel/ms for $E_C = 2.0$ keV, which agrees well with the experimental result $N_{max} \approx 80$ photons/pixel/ms within a factor of 2. This is the first verification of this computational tool by an actual plasma measurement.

We have also calculated x-ray emission profiles for both H-mode and L-mode plasmas with various condition of impurity concentrations on the DIII-D tokamak. As a result, the computed brightness of H-mode plasmas ranges from few 10^2 counts/pixel/ms depending on the cut-off energy thresholds, and the typical spatial resolution in the mid-plane will be ~ 0.5 cm with a photon-energy resolution of 500 eV at 500 Hz frame rate. We also evaluated the signal to noise ration of this 1-D profile measurement and found that the pedestal structure of H-mode profile can be clearly observed by this configuration.

Using this tool, ME-SXR measurements have been designed for several devices including TST-2 and JT-60SA, and the feasibility of this ME-SXR techniques were discussed.

In summary, a powerful and flexible computational tool for ME-SXR measurements have been developed, and it is used to optimize the design of several systems. This tool is considered to be very useful not only for designing but also for reconstructing the impurity distribution and effective charge distribution from the measurement results. We believe this diagnostic technique should be explored also as a fusion plasma diagnostic for tokamaks.

Acknowledgements

I would like to thank the following people for all their support over the course of this work, without whose help this work would not have been possible.

First of all, I would like to thank my supervisor, Professor Akira Ejiri, for his incredible support, guidance and encouragement throughout my graduate school years. He gave me a lot of valuable advice and knowledge about measurement and data analysis. Even though it was a holiday, he has spent much time for helping me with the experiments and discussing the physics that underlies the experimental results. I have learned a lot from his attitude towards research, and his dedication as a teacher for laboratory students.

Collaborative research with Princeton Plasma Physics Laboratory about ME-SXR measurement is one of the essential parts of this research, and I am grateful to Dr. Luis F. Delgado-Aparicio who has supervised me at PPPL, for his guidance, hospitality, and sponsorship. Luis-sensei taught me not only about ME-SXR measurements but also about physics and mathematics for x-ray diagnostic, as well as paper writing. Working very hard with him at PPPL was an irreplaceable experience for me.

I would like to thank Professor Yuichi Takase for supporting my Ph.D course. He gave me many suggestions about research and taught me many things in RF physics and engineering. He also gave me opportunities for collaborative research with PPPL and QST. These experiences were extremely important for me to refine my skills as a researcher. I would like to thank Dr. Naoto Tsujii for giving insightful comments and suggestions on my research, and operating LH system, although he was extremely busy. His advice has always guided me in a better directions. I also would like to thank Dr. Osamu Watanabe for his valuable advice from his extensive knowledge and skills. He provided not only much support for the research, but also mountain climbing and other activity which were very good refreshment for me. I would like to thank Professor Michiaki Inomoto, a member of my thesis committee, for giving valuable comments about this thesis and providing opportunity for experiments on the UTST device.

I would like to acknowledge those who helped and supported me at PPPL. I would like to thank Professor Masayuki Ono for his support not only for research at PPPL but also for all of my stays at Princeton, Dr. Brian A. Grierson for valuable comments and advices for calculation and design of ME-SXR measurements on DIII-D and supporting journal publication, Dr. Kenneth W. Hill for discussing FLYCHK calculation and helping me with calculation and design of x-ray spectroscopy and Dr. Nicola Bertelli for helping me with CQL3D calculation.

I also acknowledge Dr. Richard Groebner at General Atomics for his help and valuable suggestions for the journal publication at the HTPD meeting about ME-SXR design for DIII-D plasmas. I also would like to thank all members of the MST group at University of Wisconsin-Madison, especially Dr. Patrick VanMeter for supporting and hosting my visit as well as running the MST experiment.

I also wish to thank current and former members of Takase-Ejiri laboratory and UTST group. I would like to thank Dr. Takahiro Shinya and Dr. Satoru Yajima for teaching me about RF system and RF operation and helping me with experiments many times, Dr. Hirokazu Furui for teaching me about probe measurements on both TST-2 and UTST, Dr. Hiro Togashi and Mr. Yusuke Yoshida for their help and advice about all aspects of my laboratory life. I would also like to thank Dr. Kotaro Yamasaki and Dr. Tomohiko Ushiki at Inomoto laboratory for operating UTST experiments and helping me with Rogowski probe measurements

on UTST. Many thanks to my colleagues, Kazuya Toida and Wataru Takahashi for a good time in this lab. I am thankful to all other members who working together with me: Yoshiyuki Tajiri, Yuki Takei, Yongtae Ko, Yuki Aoi, James Rice, Akichika Kitayama, Naoki Matsumoto, Akito Sato, Yi Peng, Yusuke Iida, Kotaro Iwasaki, Yuya Kawamata, Sho Sakamoto, Kyohei Matsuzaki and Yuki Osawa.

Lastly, I would like to thank my parents, my sister and other members of my family for their continuous love and support.

References

[1] INTERNATIONAL ATOMIC ENERGY AGENCY, *Fusion Physics* , IAEA, Vienna (2012), Available at `https://www.iaea.org/publications/8879/fusion-physics`

[2] J. P. Freidberg, *Plasma Physics and Fusion Energy*, Cambridge University Press, Cambridge, 2007.

[3] J. D. Lawson, "Some Criteria for a Power Producing Thermonuclear Reactor", Proc. Phys. Soc. B, vol.70, no.1, p.6, Dec. 2002.

[4] Marco Ariola, Alfredo Pironti, *Magnetic Control of Tokamak Plasmas*, Springer-Verlag, London, 2008.

[5] T. Fujita, T. Hatae, T. Oikawa, S. Takeji, H. Shirai, Y. Koide, S. Ishida, S. Ide, Y. Ishii, T. Ozeki, S. Higashijima, R. Yoshino, Y. Kamada, and Y. Neyatani, "High performance reversed shear plasmas with a large radius transport barrier in JT-60U", Nucl. Fusion, vol.38, no.2, p.207, 1998.

[6] K. Tobita and the JT-60 Team, "Latest plasma performance and experiments on JT-60U", Plasma Phys. Controlled Fusion, vol.41, no.3A, p.A333, Jan. 1999.

[7] Zhe Gao, *Matter and Radiation at Extremes*, **1** 153-162 (2016).

[8] Y. R. Lin-Liu and R. D. Stambaugh, "Optimum equilibria for high performance, steady state tokamaks", Nucl. Fusion, vol.44, no.4, p.548, Mar. 2004.

[9] Y. K. M. Peng and D. J. Strickler, "Features of spherical torus plasmas", Nucl. Fusion, vol.26, p.769, Feb. 1986.

[10] A. Sykes, the START Team, the NBI Team, the MAST Team, and the Theory Team, "The spherical tokamak programme at Culham", Nucl. Fusion, vol.39, p.1271, Mar. 1999.

[11] N. J. Fisch, "Confining a Tokamak Plasma with rf-Driven Currents", Phys. Rev. Lett., vol.41, no.13, pp.873-876, Sep. 1978.

[12] N. J. Fisch, "Theory of current drive in plasmas", Rev. Mod. Phys., vol.59, no.1, pp.175-234, Jan. 1987.

[13] S. Kubo, M. Nakamura, T. Cho, S. Nakao, T. Shimozuma, A. Ando, K. Ogura, T. Maekawa, Y. Terumichi, and S. Tanaka, "Toroidal Plasma Current Startup and Sustainment by rf in the WT-2 Tokamak", Phys. Rev. Lett., vol.50, no.25, pp.1994-1997, Jun. 1983.

[14] A. Ando, K. Ogura, H. Tanaka, M. Iida, S. Ide, M. Nakamura, T. Maekawa, Y. Terumichi, and S. Tanaka, "Enhancement of efficiency for lower hybrid current drive by electron cyclotron heating in the WT-2 tokamak", Nucl. Fusion, vol.26, no.1, p.107, Jan. 2011.

[15] Y. Takase, T. Fukuda, X. Gao, M. Gryaznevich, S. Ide, S. Itoh, Y. Kamada, T. Maekawa, O. Mitarai, Y. Miura, Y. Sakamoto, S. Shiraiwa, T. Suzuki, S. Tanaka, T. Taniguchi, K. Ushigusa, and J.-60 Team, "Plasma Current Start-up, Ramp-up, and Achievement of Advanced Tokamak Plasmas without the

Use of Ohmic Heating Solenoid in JT-60U", Journal of Plasma and Fusion Research, vol.78, no.8, pp.719-721, 2002.

[16] S. Shiraiwa, S. Ide, S. Itoh, O. Mitarai, O. Naito, T. Ozeki, Y. Sakamoto, T. Suzuki, Y. Takase, S. Tanaka, T. Taniguchi, M. Aramasu, T. Fujita, T. Fukuda, X. Gao, M. Gryaznevich, K. Hanada, E. Jotaki, Y. Kamada, T. Maekawa, Y. Miura, K. Nakamura, T. Nishi, H. Tanaka, K. Ushigusa, and JT-60 Team, "Formation of advanced tokamak plasmas without the use of an ohmic-heating solenoid", Phys. Rev. Lett., vol.92, no.3, p.035001, Jan. 2004.

[17] M. Ushigome, S. Ide, S. Itoh, E. Jotaki, O. Mitarai, S. Shiraiwa, T. Suzuki, Y. Takase, S. Tanaka, T. Fujita, P. Gohil, Y. Kamada, L. Lao, T. Luce, Y. Miura, O. Naito, T. Ozeki, P. Politzer, Y. Sakamoto, and the JT-60 Team, "Development of completely solenoidless tokamak operation in JT-60U", Nucl. Fusion, vol.46, no.2, p.207, Jan. 2006.

[18] C. B. Forest, Y. S. Hwang, M. Ono, and D. S. Darrow, "Internally generated currents in a small-aspect-ratio tokamak geometry", Phys. Rev. Lett., vol.68, no.24, pp.3559-3562, Jun. 1992.

[19] C. B. Forest, Y. S. Hwang, M. Ono, G. Greene, T. Jones, W. Choe, M. Schaffer, A. Hyatt, T. Osborne, R. I. Pinsker, C. C. Petty, J. Lohr, and S. Lippmann, "Investigation of the formation of a fully pressure - driven tokamak", Phys. Plasmas, vol.1, no.5, pp.1568-1575, May 1994.

[20] A. Ejiri, Y. Takase, H. Kasahara, T. Yamada, K. Hanada, K. N. Sato, H. Zushi, K. Nakamura, M. Sakamoto, H. Idei, M. Hasegawa, A. Iyomasa, N. Imamura, K. Esaki, M. Kitaguchi, K. Sasaki, H. Hoshika, O. Mitarai, and N. Nishino, "RF start-up and sustainment experiments on the TST-2@K spherical tokamak", Nucl. Fusion, vol.46, no.7, p.709, May 2006.

[21] M. Uchida, T. Yoshinaga, K. Katsuura, M. Konno, H. Igami, H. Tanaka, and T. Maekawa, "Start-Up of Spherical Torus by ECH without Central Solenoid in the LATE Device", Plasma Fusion Res., vol.80, no.2, pp.83-84, 2004.

[22] T. Maekawa, Y. Terumichi, H. Tanaka, M. Uchida, T. Yoshinaga, S. Yamaguchi, H. Igami, M. Konno, K. Katsuura, K. Hayashi, Y. Abe, J. Yamada, S. Maebara, and T. Imai, "Formation of spherical tokamak equilibria by ECH in the LATE device", Nucl. Fusion, vol.45, no.11, p.1439, Oct. 2005.

[23] K. Hanada, K. Sato, H. Zushi, K. Nakamura, M. Sakamoto, H. Idei, M. Hasegawa, Y. Takase, O. Mitarai, T. Maekawa, Y. Kishimoto, M. Ishiguro, T. Yoshinaga, H. Igami, N. Nishino, H. Honma, S. Kawasaki, H. Nakashima, A. Higashijima, Y. Higashizono, A. Ando, N. Asakura, A. Ejiri, Y. Hirooka, A. Ishida, A. Komori, M. Matsukawa, O. Motojima, Y. Ogawa, N. Ohno, Y. Ono, M. Peng, S. Sudo, H. Yamada, N. Yoshida, and Z. Yoshida, "Steady-State Operation Scenario and the First Experimental Result on QUEST", Plasma and Fusion Research, vol.5, p.S1007, 2010.

[24] H. Idei, O. Watanabe, H. Zushi, K. Hanada, T. Onchi, K. Nakamura, A. Fujisawa, Y. Nagashima, M. Hasegawa, K. Matsuoka, and Others, "Fully non-inductive current drive experiments using 28 GHz and 8.2 GHz electron cyclotron waves in QUEST", National Inst. for Fusion Science, 2014.

[25] M. Ono, S. M. Kaye, Y.-K. M. Peng, G. Barnes, W. Blanchard, M. D. Carter, J. Chrzanowski, L. Dudek, R. Ewig, D. Gates, R. E. Hatcher, T. Jarboe, S. C. Jardin, D. Johnson, R. Kaita, M. Kalish, C. E. Kessel, H. W. Kugel, R. Maingi, R. Majeski, J. Manickam, B. McCormack, J. Menard, D. Mueller, B. A. Nelson, B. E. Nelson, C. Neumeyer, G. Oliaro, F. Paoletti, R. Parsells, E. Perry, N. Pomphrey, S. Ramakrishnan, R. Raman, G. Rewoldt, J. Robinson, A. L. Roquemore, P. Ryan, S. Sabbagh, D. Swain, E. J. Synakowski, M. Viola, M. Williams, J. R. Wilson, and NSTX Team, "Exploration of spherical torus physics in the NSTX device", Nucl. Fusion, vol.40, no.3Y, p.557, 2000.

[26] V. F. Shevchenko, M. R. O ' Brien, D. Taylor, A. N. Saveliev, and MAST team, "Electron Bernstein wave assisted plasma current start-up in MAST", Nucl. Fusion, vol.50, no.2, p.022004, Jan. 2010.

[27] V. F. Shevchenko, Y. F. Baranov, T. Bigelow, J. B. Caughman, S. Diem, C. Dukes, P. Finburg, J. Hawes, C. Gurl, J. Griffiths, J. Mailloux, M. Peng, A. N. Saveliev, Y. Takase, H. Tanaka, and G. Taylor, "Long Pulse EBW Start-up Experiments in MAST", EPJ Web of Conferences, vol.87, p.02007, 2015.

[28] A. Ejiri, Y. Takase, T. Oosako, T. Yamaguchi, Y. Adachi, O. Watanabe, Y. Nagashima, B. I. An, H. Kobayashi, H. Kurashina, H. Hayashi, H. Matsuzawa, K. Yamada, H. Tojo, T. Masuda, M. Sasaki, R. Kumazawa, H. Kasahara, and F. Shimpo, "Non-inductive plasma current start-up by EC and RF power in the TST-2 spherical tokamak", Nucl. Fusion, vol.49, no.6, p.065010, May 2009.

[29] T. Shinya, Y. Takase, T. Wakatsuki, A. Ejiri, H. Furui, J. Hiratsuka, K. Imamura, T. Inada, H. Kakuda, H. Kasahara, R. Kumazawa, C. Moeller, T. Mutoh, Y. Nagashima, K. Nakamura, A. Nakanishi, T. Oosako, K. Saito, T. Seki, M. Sonehara, H. Togashi, S. Tsuda, N. Tsujii, and T. Yamaguchi, "Non-inductive plasma start-up experiments on the TST-2 spherical tokamak using waves in the lower-hybrid frequency range", Nucl. Fusion, vol.55, no.7, p.073003, Jun. 2015.

[30] T. Yamamoto, T. Imai, M. Shimada, N. Suzuki, M. Maeno, S. Konoshima, T. Fujii, K. Uehara, T. Nagashima, A. Funahashi, and N. Fujisawa, "Experimental Observation of the rf-Driven Current by the Lower-Hybrid Wave in a Tokamak", Phys. Rev. Lett., vol.45, no.9, pp.716-719, Sep. 1980.

[31] T. Maekawa, T. Saito, M. Nakamura, T. Cho, S. Kubo, T. Shimozuma, Y. Terumichi, Y. Yamada, and S. Tanaka, "Lower hybrid wave driven current and associated instabilities in the WT-2 tokamak", Phys. Lett. A, vol.85, no.6, pp.339-341, Oct. 1981.

[32] M. Nakamura, T. Cho, S. Kubo, T. Shimozuma, H. Kawai, K. Yamazaki, T. Maekawa, Y. Terumichi, Y. Hamada, and S. Tanaka, "Toroidal Plasma Current Sustainment by Lower Hybrid Waves in the WT-2 Tokamak", Phys. Rev. Lett., vol.47, no.26, pp.1902-1906, Dec. 1981.

[33] S. C. Luckhardt, M. Porkolab, S. F. Knowlton, K.-I. Chen, A. S. Fisher, F. S. McDermott, and M. Mayberry, "Generation of rf-Driven Currents by Lower-Hybrid-Wave Injection in the Versator II Tokamak", Phys. Rev. Lett., vol.48, no.3, pp.152-155, Jan. 1982.

[34] F. Jobes, J. Stevens, R. Bell, S. Bernabei, A. Cavallo, T. K. Chu, S. Cohen, B. Denne, P. Efthimion, E. Hinnov, W. Hooke, J. Hosea, E. Mazzucato, R. McWilliams, R. Motley, S. Suckewer, G. Taylor, J. Timberlake, S. von Goeler, and R. Wilson, "Formation of a 100-kA Tokamak Discharge in the Princeton Large Torus by Lower Hybrid Waves", Phys. Rev. Lett., vol.52, no.12, pp.1005-1008, Mar. 1984.

[35] M. Porkolab, "Survey of Lower Hybrid Experiments", IEEE Trans. Plasma Sci. IEEE Nucl. Plasma Sci. Soc., vol.12, no.2, pp.107-117, Jun. 1984.

[36] S. Texter, S. Knowlton, M. Porkolab, and Y. Takase, "High energy X-ray measurements during lower hybrid current drive on the Alcator C tokamak", Nucl. Fusion, vol.26, no.10, p.1279, 1986.

[37] T. H. Stix. "Waves in Plasma", Americal Institute of Physics, New York, 1992.

[38] W. Hooke, "Review of experiments on current drive in Tokamaks by means of RF waves", Plasma Phys. Controlled Fusion, vol.26, no.1A, p.133, 1984.

[39] Y. Takase, M. Porkolab, J. J. Schuss, R. L. Watterson, C. L. Fiore, R. E. Slusher, and C. M. Surko, "Observation of parametric instabilities in the lower- hybrid range of frequencies in the high- density tokamak", The Physics of Fluids, vol.28, no.3, pp.983-994, Mar. 1985.

[40] G. M. Wallace, R. R. Parker, P. T. Bonoli, A. E. Hubbard, J. W. Hughes, B. L. LaBombard, O. Meneghini, A. E. Schmidt, S. Shiraiwa, D. G. Whyte, J. C. Wright, S. J. Wukitch, R. W. Harvey, A. P. Smirnov, and J. R. Wilson, "Absorption of lower hybrid waves in the scrape off layer of a diverted tokamak", Phys. Plasmas, vol.17, no.8, p.082508, Aug. 2010.

[41] G. M. Wallace, A. E. Hubbard, P. T. Bonoli, I. C. Faust, R. W. Harvey, J. W. Hughes, B. L. LaBombard, O. Meneghini, R. R. Parker, A. E. Schmidt, S. Shiraiwa, A. P. Smirnov, D. G. Whyte, J. R. Wilson, J. C. Wright, S. J. Wukitch, and the Alcator C-Mod Team, "Lower hybrid current drive at high density in Alcator C-Mod", Nucl. Fusion, vol.51, no.8, p.083032, Jul. 2011.

[42] G. M. Wallace, A. E. Hubbard, P. T. Bonoli, I. C. Faust, R. W. Harvey, J. W. Hughes, B. L. LaBombard, O. Meneghini, R. R. Parker, A. E. Schmidt, S. Shiraiwa, A. P. Smirnov, D. G. Whyte, J. R. Wilson, J. C. Wright, S. J. Wukitch, and the Alcator C-Mod Team, "Lower hybrid current drive at high density in Alcator C-Mod", Nucl. Fusion, vol.51, no.8, p.083032, Jul. 2011.

[43] V. V. D'yachenko, V. K. Gusev, M. M. Larionov, A. D. Mel'nik, A. N. Novokhatskii, Y. V. Petrov, V. V. Rozhdestvenskii, N. V. Sakharov, A. Y. Stepanov, S. A. Khitrov, N. A. Khromov, F. V. Chernyshev, A. E. Shevelev, O. N. Shcherbinin, S. E. Bender, A. A. Kavin, and K. M. Lobanov, "Noninductive plasma generation and current drive in the Globus-M spherical tokamak", Plasma Phys. Rep., vol.39, no.3, pp.189-198, Mar. 2013.

[44] N. N. Bakharev, G. I. Abdullina, V. I. Afanasyev, A. B. Altukhov, L. G. Askinazi, N. A. Babinov, A. N. Bazhenov, A. A. Belokurov, M. D. Blekhshtein, E. N. Bondarchuk, I. M. Bukreev, V. V. Bulanin, A. P. Chernakov, F. V. Chernyshev, I. N. Chugunov, A. M. Dmitriev, D. N. Doinikov, V. V. Dyachenko, L. A. Esipov, D. B. Gin, A. V. Gorbunov, A. D. Gurchenko, E. Z. Gusakov, V. K. Gusev, S. Heuraux, M. V. Iliasova, M. A. Irzak, S. N. Kamenshikov, A. A. Kavin, E. M. Khilkevitch, N. A. Khromov, E. O. Kiselev, T. P. Kiviniemi, A. A. Kobelev, V. A. Kornev, A. N. Koval, D. V. Kouprienko, S. V. Krikunov, O. L. Krutkin, G. S. Kurskiev, S. I. Lashkul, S. V. Lebedev, C. Lechte, S. Leerink, A. E. Litvinov, K. M. Lobanov, S. V. Masyukevich, A. A. Martynov, S. Yu. Medvedev, A. D. Melnik, V. B. Minaev, A. B. Mineev, M. I. Mironov, I. V. Miroshnikov, E. E. Mukhin, V. O. Naidenov, A. S. Navolotsky, V. G. Nesenevich, P. Niskala, A. N. Novokhatskii, K. Yu. Oshuev, M. I. Patrov, A. V. Petrov, M. P. Petrov, S. Ya. Petrov, Y. V. Petrov, I. A. Polunovsky, A. Yu. Popov, A. G. Razdobarin, D. V. Razumenko, V. V. Rozhdestvensky, N. V. Sakharov, D. S. Samsonov, A. N. Saveliev, V. A. Senichenkov, P. B. Shchegolev, A. E. Shevelev, A. D. Sladkomedova, A. I. Smirnov, A. S. Smirnov, V. V. Solokha, V. A. Solovei, A. Yu. Stepanov, A. Yu. Telnova, V. A. Tokarev, S. Yu. Tolstyakov, P. V. Tretinnikov, I. B. Tereschenko, A. S. Tukachinsky, E. A. Tukhmeneva, V. I. Varfolomeev, L. A. Varshavchick, A. Yu. Yashin, E. G. Zhilin, and N. A. Zhubr, "Tokamak research at the Ioffe Institute", Nucl. Fusion, vol.59, no.11, p.112022, Aug. 2019.

[45] Y. Takase, A. Ejiri, N. Kasuya, T. Mashiko, S. Shiraiwa, L. M. Tozawa, T. Akiduki, H. Kasahara, Y. Nagashima, H. Nozato, H. Wada, H. Yamada, T. Yamada, and K. Yamagishi, "Initial results from the TST-2 spherical tokamak", Nucl. Fusion, vol.41, no.11, p.1543, May 2002.

[46] H. Toyama, K. Hanada, and H. Totsuka, "Comparative studies of a spherical tokamak and a conventional tokamak: Magnetic turbulence-induced transport", IAEA-CN-69/EXP2/15, paper presented at 17th IAEA Conf. on Fusion Energy, Yokohama, 1998.

[47] T. Shinya, Y. Takase, S. Yajima, C. Moeller, H. Yamazaki, N. Tsujii, Y. Yoshida, A. Ejiri, H. Togashi, K. Toida, H. Furui, H. Homma, K. Nakamura, B. Roidl, M. Sonehara, W. Takahashi, and T. Takeuchi, "Plasma current start-up experiments using outboard- and top-launch lower hybrid wave on the TST-2 spherical tokamak", Nucl. Fusion, vol.57, no.3, p.036006, Mar. 2017.

[48] S. Yajima, Y. Takase, A. Ejiri, N. Tsujii, H. Yamazaki, C. P. Moeller, T. Shinya, Y. Takei, Y. Tajiri, Y. Yoshida, A. Sato, A. Kitayama, and N. Matsumoto, "Current Drive Experiment Using Top/Outboard Side Lower Hybrid Wave Injection on TST-2 Spherical Tokamak", Plasma and Fusion Research, vol.13, p.3402114, 2018.

[49] S. Yajima, Y. Takase, Y. Tajiri, Y. Takei, N. Tsujii, H. Yamazaki, C. P. Moeller, and T. Shinya, "Development of capacitively-coupled combline antennas for current drive in tokamaks", Nucl. Fusion, vol.59, no.6, p.066004, Apr. 2019.

[50] K. Ogura, T. Cho, A. Ando, H. Tanaka, M. Iida, S. Ide, M. Nakamura, T. Maekawa, Y. Terumichi, and S. Tanaka, "Formation of High Energy Electron Tail during rf Plasma Current Start-Up in the WT-2 Tokamak", J. Phys. Soc. Jpn., vol.55, no.1, pp.13-16, Jan. 1986.

[51] E. H. Silver, M. Bitter, K. Brau, D. Eames, A. Greenberger, K. W. Hill, D. M. Meade, W. Roney, N. R. Sauthoff, and S. Von Goeler, "Soft x- ray measurements from the PDX tokamak", Rev. Sci. Instrum., vol.53, no.8, pp.1198-1213, Aug. 1982.

[52] Thomas J. Dolan Editor, *Magnetic Fusion Technology*, Springer, London, pp.560-561, 2013.

[53] L. C. Ingesson, B. Alper, B. J. Peterson, and J.-C. Vallet, "Chapter 7: Tomography Diagnostics: Bolometry and Soft-X-Ray Detection", Fusion Sci. Technol., vol.53, no.2, pp.528-576, Feb. 2008.

[54] R. S. Granetz and P. Smeulders, "X-ray tomography on JET", Nucl. Fusion, vol.28, no.3, pp.457-476, 1988.

[55] K. Ertl, W. von der Linden, V. Dose, and A. Weller, "Maximum entropy based reconstruction of soft X-ray emissivity profiles in W7-AS", Nucl. Fusion, vol.36, no.11, p.1477, Oct. 2002.

[56] M. Anton, H. Weisen, M. J. Dutch, W. von der Linden, F. Buhlmann, R. Chavan, B. Marletaz, P. Marmillod, and P. Paris, "X-ray tomography on the TCV tokamak", Plasma Phys. Controlled Fusion, vol.38, no.11, p.1849, Jan. 1999.

[57] J. Liptac, R. Parker, V. Tang, Y. Peysson, and J. Decker, "Hard x-ray diagnostic for lower hybrid experiments on Alcator C-Mod", Rev. Sci. Instrum., vol.77, no.10, p.103504, Oct. 2006.

[58] L. C. Ingesson, B. Alper, H. Chen, A. W. Edwards, G. C. Fehmers, J. C. Fuchs, R. Giannella, R. D. Gill, L. Lauro-Taroni, and M. Romanelli, "Soft X ray tomography during ELMs and impurity injection in JET", Nucl. Fusion, vol.38, no.11, p.1675, May 2002.

[59] Y. Peysson and F. Imbeaux, "Tomography of the fast electron bremsstrahlung emission during lower hybrid current drive on TORE SUPRA", Rev. Sci. Instrum., vol.70, no.10, pp.3987-4007, Oct. 1999.

[60] A. Ince-Cushman, J. E. Rice, M. Bitter, M. L. Reinke, K. W. Hill, M. F. Gu, E. Eikenberry, C. Broennimann, S. Scott, Y. Podpaly, S. G. Lee, and E. S. Marmar, "Spatially resolved high resolution x-ray spectroscopy for magnetically confined fusion plasmas (invited)", Rev. Sci. Instrum., vol.79, no.10, p.10E302, Oct. 2008.

[61] K. W. Hill, M. L. Bitter, S. D. Scott, A. Ince-Cushman, M. Reinke, J. E. Rice, P. Beiersdorfer, M.-F. Gu, S. G. Lee, C. Broennimann, and E. F. Eikenberry, "A spatially resolving x-ray crystal spectrometer for measurement of ion-temperature and rotation-velocity profiles on the Alcator C-Mod tokamak", Rev. Sci. Instrum., vol.79, no.10, p.10E320, Oct. 2008.

[62] M. L. Reinke, Y. A. Podpaly, M. Bitter, I. H. Hutchinson, J. E. Rice, L. Delgado-Aparicio, C. Gao, M. Greenwald, K. Hill, N. T. Howard, A. Hubbard, J. W. Hughes, N. Pablant, A. E. White, and S. M. Wolfe, "X-ray imaging crystal spectroscopy for use in plasma transport research", Rev. Sci. Instrum., vol.83, no.11, p.113504, Nov. 2012.

[63] L. Delgado-Aparicio, M. Bitter, Y. Podpaly, J. Rice, W. Burke, M. S. del Rio, P. Beiersdorfer, R. Bell, R. Feder, C. Gao, K. Hill, D. Johnson, S. G. Lee, E. Marmar, N. Pablant, M. L. Reinke, S. Scott, and R. Wilson, "Effects of thermal expansion of the crystal lattice on x-ray crystal spectrometers used for fusion research", Plasma Phys. Controlled Fusion, vol.55, no.12, p.125011, Nov. 2013.

[64] N. A. Pablant, R. E. Bell, M. Bitter, L. Delgado-Aparicio, K. W. Hill, S. Lazerson, and S. Morita, "Tomographic inversion techniques incorporating physical constraints for line integrated spectroscopy in stellarators and tokamaks", Rev. Sci. Instrum., vol.85, no.11, p.11E424, Nov. 2014.

[65] N. A. Pablant, S. Satake, M. Yokoyama, D. A. Gates, M. Bitter, N. Bertelli, L. Delgado-Aparicio, A. Dinklage, M. Goto, K. W. Hill, and Others, "Investigation of ion and electron heat transport of high-T e ECH heated discharges in the large helical device", Plasma Phys. Controlled Fusion, vol.58, no.4, p.045004, 2016.

[66] S. G. Lee, J. G. Bak, M. Bitter, M. K. Moon, U. W. Nam, K. C. Jin, K. N. Kong, and K. I. Seon, "Imaging x-ray crystal spectrometers for KSTAR", Rev. Sci. Instrum., vol.74, no.3, pp.1997-2000, Mar. 2003.

[67] B. Lyu, F. D. Wang, X. Y. Pan, J. Chen, J. Fu, Y. Y. Li, M. Bitter, K. W. Hill, L. F. Delgado-Aparicio, N. Pablant, S. G. Lee, Y. J. Shi, M. Y. Ye, and B. N. Wan, "Upgrades of imaging x-ray crystal spectrometers for high-resolution and high-temperature plasma diagnostics on EAST", Rev. Sci. Instrum., vol.85, no.11, p.11E406, Nov. 2014.

[68] A. Ejiri, T. Yamaguchi, J. Hiratsuka, Y. Takase, M. Hasegawa, and K. Narihara, "Development of a Bright Polychromator for Thomson Scattering Measurements", Plasma and Fusion Research, vol.5, p.S2082, 2010.

[69] T. Sato, Y. Iwamoto, S. Hashimoto, T. Ogawa, T. Furuta, S.-I. Abe, T. Kai, P.-E. Tsai, N. Matsuda, H. Iwase, N. Shigyo, L. Sihver, and K. Niita, "Features of Particle and Heavy Ion Transport code System (PHITS) version 3.02", J. Nucl. Sci. Technol., vol.55, no.6, pp.684-690, Jun. 2018.

[70] Y. Iwamoto, T. Sato, S. Hashimoto, T. Ogawa, T. Furuta, S.-I. Abe, T. Kai, N. Matsuda, R. Hosoyamada, and K. Niita, "Benchmark study of the recent version of the PHITS code", J. Nucl. Sci. Technol., vol.54, no.5, pp.617-635, May 2017.

[71] L. L. Lao, H. St. John, R. D. Stambaugh, A. G. Kellman, and W. Pfeiffer, "Reconstruction of current profile parameters and plasma shapes in tokamaks", Nucl. Fusion, vol.25, no. 11, p.1611, Jan. 2011.

[72] R. W. Harvey and M. G. McCoy, "The cql3d fokker-planck code", IAEA TCM, Montreal, 1992.

[73] I. H. Hutchinson, "Principles of Plasma Diagnostics", Cambridge University Press, 1987.

[74] H. R. Griem, "Principles of Plasma Spectroscopy", Cambridge University Press, 1997.

[75] S. Von Goeler, W. Stodiek, H. Eubank, H. Fishman, S. Grebenshchikov, and E. Hinnov, "Thermal X-ray spectra and impurities in the ST Tokamak", Nucl. Fusion, vol.15, no.2, p.301, 1975.

[76] R. Hofstadter, "The Detection of Gamma-Rays with Thallium-Activated Sodium Iodide Crystals", Phys. Rev., vol.75, no.5, pp.796-810, Mar. 1949.

[77] D. W. Cooke, K. J. McClellan, B. L. Bennett, J. M. Roper, M. T. Whittaker, R. E. Muenchausen, and R. C. Sze, "Crystal growth and optical characterization of cerium-doped Lu1.8Y0.2SiO5", J. Appl. Phys., vol.88, no.12, pp.7360-7362, Dec. 2000.

[78] T. Kimble, M. Chou, and B. H. T. Chai, "Scintillation properties of LYSO crystals", 2002 IEEE Nuclear Science Symposium Conference Record, vol.3, pp.1434-1437 vol.3, Nov. 2002.

[79] J. Chen, R. Mao, L. Zhang, and R. Zhu, "Large Size LSO and LYSO Crystals for Future High Energy Physics Experiments", IEEE Trans. Nucl. Sci., vol.54, no.3, pp.718-724, Jun. 2007.

[80] E. V. D. van Loef, P. Dorenbos, C. W. E. van Eijk, K. Krämer, and H. U. Güdel, "High-energy-resolution scintillator: Ce3+ activated LaBr3", Appl. Phys. Lett., vol.79, no.10, pp.1573-1575, Sep. 2001.

[81] Tokushi Shibata, *Introduction to Radiation Basics*, tsuusyousangyou–kenkyuusya, Tokyo, 2011. [in Japanese]

[82] Hamamatsu Photonics K.K, *"PHOTOMULTIPLIER TUBES - Basics and Applications -"*, Third Edition, p.27, 2007.

[83] Hamamatsu Photonics K.K, *"Datasheet of H10426"*, Available at `https://www.hamamatsu.com/eu/en/product/type/H10426/index.html`, accessed Oct. 20. 2019.

[84] The Japan Radioisotope Association, "Radioisotope Pocket Data Book 11th Edition", pp.110-111, Maruzen, Tokyo, 2012. [in Japanese]

[85] H. Yamazaki, "Master Thesis: A Study of Start-Up Process of Spherical Tokamak Configurations Using Lower Hybrid Wave Current Drive and Plasma Merging", The University of Tokyo, 2017.

[86] H. Togashi, H. Yamazaki, A. Ejiri, Y. Takase, N. Tsujii, S. Yajima, Y. Yoshida, and TST-2 Team, "Development of a Hard X-Ray Profile Measurement System in the TST-2 Spherical Tokamak", Plasma and Fusion Research, vol.12, pp.1402030-1402030, 2017.

[87] H. Togashi, "Doctoral Thesis: Electron temperature and density profile measurement in spherical tokamaks started-up by radio frequency waves", The University of Tokyo, 2017.

[88] Walt Jung, "Op Amp Applications Handbook", Newnes Elsevier, sec.1-4 and sec.4-4, pp.51-88, 257-284, 2005, UK.

[89] L. Smith, D. H. Sheingold, "Noise and operational amplifier circuits" in Analogue Dialogue, Analogue Devices, Inc., vol.3, Mar 1969.

[90] "Datasheet: OPA627 and OPA637 Precision High-Speed Difet Operational Amplifiers", Texas Instruments, 2015. Available at `http://www.ti.com/jp/lit/ds/symlink/opa627.pdf`, accessed Sep. 22. 2019.

[91] J. H. Hubbell and S. M. Seltzer, "X-Ray Mass Attenuation Coefficients", Available at `https://www.nist.gov/pml/x-ray-mass-attenuation-coefficients`, last accessed Sep. 22. 2019.

[92] H. Goldstein, J. E. Wilkins Jr., "Calculations of the penetration of gamma rays", NYO-3075, 1954.

[93] American National Standard, "Gamma-Ray Attenuation Coefficients and Buildup Factors for Engineering Materials", ANSI/ANS-6.4.3, 1991.

[94] J. A. Bearden and A. F. Burr, "Reevaluation of X-Ray Atomic Energy Levels", Rev. Mod. Phys., vol.39, no.1, pp.125-142, Jan. 1967.

[95] H. K. Tseng, R. H. Pratt, and C. M. Lee, "Electron bremsstrahlung angular distributions in the 1-500 keV energy range", Phys. Rev. A, vol.19, no.1, pp.187-195, Jan. 1979.

[96] A. Murari, C. Vinante, and M. Monari, "Comparison of PEEK and VESPEL®SP1 characteristics as vacuum seals for fusion applications", Vacuum, vol.65, no.2, pp.137-145, Apr. 2002.

[97] "Product information for PEEK", Available at `https://www.toplaseiko.com/en/product/tps_peek.html`, last accessed Oct. 20. 2019.

[98] Y. Sato, S. Takeda, T. Omori, N. Kimura, T. Suzuki, Y. Saito, "Outgassing Rate Measurement of the Plastics", Journal of the Vacuum Society of Japan, vol.56, no.10, pp.422-424, 2013. [in Japanese]

[99] European Space Research and Technology Centre, "Outgassing database", Available at `http://esmat.esa.int/services/outgassing_data/outgassing_data.html`, last accessed Oct. 20. 2019.

[100] HEISHIN Ltd., "The engineer's book vol.19, p.96", Available at `http://ebw.eng-book.com/heishin/vfs/calculation/DiskMaximumStressAndDeflection/`, last accessed Oct. 20. 2019. [in Japanese]

[101] C. Brönnimann, R. Baur, E. F. Eikenberry, S. Kohout, M. Lindner, B. Schmitt, and R. Horisberger, "A pixel read-out chip for the PILATUS project", Nuclear Instruments and Methods in Physics Research Section A: Accelerators, Spectrometers, Detectors and Associated Equipment, vol.465, no.1, pp.235-239, 2001.

[102] P. Kraft, A. Bergamaschi, C. Broennimann, R. Dinapoli, E. F. Eikenberry, B. Henrich, I. Johnson, A. Mozzanica, C. M. Schlepütz, P. R. Willmott, and B. Schmitt, "Performance of single-photon-counting PILATUS detector modules", J. Synchrotron Radiat., vol.16, no.3, pp.368-375, May 2009.

[103] P. Kraft, A. Bergamaschi, C. Bronnimann, R. Dinapoli, E. F. Eikenberry, H. Graafsma, B. Henrich, I. Johnson, M. Kobas, A. Mozzanica, C. M. Schleputz, and B. Schmitt, "Characterization and Calibration of PILATUS Detectors", IEEE Trans. Nucl. Sci., vol.56, no.3, pp.758-764, Jun. 2009.

[104] See `https://www.dectris.com`

[105] L. F. Delgado-Aparicio, J. Maddox, N. Pablant, K. Hill, M. Bitter, J. E. Rice, R. Granetz, A. Hubbard, J. Irby, M. Greenwald, E. Marmar, K. Tritz, D. Stutman, B. Stratton, and P. Efthimion, "Multi-energy SXR cameras for magnetically confined fusion plasmas (invited)", Rev. Sci. Instrum., vol.87, no.11, p.11E204, Nov. 2016.

[106] N. A. Pablant, L. Delgado-Aparicio, M. Bitter, S. Brandstetter, E. Eikenberry, R. Ellis, K. W. Hill, P. Hofer, and M. Schneebeli, "Novel energy resolving x-ray pinhole camera on Alcator C-Mod", Rev. Sci. Instrum., vol.83, no.10, p.10E526, Oct. 2012.

[107] L. F. Delgado-Aparicio, J. Wallace, H. Yamazaki, P. VanMeter, L. Reusch, M. Nornberg, A. Almagari, J. Maddox, B. Luethi, M. Rissi, T. Donath, D. Den Hartog, J. Sarff, P. Weix, J. Goetz, N. Pablant, K. Hill, B. Stratton, P. Efthimion, Y. Takase, A. Ejiri, and M. Ono, "Simulation, design, and first test of a multi-energy soft x-ray (SXR) pinhole camera in the Madison Symmetric Torus (MST)", Rev. Sci. Instrum., vol.89, no.10, p.10G116, Oct. 2018.

[108] P. VanMeter, L. F. Delgado-Aparicio, L. Reusch, N. Pablant, J. Maddox, M. Rissi, B. Luethi, T. Donath, C. Schulze-Briese, K. Hill, and D. Den Hartog, "Pixel-to-pixel variation on a calibrated PILATUS3-based multi-energy soft x-ray detector", Rev. Sci. Instrum., vol.89, no.10, p.10G119, Oct. 2018.

[109] P. D. VanMeter, L. F. Delgado-Aparicio, L. M. Reusch, and D. J. Den Hartog, "A versatile multi-energy soft x-ray diagnostic for Te measurements in the Madison Symmetric Torus", J. Instrum., vol.14, no.09, p.C09009, Sep. 2019.

[110] P. D. VanMeter, Private communication, Jun 2019.

[111] H. Yamazaki, L. F. Delgado-Aparicio, R. Groebner, B. Grierson, K. Hill, N. Pablant, B. Stratton, P. Efthimion, A. Ejiri, Y. Takase, and M. Ono, "A computational tool for simulation and design of tangential multi-energy soft x-ray pin-hole cameras for tokamak plasmas", Rev. Sci. Instrum., vol.89, no.10, p.10G120, Oct. 2018.

[112] H.-K. Chung, W. L. Morgan, and R. W. Lee, "FLYCHK: an extension to the K-shell spectroscopy kinetics model FLY", J. Quant. Spectrosc. Radiat. Transf., vol.81, no.1, pp.107-115, Sep. 2003.

[113] H.-K. Chung, M. H. Chen, W. L. Morgan, Y. Ralchenko, and R. W. Lee, "FLYCHK: Generalized population kinetics and spectral model for rapid spectroscopic analysis for all elements", High Energy Density Phys., vol.1, no.1, pp.3-12, Dec. 2005.

[114] R. W. Lee and J. T. Larsen, "A time-dependent model for plasma spectroscopy of K-shell emitters", J. Quant. Spectrosc. Radiat. Transf., vol.56, no.4, pp.535-556, Oct. 1996.

[115] H. K. Chung, Private communication, Jun 2019.

[116] J. Maddox, N. Pablant, P. Efthimion, L. Delgado-Aparicio, K. W. Hill, M. Bitter, M. L. Reinke, M. Rissi, T. Donath, B. Luethi, and B. Stratton, "Multi-energy x-ray detector calibration for T and impurity density (n) measurements of MCF plasmas", Rev. Sci. Instrum., vol.87, no.11, p.11E320, Nov. 2016.

[117] Manuel Sánchez del Río, Roger J. Dejus, "XOP v2.4: recent developments of the x-ray optics software toolkit", Proc. SPIE, vol.8141, Advances in Computational Methods for X-Ray Optics II, p.814115, 2011.

[118] See `http://www.esrf.eu/Instrumentation/software/data-analysis/xop2.4`

[119] L. F. Delgado-Aparicio, Private communication, Jul 2017.

[120] R. E. Bell, "Inversion technique to obtain an emissivity profile from tangential line-integrated hard x-ray measurements", Rev. Sci. Instrum., vol.66, no.1, pp.558-560, Jan. 1995.

[121] R. N. Dexter, D. W. Kerst, T. W. Lovell, S. C. Prager, and J. C. Sprott, "The Madison Symmetric Torus", Fusion Technol., vol.19, no.1, pp.131-139, Jan. 1991.

[122] J. S. Sarff, S. A. Hokin, H. Ji, S. C. Prager, and C. R. Sovinec, "Fluctuation and transport reduction in a reversed field pinch by inductive poloidal current drive", Phys. Rev. Lett., vol.72, no.23, pp.3670-3673, Jun. 1994.

[123] B. E. Chapman, A. F. Almagri, J. K. Anderson, T. M. Biewer, P. K. Chattopadhyay, C.-S. Chiang, D. Craig, D. J. Den Hartog, G. Fiksel, C. B. Forest, A. K. Hansen, D. Holly, N. E. Lanier, R. O ' Connell, S. C. Prager, J. C. Reardon, J. S. Sarff, M. D. Wyman, D. L. Brower, W. X. Ding, Y. Jiang, S. D. Terry, P. Franz, L. Marrelli, and P. Martin, "High confinement plasmas in the Madison Symmetric Torus reversed-field pinch", Phys. Plasmas, vol.9, no.5, pp.2061-2068, May 2002.

[124] M. E. Puiatti, S. Cappello, R. Lorenzini, S. Martini, S. Ortolani, R. Paccagnella, F. Sattin, D. Terranova, T. Bolzonella, A. Buffa, A. Canton, L. Carraro, D. F. Escande, L. Garzotti, P. Innocente, L. Marrelli, E. Martines, P. Scarin, G. Spizzo, M. Valisa, P. Zanca, V. Antoni, L. Apolloni, M. Bagatin, W. Baker, O. Barana, D. Bettella, P. Bettini, R. Cavazzana, M. Cavinato, G. Chitarin, A. Cravotta, F. D ' Angelo, S. Dal Bello, A. De Lorenzi, D. Desideri, P. Fiorentin, P. Franz, L. Frassinetti, E. Gaio, L. Giudicotti, F. Gnesotto, L. Grando, S. C. Guo, A. Luchetta, G. Malesani, G. Manduchi, G. Marchiori, D. Marcuzzi, P. Martin, A. Masiello, F. Milani, M. Moresco, A. Murari, P. Nielsen, R. Pasqualotto, B. Pégourie, S. Peruzzo, R. Piovan, P. Piovesan, N. Pomaro, G. Preti, G. Regnoli, G. Rostagni, G. Serianni, P. Sonato, E. Spada, M. Spolaore, C. Taliercio, G. Telesca, V. Toigo, N. Vianello, P. Zaccaria, B. Zaniol, L. Zanotto, E. Zilli, G. Zollino, and M. Zuin, "Analysis and modelling of the magnetic and plasma profiles during PPCD experiments in RFX", Nucl. Fusion, vol.43, no.10, p.1057, Sep. 2003.

[125] P. Franz, M. Gobbin, L. Marrelli, A. Ruzzon, F. Bonomo, A. Fassina, E. Martines, and G. Spizzo, "Experimental investigation of electron temperature dynamics of helical states in the RFX-Mod reversed field pinch", Nucl. Fusion, vol.53, no. 5, p.053011, Apr. 2013.

[126] M. E. Galante, L. M. Reusch, D. J. Den Hartog, P. Franz, J. R. Johnson, M. B. McGarry, M. D. Nornberg, and H. D. Stephens, "Determination of Zeff by integrating measurements from x-ray tomography and charge exchange recombination spectroscopy", Nucl. Fusion, vol.55, no.12, p.123016, Nov. 2015.

[127] J. L. Luxon, "A design retrospective of the DIII-D tokamak", Nucl. Fusion, vol.42, no.5, p.614, May 2002.

[128] C. C. Petty and the DIII-D Team, "DIII-D research towards establishing the scientific basis for future fusion reactors", Nucl. Fusion, vol.59, no.11, p.112002, Jun. 2019.

[129] M. S. Vorenkamp, A. Nagy, A. Bortolon, R. Lunsford, R. Maingi, D. K. Mansfield, and A. L. Roquemore, "Recent Upgrades of the DIII-D Impurity Granule Injector", Fusion Sci. Technol., vol.72, no.3, pp.488-495, Oct. 2017.

[130] R. Groebner, Private communication, Jan. 2018.

[131] R. Guirlet, C. Giroud, T. Parisot, M. E. Puiatti, C. Bourdelle, L. Carraro, N. Dubuit, X. Garbet, and P. R. Thomas, "Parametric dependences of impurity transport in tokamaks", Plasma Physics and Controlled Fusion, vol.48, p.B63, Nov. 2006.

[132] C. Angioni, E. Fable, M. Greenwald, M. Maslov, P. G. A, H. Takenaga, and H. Weisen, "Particle transport in tokamak plasmas, theory and experiment", Plasma Physics and Controlled Fusion, vol.51, no.12, p.124017, Nov. 2009.

[133] B. A. Grierson, K. H. Burrell, R. M. Nazikian, W. M. Solomon, A. M. Garofalo, E. A. Belli, G. M. Staebler, M. E. Fenstermacher, G. R. McKee, T. E. Evans, D. M. Orlov, S. P. Smith, C. Chrobak, and C. Chrystal, "Impurity confinement and transport in high confinement regimes without edge localized modes on DIII-D", Phys. Plasmas, vol.22, no.5, p.055901, May 2015.

[134] L. Delgado-Aparicio, R. E. Bell, I. Faust, K. Tritz, A. Diallo, S. P. Gerhardt, T. A. Kozub, B. P. LeBlanc, and B. C. Stratton, "High-resolution tangential absolute extreme ultraviolet arrays for radiated power density measurements on NSTX-U", Rev. Sci. Instrum., vol.85, no.11, p.11D859, Nov. 2014.

[135] K. Brau, S. von Goeler, M. Bitter, R. D. Cowan, D. Eames, K. Hill, N. Sauthoff, E. Silver, and W. Stodiek, "Observations of giant recombination edges on the Princeton Large Torus tokamak induced by particle transport", Phys. Rev. A, vol.22, no.6, pp.2769-2775, Dec. 1980.

[136] JT-60SA Research Unit, "JT-60SA Research Plan – Research Objectives and Strategy – Version 4.0," p.16, Sep. 2018.

[137] H. Dreicer, "Electron and Ion Runaway in a Fully Ionized Gas. I", Phys. Rev., vol.115, no.2, pp.238-249, Jul. 1959.

[138] R. J. Goldston, P. H. Rutherford, *Introduction to Plasma Physics*, Taylor & Francis, New York, 1995.

[139] S. Yajima, "Comparison of Ip Start-up by Outboard-Launch and Top- Launch LHW on TST-2", Presented in 6th Kyushu Workshop on Solenoid-Free RF-Only ST Plasmas, Kyushu University, Feb. 1-2, 2018.

[140] N. Tsujii, Y. Takase, A. Ejiri, T. Shinya, H. Togashi, S. Yajima, H. Yamazaki, C. P. Moeller, B. Roidl, M. Sonehara, W. Takahashi, K. Toida, and Y. Yoshida, "Numerical modeling of lower hybrid current drive in fully non-inductive plasma start-up experiments on TST-2", Nucl. Fusion, vol.57, no.12, p.126032, Sep. 2017.

[141] N. Tsujii, "Development of a microwave polarimeter for the measurement of the lower-hybrid driven current profile on the TST-2 spherical tokamak", Poster presented in APS-DPP meeting, Nov. 5-9, 2018.

[142] A. Ejiri, "Plasma current start-up by using the lower hybrid wave and its modeling on TST-2", Presentation material for JPS meeting, Jan. 17, 2020.

[143] L. Chen, J. Vaclavik, and G. W. Hammett, "Ion radial transport induced by ICRF waves in tokamaks", Nucl. Fusion, vol.28, no.3, p.389, Mar. 1988.